VORTEX INTERACTION WITH A

LEADING-EDGE OF FINITE THICKNESS*

by

D. Sohn and D. Rockwell
Department of Mechanical Engineering and Mechanics
354 Packard Laboratory #19
Lehigh University
Bethlehem, Pennsylvania 18015

* Final technical report on NASA Grant NAG-1-461
"Free vorticity field-boundary layer conversions:
Effect of boundary configuration and scale",
Langley Research Center (2/33/84 to 4/30/87).

Principal Investigator: Professor Donald Rockwell
Program Monitors: Dr. James Yu
Dr. Paul Pao

TABLE OF CONTENTS

ABSTRACT

Vortex interaction with a thick elliptical leading-edge at zero relative offset produces a pronounced secondary vortex of opposite sense that travels with the same phase speed as the primary vortex along the lower surface of the edge. For the range of parameters examined, this primary-secondary vortex combination, once formed, does not move away from the surface. In contrast to the case of a thin leading-edge, there is no "sweeping" of flow about the tip of the edge during the formation of the secondary vortex.

The edge thickness (scale) relative to the incident vorticity field has a strong effect on the distortion of the incident primary vortex during the impingement process. When the thickness (scale) is sufficiently small, there is a definite "severing" of the incident vortex and the portion of the incident vortex that travels along the upper part of the elliptical surface has a considerably larger phase speed than that along the lower surface; this suggests that the integrated loading along the upper surface is more strongly correlated. When the thickness (scale) becomes too large, then most, if not all, of the incident vortex passes below the leading-edge. The edge thickness (scale), however, does not have any significant effect on the secondary vortex formation process.

On the other hand, the relative transverse offset of the edge with respect to the center of the incident vortex has a significant effect on the secondary vortex formation. At zero offset, the vortex

impinges directly along the centerline of the edge, while positive and negative offsets of the edge produce vortex trajectories below and above the centerline. The secondary vortex is most pronounced for the zero offset case and is less so for the positive offset case; the secondary vortex for this positive offset case breaks apart following its formation. The negative offset case, however, does not produce any secondary vortex on either the upper or lower surfaces of the leading-edge. Due to the large thickness of the edge, the incident vortex passes along either the upper or lower surface of the edge, and no "severing" of the vortex occurs. This physics of the flow is directly reflected in the pressure amplitude and phase measurements. Along the surface where the distorted primary vortex and the secondary vortex (if any) travel, there is a propagating pressure wave. However, on that portion of the surface where there is no primary vortex, there occurs a relatively constant phase, corresponding to no wave-like motion. The wavelength of the propagating wave also changes for the various offset cases; the wavelength of vortex-induced pressure field, corresponding to the negative offset case, is approximately twice that of zero and positive offset cases.

INTRODUCTION

There is a strong need for a deeper understanding of the interaction of unsteady vorticity fields with solid boundaries of various geometries. The interaction process results in structural loading and noise generation in a number of applications: leading-edges of airplane wings, propeller blades, turbine guide vanes, cavities in submarine and ship hulls, bridge decks and turbulence attenuators (Naudascher and Rockwell 1980).

The unsteady vorticity fields are basically inherent to all unstable shear layers. In all shear layer configurations (mixing layer, planar jet, axisymmetric jet and planar wake), the growth of the initially unstable disturbance that leads to eventual formation of a concentration of vorticity, i.e. "vortex", is qualitatively similar. First, immediately downstream of the separation, small vorticity perturbations are rapidly amplified in a "linear" growth region. The wave propagation velocity, rate of amplification, and amplitude of the pressure fluctuation, can be predicted in this region by applying linearized stability theory (Freymuth 1966, Michalke 1965). Of course, this "linear" region of growth is not linear at all but rather shows an exponential growth; if semi-logarithmic coordinates are used, then the disturbance is said to amplify "linearly" in the streamwise direction. Further downstream, when the disturbance amplitude reaches the value of ten percent or so of the free-stream velocity U, it undergoes distortion in the

nonlinear growth region, eventually concentrating into organized vortical-like structures. During this evolution process, the spectral content of the shear layer changes from distributed vorticity of a single predominant frequency to concentrated vorticity having several discrete frequencies and eventually forms multiple concentrations ov vorticity having broader frequency content. Beyond this region, the spectral broadening process eventually leads to fully three-dimensional turbulent flow (Miksad 1972, Sato and Kuriki 1961). Hence there is a wide range of unsteady shear flows with varying coherence, from well-defined single, concentrated vortices to fully turbulent flow. Bushnell (1984) extensively reviews various categories of these flows and discusses their interaction with surfaces having sharp and blunt leading-edges. Booth and Yu (1984) and Rockwell (1983, 1984) also review recent experimental and theoretical simulations of coherent vortex-leading edge interactions.

Various studies have been carried out recently, covering a wide range of interactions of unsteady distributed and concentrated vorticity fields with leading-edges such as: distributed vorticity at a single frequency, concentrated vorticity at a single frequency, concentrated vorticity at multiple frequencies, and concentrated streamwise vorticity.

Distributed vorticity at a single frequency. As mentioned previously, distributed vorticity can be defined as an unsteady shear

flow whose vorticity has not yet agglomerated into a coherent concentration of vorticity. This type of vorticity field provides a simple case for examining the basic features of leading-edge interaction. Kaykayoglu and Rockwell (1985) employed the configuration of a planar jet, oscillating in its sinuous mode, to generate a distributed vorticity field. The oscillating jet, unlike mixing layers and wake regions with ill-defined near fields due to presence of a splitter plate, produces a distributed vorticity field which is in good agreement with linear stability theory. By generating a relatively small amplitude disturbance in a shear layer incident upon the edge, rollup of the incident shear layer into a concentration of vorticity can be avoided. In the flow region near the leading edge, the interaction process between the upstream distributed vorticity field and the solid surface causes rapid amplification and subsequent vortex formation. A semi-infinite length thin leading-edge was used to study the interaction process. Extensive visualization showed details of formation of primary and secondary vortices near the tip of the leading-edge. Even though, as mentioned earlier, incident vortices were not present in the jet shear layer upstream of the edge, transverse oscillation of the jet allowed their rapid formation near and downstream of the tip of the leading edge. The growth of the primary vortex gives rise to an instantaneous adverse pressure gradient near the tip region. The pressure gradient causes flow separation from the surface of the edge and subsequent

formation of the secondary vortex. Using an experimental technique which will be discussed in detail in a subsequent chapter, Kaykayoglu and Rockwell (1985) reconstructed the instantaneous pressure fields along the surface of the edge. This revealed that the pressure took on its maximum negative value, downstream of the tip of the edge at the point of the separation. The pressure field along the surface of the edge showed very small streamwise phase variation near the tip even though the visualization showed that the primary vortex past the edge has a very well-defined phase speed and wavelength. Hence, in the region of greatest flow distortion, the surface pressure field is nonpropagating, in contrast to the propagating wave associated with the primary vortex formation. This negligible streamwise variation of the pressure phase in the tip region thus provides highly correlated pressure fluctuations and large force amplitude. Flow visualization and simultaneous pressure measurement revealed that the onset of flow separation immediately downstream of the tip produced the highest fluctuation amplitude, though the amplitude associated with the primary-secondary vortex pair downstream remained substantial.

Concentrated vorticity at a single frequency. Unlike a planar jet or wake, a mixing-layer configuration with different velocities above and below the splitter plate can produce a concentrated single row of vorticies with like sense of circulation. The nature and the strength of such vortices depends on the ratio of the higher to

lower flow speed as well as on the distance from the onset of vortex formation. Various studies have been done on "two-dimensional" or transverse vortex interactions with a flat wall and a corner/leading edge as well as longitudinal vortex interaction with a plane wall and a wing (Bushnell 1984). All the related references are listed in Bushnell's review and will not be covered here; only the research in the area of concentrated vorticity at a single frequency interacting with various bodies will be addressed.

The vortex-corner impingement case was studied by Knisely and Rockwell (1979). They found that the interaction dynamics were very sensitive to the alignment between the corner and the vortex. In the case where the corner and vortex were nearly aligned, "severing" of the vortex and generation of "counter vorticity" on the vertical wall occurred. They also found that the feedback from the leading edge influenced the vortical structure upstream; the vortex diameter was increased.

An interesting study of an impulsively generated vortex pair, interacting with a thin flat plate, was done by Homa and Rockwell (1984). In the case of plate offset,where the outer layer of one of the vortices of the vortex pair impinged on a thin flat plate, there was flow separation leading to formation of a secondary vortex occurred. Once generated, the primary and secondary vortex pair travelled together upstream. At the same time, there

occurred another type of secondary vortex formation, leading to a primary vortex-secondary vortex pair which travelled down to the right of the impingement location. Similar to the previous case of distributed vorticity-edge interaction, the secondary vortex formation plays a crucial role during the primary vortex-edge interaction process in other configurations. Both Ziada and Rockwell (1982) and Kaykayoglu and Rockwell (1985, 1986a) studied the case of vortex-thin leading edge interaction. Ziada and Rockwell found that, similar to the case of vortex-corner edge interaction, the alignment of the plate leading-edge and the vortex center had a strong influence on the interaction process. Within a range of offset, the primary vortex interaction with the leading-edge produced a secondary vortex of opposite circulation on the lower surface of the leading-edge. The frequency of this shedding process coincided with the incident disturbance frequency. The strength and the scale of the secondary vortex was greater for the case where the center of the incident vortex passed above the leading-edge. A more detailed visualization of the interaction process was performed by Kaykayoglu and Rockwell. A hydrogen bubble wire was mounted with one end in the surface of the leading-edge; corresponding formation of the secondary vortex, below the edge, was seen more clearly. This showed a "sweeping" of the flow from the top to the bottom surface. This sweeping of the viscous layer about the tip was caused by a strong induced flow between the primary vortex and the tip; this process directly led

to the formation of a secondary vortex. Detailed pressure measurements in the tip region revealed high pressure amplitude due to the migration of fluid from the upper to lower surface of the edge. The interaction process led to maximum pressure amplitude, rather than a minimum occurring at the tip, as in the case of distributed vorticity-edge interaction. On the lower surface of the leading-edge, the fluctuating pressure field exhibited wavelike motion due to the convection of the secondary vortex instability; this is shown by the increasing phase downstream of the tip. In contrast, along the upper surface, there was nearly constant phase of the pressure field in the streamwise direction; this led to large local loading of the edge.

Booth and Yu (1984) reveal several interesting features of vortex street-blade interaction. They showed that the structure of the wake was altered as a function of blade position; also, the changes in blade loading were related to the vortex trajectories.

Concentrated vorticity at multiple frequencies. In many practical situations, the concentrated vorticity field contains more than one concentration of vorticity with a number of discrete frequency components. Such multiple concentrated vorticity, upon interaction with the edge, induces a modulated pressure wave with several spectral components along the surface of the edge. Kaykayoglu and Rockwell (1986b) investigated the case of a planar jet undergoing transverse modulations. This flow field generated remarkably ordered patterns of multiple vortex interaction in the vicinity of the edge. In one case, with increasing time, the small scale vortices passed beneath the large scale vortex along the lower surface of the

edge. When there was a finite length scale between the upstream separation boundary and the leading edge, remarkably repeatable patterns of incident vortices generated well-defined spectral components in the edge region. The spectra of the pressure fluctuations along the bottom surface of the edge showed that components $\beta/3$, $2\beta/3$ and β were predominant; β corresponds to the rate at which the vortex formed in the jet shear layer, i.e. the most unstable frequency of the shear layer. In contrast, spectra at the tip of the edge showed that the first harmonics of these components were predominant. Hence, in the near tip region, the predominant spectra components changed drastically as a function of streamwise distance. Much like the single frequency cases, the edge offset, relative to the incident shear layer, had strong effect on the vortex interaction patterns. In the case of edge offset where direct impingement of the shear layer vortices upon the edge occurred, the most unstable frequency of the shear layer β dominated the low frequency components.

Concentrated streamwise vorticity. In contrast to the previous case of the two-dimensional, transverse vorticity field, this type of incident vorticity field is predominantly oriented in the streamwise direction. This orientation involves an inherently three-dimensional flow structure such as a wing tip vortex. Interaction of a tip vortex with airfoils has been studied by McAlister and

Tung (1984). They found that the mean angle of attack of airfoil α strongly affects the stability of the vortex core following the impingement process. The vortex core may remain stabilized during the impingement, or show an instability downstream of the leading edge or even at the upstream portion of the airfoil (α=4°, 14° and -12° respectively). In general, they found that the pressure gradient from streamwise vorticity upstream of the leading-edge led to premature stall along the airfoil; a larger strength vortex closer to the surface caused stalling to occur closer to the leading edge. Ham (1974),in his investigation of blade-vortex interaction,also emphasized the importance of spanwise pressure gradients induced by the tip vortex in causing laminar leading-edge separation; this led to an early stall or turbulent trailing-edge separation. Patel and Hancock (1974) found that the proximity, or offset, of the tip vortex core with respect to the leading edge had a strong effect on the onset of instability of the tip vortex itself as it interacted with the leading-edge of the blade or airfoil. Far away from the airfoil the tip vortex core passed by undisturbed, but as its trajectory moved forward to the stagnation region of the airfoil, it experienced onset of instability well upstream of the leading-edge interaction region. Kramer and Rockwell (1984) investigated the evolution of tip vortices and interactions with thin plates. Using three hydrogen bubble timelines located upstream of the leading-edge of the plate, a detailed visualization of the

interaction process was done; upon interaction with the plate, the incident tip vortex was split at an off-center location. Following the splitting process, the major share of the incident vortex was distorted and moved to the left side of the plate. Even though secondary vortex formation could not be seen clearly, the onset of its formation was suggested by the strong curvature of the time-lines closest to the plate. Meanwhile, on the right side of the plate, a thick layer of retarded fluid with no apparent concentration of vorticity was formed.

Overview and Proposed Research. In all the previous studies of coherent vorticity field-edge interactions, many common features can be found: an unsteady separation process and subsequent secondary vortex formation; a relation between the instantaneous pressure field and the nature of secondary vortex generation; and dependence of the interaction mechanism on the offset between the incident shear layer at the body.

This investigation will study the case of a concentrated vorticity field at a single frequency, interacting with a finite thickness leading-edge. The concept of the investigation will be similar to those of Ziada and Rockwell (1982) and Kaykayoglu and Rockwell (1985) except a finite thickness edge instead of a thin leading edge will be used. Detailed flow visualization studies will be done to determine the effect of edge scale and offset on

the vortex-leading edge interaction. Since the fluctuating pressure field in the edge region plays an important role in the impingement process, detailed amplitude and phase measurements will be performed. To minimize the effect of possible three-dimensionality of the flow field and the end-wall effect on the pressure measurement, the pressure taps will be aligned in a single row; this is in contrast with the V-shaped staggering of the pressure taps of the Kaykayoglu and Rockwell set-up. A simultaneous pressure measurement-flow visualization technique, successfully used by Kaykayoglu and Rockwell (1985), will be used to construct the instantaneous pressure field on the surface of the edge. Through these various experiments, the relation of the pressure amplitude and phase variation to the vortex-edge distortion process will be determined. A detailed description of the experimental set-up and techniques are given in the subsequent section of this report.

EXPERIMENTAL SYSTEM AND TECHNIQUE

In order to investigate the mixing layer-generated vortex and its interaction with a leading edge, water was chosen as a fluid medium. This working fluid allowed detailed flow visualization and also avoided possible acoustic-instability wave coupling. The main test section, 30.5 cm wide by 45.7 cm deep, was located along the closed circuit water channel (Fig. 1). In order to minimize disturbances from the side and floor wall-generated boundary layers, a secondary test section, 24 cm wide and 45.7 cm deep, was inserted within the main test section (Fig. 2). Both the main test section and the secondary test section insert were made of plexiglass to allow detailed visualization studies.

A honeycomb flow straightener and a splitter plate were used to generate a well defined two-dimensional mixing layer of two uniform streams within the test section (Fig. 2). Details of the mixing layer section are given in Ziada and Rockwell (1982), hereafter referred to as Z-R. The unstable mixing layer grows and eventually evolves into a well-defined two-dimensional vortex which subsequently impinges on a leading edge. As shown in Z-R, the structure of the generated vortex remains coherent within the region of interest. During the course of the experiment, the impingement length and the flow speed were kept constant. The flow speed was fixed at U_1=18.35 cm/s for the high speed upper layer and U_2=6.44 cm/s for the

low speed layer (Fig. 2). This freestream velocity ratio of high to low speed layer $U_1/U_2=2.85\pm0.05$, provided well-defined vortices in the downstream mixing layer with laminar boundary layers at separation having momentum thickness $\theta_{o1}=0.62$ mm and $\theta_{o2}=0.08$ mm, θ_o representing their sum [see p. 81 of Z-R, 1982]. The corresponding Reynolds number based on momentum thickness was given as $Re(\Delta U,\theta_o) = (U_1-U_2)\theta_o/\nu = 157$ or $Re(U_1,\theta_o) = U_1\theta_o/\nu = 239$ in Z-R. The impingement length was fixed at $L/\theta_o = 60$ (L=7.8 cm) from the trailing-edge of the splitter plate. This impingement length, which was used by Kaykayoglu and Rockwell (1985), hereafter referred to as K-R, generated two-dimensional vortex structure impinging upon a very thin leading-edge. Z-R also showed that at this impingement length, and previously noted flow conditions, there was no free surface effect on the self-sustained oscillation of the mixing layer. Both in Z-R and K-R, the structure of the incident vortex and velocity profile of the flow field is discussed in detail and hence will be omitted here. It is, however, sufficient to say that the structure of the incident vortex is invariant with the transverse offset of the leading-edge; moreover the distribution of fluctuating velocity at the vortex frequency $u_{rms}(\beta)$ where β is dimensionless frequency, agrees well with the Stuart's nonlinear inviscid model (1967) of vorticity concentration of $\alpha=0.7$. Hence vortex-leading edge interaction can be studied with the safe assumption that the upstream flow conditions are not affected by the various values of vortex-edge offset.

For the experiment, three different types of leading-edges were used. The first type of leading-edge was a pair of NACA 0012 airfoils having a length of 12.7 cm and 6.4 cm machined from plexiglas block. It was used for preliminary visualization of the vortex-leading edge interaction. The airfoil was free-mounted in the test section as shown in Fig. 3. This setup allowed a quick change in the angle of attack for the series of flow visualizations. The various angles of attack were 0°, 10°, -10°, and -5°. The second type of leading edge was a 5:1 elliptical leading edge with semi-infinite length trailing edge. Three different edge thicknesses were machined from Plexiglas by Bridgeport CNC machines. These various thickness (¼", ½", 1½") leading edges were used only for visualization studies, in order to determine the effect of edge scale on the vortex-leading edge interaction. These leading edges were rigidly mounted on a carrier system to allow adjustment along the direction of the flow as well as across the flow (Fig. 2). The leading edge-plate assembly was suspended in the flow field by three brass supports from the carrier which slides along the top edges of the side walls of the test section.

For pressure measurements, it was necessary to design a special leading-edge, having a thickness of one inch and an elliptical (5:1) shape. This leading edge contained 26 pressure taps, 12 along the top surface, 12 along the bottom surface, and one at the tip of

leading edge. The necessary valving and plumbing for the pressure measurement at the individual taps was similar in concept to the leading edge used by K-R, but was constructed much differently (Figure 5). The elliptical leading edge section was initially machined from one piece of plexiglass (1" thick, 9" wide and 5" long). Then the leading edge was cut into three pieces to facilitate plumbing of 1/16" ϕ brass tubes to transmit the pressure signals from the surface pressure taps to the pressure transducer via valves. The 1" wide center section contained 26 pressure taps along the elliptical contour. To avoid possible wake effects from one tap to the next, all the taps were staggered by 1/8". Since near the tip, larger pressure gradients were presumed to exist, more pressure taps were concentrated there. The relevant dimensions and detailed drawing of the pressure tap locations are shown in Fig. 5 [4:1 scale]. The pressure taps were chosen to be 1/32" in diameter in order to minimize the error in pressure measurement. For this size opening and water as a fluid medium, Vollery (1961) showed that the error in stream-pressure measurement for steady flow, in percent of dynamic head ($1/2\ \rho U^2$), was less than 0.4%. There will be also some error in measurement near the tip of the leading edge due to sharp inclination of the pressure tap hole with respect to the surface. Erwin (1964) showed that for the case of 45° inclination of the tap, static pressure variation of 0.4% of dynamic head can result.

The remaining two side pieces of the elliptical leading edge were hollowed out to accommodate the brass tubing (Fig. 4). Once the sections of tubing were fitted to the centerpiece, all three

pieces were glued back together and filled with slow curing epoxy to increase the overall stiffness, and therefore its natural frequency. Individual tubes were then connected to the valve assembly body (Fig. 6). The small brass valves in each pressure channel, located downstream of the tap, allowed selective measurement of the pressure at the desired location. All the pressure signals were then fed into a common pressure manifold where a single pressure transducer monitored the selected pressure signal (Fig. 7). The completed assembly of the leading edge and pressure measurement section, including the mounting plate, is shown in Fig. 8.

For the pressure measurements, a Kulite XCS-190-2D differential pressure transducer with a Paralene coated diaphragm was selected for its small size and high natural frequency of 100 kHz. The pressure signals were amplified by a Tektronix, model TM 502 differential amplifier and then filtered with Krohn-Hite, model 3700 bandpass filter. Nominal filtering frequencies were 0.5 Hz for the low cut off point and 6 Hz for the high cutoff point. The nominal frequency of interest during the measurement was around 4 Hz. Signals were monitored by a Tektronix 5223 Digitizing Oscilloscope. A DEC-MINC mini-computer with 28 K ram and DEC-PDP 11/23 were used for real-time spectral analysis. In order to run the cross-spectrum analysis to obtain amplitude and phase information of the pressure signal, a reference signal had to be used. For the reference signal, a DISA hot wire probe, connected to a DISA 55D01 constant temperature

anemometer, was used. The pressure and the velocity signals were fed into the microcomputer (Fig. 9). Both signals were first digitized by the MINC minicomputer and the amplitude and relative phase information were obtained by cross-spectral analysis. The same type of Fast-Fourier Transform (FFT) program used by Z-R and K-R allowed the cross-spectral analysis between velocity and pressure signals. A total of 512 sampling points were allowed by the program for any given run. The sampling interval of 0.039063 seconds was used to obtain 0.05 Hz resolution. This sampling interval provided a sampling frequency of 13 Hz which was above the Nyquist frequency. Hence the aliasing effect was avoided for all cases. The concept of cross-spectral analysis is shown in Fig. 10. Ensemble averaging was not carried out in order to minimize possible error in phase data. Since the phase difference from the FFT, $\phi_{\tilde{p}}$ active- $\phi_{\tilde{p}}$ reference, lies either in the range of 0 to π or 0 to $-\pi$, an actual value close to π may correspondingly indicate a value close to π , while a subsequent run may give an indicated value close to $-\pi$. This will result in an ensemble-averaged phase value close to zero. In order to avoid this problem, data acquisition and reduction were repeated separately and then averaged with proper phase interpretation. The filters also introduced some phase distortions in the signal which may lead to error in the cross-spectrum phase data. This, however, can be avoided in the case of cross-spectral analysis by simply

putting both filters for pressure and velocity signals to the same low and high cutoff frequencies. Since the cross spectrum phase data is the difference in phase angle between the active and reference signal, any common phase shift produced by the filters at the same setting will cancel each other out. There was also a major concern that the long and small diameter brass tubes, transmitting the pressure signals from the taps to the pressure transducer, may introduce undesirable amplitude attenuation and phase distortion. A calibration scheme was devised to check this effect. An eccentric motor drive was used to displace mass inside a fixed volume container to produce static pressure variation. A reference pressure transducer was mounted rigidly next to the active tap and both signals were processed via the same instrumental setup in order to obtain cross-spectral data (Fig. 11). Two taps (No. 13 & No. 1; Fig. 12) were checked since they represented the two extreme cases, i.e. shortest and longest tubes. Both taps were swept with a sinusoidal input signal of varying frequency from 0 to 5 Hz, corresponding to the frequency range of interest. The result showed minimal amplitude attenuation in the case of tap No. 1 (longest tube) and virtually no amplitude distortion for tap No. 13 (shortest test tube). The result also showed a maximum phase distortion of 0.18π at 5Hz for tap No. 1 and 0.05π for the tap No. 13 (Fig. 12). Both results showed that the original concern was unfounded and the resulting errors were minimal.

In order to obtain detailed insight into the vortex-edge interaction mechanism, various means of flow visualization were used. To clearly see the vortex rollup and its subsequent interaction with the leading edge, hydrogen bubble timeline visualization was extensively utilized. Hydrogen bubble time lines were generated by a platinum wire (0.001"-0.003" ϕ) positioned vertically on a wire probe mount. Since the technique of hydrogen bubble visualization is well known, only the pertinent details will be discussed.

The necessary lighting for illuminating the hydrogen bubble lines was provided by two 90 watt strobascopic lights (Instrobe 90). These strobes were synchronized to the Instar video system to operate at a flash duration of ten microseconds at a triggering frequency of 120 Hz. The Instar video system was capable of taking video pictures at a framing rate of 120 frames per second. The Instar system had horizontal and vertical sweep frequencies of 25.2 kHz and 120 Hz respectively, with a resolution of 250 lines. An overall view of the typical hydrogen bubble visualization is shown in Fig. 13. Once the video sequences were taken, they were played back frame by frame and then the Nikon F-3 35mm SLR was used to take the final photos from the video screen.

The hydrogen bubble wires were located in various positions in order to see the details of the flow field along the top and bottom surfaces of the leading edge (Fig. 14a,b). Sometimes, instead of a straight wire, a notched wire was used to generate lines of hydrogen

bubbles. This technique is similar in principal to that of Schraub et al (1965), but instead of selectively insulating the wire, a notched wire was used to generate the hydrogen bubble lines. These lines can show the fluid movement normal to the flow. By locating the notched wire at the tip of the leading edge rather than well upstream of it, the secondary vortex formation or interaction downstream of the edge can be seen more clearly (Fig. 14c).

Sometimes food-dye color was injected into the flow field for preliminary visualization and also to monitor the flow field during measurements. Since the food-dye color has relatively neutral buoyancy, laying it on the surface of the splitter plate generated continuous streaklines (Fig. 14d). The dye injection technique was also necessary in the case of simultaneous pressure-flow visualization.

In order to obtain the time-phase relationship between the cross spectrum data and the flow visualization, a split-screen, simultaneous pressure-flow visualization had to be done. The experiment setup is clearly illustrated in Fig. 15. Two cameras simultaneously monitor the streakline from the dye injection and the pressure signal displayed on the oscilloscope. As mentioned previously, since the electrical pulsing of the hydrogen bubble line disturbs the pressure signal, only the dye injection could be used. The required lighting was provided by a 1000 watt constant intensity studio light, diffused by semi-transparent white plastic sheet (Fig. 15). Once the cross-spectrum phase data and the flow visualization were correlated,

instantaneous pressure plots, along the leading edge surface, were constructed for given time t. The plates and the corresponding pictures were physically related through this technique. This technique was used successfully by K-R and further details can be obtained from that paper (K-R 1985). Unlike the previous case of cross-spectrum analysis, here the phase distortion caused by the filter played a significant role. Since only one signal (pressure) is being processed through the filter, the high and low cutoff frequencies had to be set in such a way as to minimize phase shift from the visualized data and the pressure signal. A signal generator was used in conjunction with the mini-computer to calibrate the filter settings. A sinusoidal signal of known phase and frequency was processed through the filter-amplifier setup. By checking the phase angle of the output signal through the cross-spectral analysis, it was possible to obtain the proper setting of the frequency cutoff points for minimum phase shift.

VORTEX INTERACTION WITH A LEADING-EDGE OF FINITE THICKNESS

Preliminary Visualization of a Concentrated Vorticity-edge Interaction at a Single Frequency

As discussed in the introduction, the case of vortex-thin leading-edge interaction was studied in detail by Z-R and K-R. In this investigation, the case of interaction between concentrated vorticity field and a finite thickness leading-edge was investigated. The visualization study was performed for two different geometries; a 5:1 elliptical leading-edge and a finite length airfoil (NACA0012). This preliminary visualization showed that the vortex-edge interaction process was substantially different from the thin leading-edge vortex interaction. In the case of thin leading-edge vortex interaction process there was a clear "splitting" of the incident vortex with fractions of it passing above and below the edge. The primary vortex interaction with the leading-edge produced a pronounced secondary vortex of opposite circulation on the lower surface of the leading-edge. K-R found that there was sweeping of the viscous layer about the tip from the top to bottom; this process, caused by a strong induced flow between the primary vortex and the tip, directly led to the formation of a secondary vortex.

In the case of a vortex incident upon a 5:1 elliptical leading-edge, a substantially different interaction process takes place. Figure 16 show a primary vortex, rotating in the clockwise direction, impinging on the leading edge. The vortex is initially in line with

the edge (i.e. $\xi/2T=0$ where ξ is the transverse edge-vortex offset and 2T is the edge thickness); however, as it approaches the leading-edge, its center moves slightly below the centerline of the leading-edge. This slight deviation of the incident vortex causes the major portion of it to dive below the leading-edge. In the third photo, one can see the start of the primary vortex-induced flow separation from the underside of the leading-edge. The separation process leads to formation of the secondary vortex. Once formed, the secondary vortex moves downstream with the same phase speed as the corresponding primary-vortex. Meanwhile, along the upper surface, only a small fraction of the incident primary vortex is swept upward. Since the mean velocity of the fluid above the leading-edge is still greater than the velocity of the fluid below the leading-edge, the portion of the primary vortex above the edge is rapidly accelerated along the upper surface.

Figure 17 shows a simplified schematic of the incident vortex wave and the lower surface pressure wave at the leading-edge. This simplified diagram shows that the downstream travelling wave has characteristic wavelength λ_ℓ and convective speed C_ℓ, which can be linked to the characteristic incident vortex wave (λ_v, C_v). Figure 18 shows a wider view of the flow field upstream of the leading-edge. Instead of using finely-pulsed hydrogen bubble lines, a block of hydrogen bubbles is used to show the successive interaction of the vortices with the leading-edge. The sequence of the photos shows

that the wavelength of the primary vortices is of the order of twice the thickness of the leading-edge. It is interesting to note that the secondary vortex, once formed, continues to travel along the bottom surface of the leading-edge as it is swept downstream, nested within its corresponding primary vortex. Once again, one can clearly see that only a fraction of the primary vortex is swept above the leading-edge allowing the distorted primary vortex to remain relatively intact along the lower surface.

Figure 19 shows the same interaction process as in Figures 16 and 18 but a notched wire, instead of a straight wire, is used to generate the lines of hydrogen bubbles. As discussed in the previous section, this technique can show the fluid movement normal to the flow. The wire is located at the tip of the leading-edge rather than well upstream of it. Locating the wire well upstream of the edge may show the primary vortex roll-up and the initial interactions with the leading-edge, but locating the wire at the tip of the edge brings out the features of the secondary vortex formation and interaction occurring downstream of the edge more clearly. The first photo shows the continued roll-up of distorted primary vortex as well as the formation of a secondary vortex on the lower surface of the edge. The following photos show that this primary-secondary vortex pair travels downstream along the lower surface of the edge, in much the same manner as shown in previous photos. However, on the upper side of the leading-edge, one can only see a slight deviation of the

streakline patterns. There is no evidence of any further roll-up of the primary vortex on the upper side. Clearly most of the incident vortex is swept below the leading edge as suggested in Figures 16 and 18.

These series of photos suggest that when the scale of the primary vortex is sufficiently small with respect to the thickness of the leading-edge, a major portion of the incident vortex will dive below the tip rather than "split" into two primary vortices as in the case of thin leading-edge vortex interaction. There is also no "sweeping" of the fluid from the upper to lower surface of the edge, at least for the vortex scale examined here. The Reynolds number based on leading-edge thickness and average velocity $(U_1+U_2)/2$ for the case examined was 2400. At this Reynolds number, the leading-edge separation leading to the secondary vortex formation was caused only by the adverse pressure gradient of the incident vortex.

In the next series of the preliminary investigation, a finite length airfoil (NACA 0012) replaced the 5:1 elliptical leading-edge. The thickness of the leading edge of the airfoil was about one-half that of the elliptical leading-edge. The upstream flow conditions and the scale of the incident primary vortex were kept constant. The Reynolds number based on airfoil chord C and average velocity $(U_1+U_2)/2$ was 7740. Figure 20 shows a vortex incident upon the airfoil at 0° angle of attack with respect to the free stream. A pulsed wire technique was used to obtain long duration pulses with shorter duration timelines embedded within them. The first photo shows the front edge of the bubble lines

being distorted by the leading-edge of the airfoil. The second photo clearly shows the flow speed difference between the upper and lower surface of the airfoil; the front edge of the bubble patch has advanced further on the upper surface than the lower surface. The fourth photo clearly shows the splitting of the primary vortex on the upper and lower side of the airfoil. The upper part of the primary vortex continues to grow and move close to the surface of the airfoil, while the bottom part of the primary vortex induces flow separation. In the subsequent photos, the formation and growth of the secondary vortex is clearly evident.

In comparison with the thicker 5:1 elliptical leading-edge, there is a well-defined "splitting" of the incident vortex and formation of a relatively large-scale secondary vortex. Figure 21 examines the same interaction process but focusses on the growth of the primary vortex along the upper side of the airfoil using the pulsed bubble wire located at the tip of the leading-edge. This was done to check whether the primary vortex along the upper surface continues to "roll-up" as it moves downstream. This continued roll-up process is evident by following photos 1 through 4. The primary vortex, though distorted continues to roll-up despite the presence of the solid boundary and stays along the upper surface of the airfoil.

Next, in order to determine the effect of angle of attack on the interaction process, various values of angle of attack α were tried (α=-10°, -5°, 10°). Figure 22 shows the case of α=-10°; this

relatively large negative angle of attack induced early flow separation from the leading-edge region. The photos show the secondary vortex formation and subsequent breakdown of the primary-secondary vortex pair. Figure 23 shows closeup visualization of the same interaction process. One can see that once the secondary vortex formation occurs, the primary-secondary vortex pair moves down away from the surface of the airfoil; this is in contrast to Figure 21 where the primary-secondary vortex pair moves along the surface of the airfoil. The scale of the secondary vortex in this case also seems to be of the order of the primary vortex. This can be seen in Figure 23 as well as in Figure 24 where a wider view of the interaction process is shown.

If the wire is located at the tip of the airfoil, a more interesting detail in the flow structure can be examined. Figure 25 shows a case of α=-5°. This series shows the nature of the unsteady separation zone in the leading-edge region prior to and after the arrival of the incident vortex. In the first photo, flow separation due to the adverse pressure gradient caused by the negative angle of attack can be seen. This process takes place before the arrival of the primary vortex. In the third and subsequent photos one can again see a separation process from the leading edge, this time due to the primary vortex. This process leads to the formation of two secondary vortices along the bottom surface of the airfoil. In the fifth photo one can see simultaneously the distorted primary vortex along

the top and bottom surface of the airfoil as well as the two secondary vortices, one due to angle of attack α and the other to the outside separation from the edge caused by the primary vortex-edge interaction. In the sixth and seventh photos, one can see that the stronger secondary vortex due to the primary vortex entrains the first secondary vortex and the two combine while the distorted primary vortex continues to travel along the upper and lower surfaces. Figure 26 shows the case of positive angle of attack (α=10°). The first photo of the series shows the initial reaction of the incident primary vortex as well as the previous distorted primary vortex on the upper side. The second photo shows the splitting of the primary vortex and continued growth of the scale of distorted primary vortex. The sixth and seventh photos show smaller scale vortex shedding upstream of the distorted primary vortex along the upper surface. It it not clear, however, whether this secondary vortex formation is due to the angle of attack or induced by the primary vortex.

Effect of Edge Thickness Scale on the Interaction Process

The previous studies of the vortex-leading edge interaction process seem to indicate the importance of edge thickness (scale) relative to the incident vorticity field on the interaction process. To date, however, no detailed studies have been done to actually determine the effect of edge thickness scale on vortex-leading-edge interaction. The preliminary visualization seems to indicate that there is a direct relationship between the edge thickness and the incident vortex distortion process. In the case of a 5:1 elliptical

leading-edge, the majority of the incident primary vortex passes below the edge surface. On the other hand, in the case of the airfoil having half the thickness of the 5:1 elliptical leading-edge, there was a clear "splitting" or "severing" of the incident vortex much like the case of thin leading-edge-vortex interaction. In order to investigate the effect of edge scale further, three 5:1 elliptical leading-edges of different thickness were used for visualization studies (2T=1/4", 1/2", 1 1/2"). Since the physical thickness of the edge itself, without considering the relative scale of the incident vorticity field, is meaningless, we introduce a parameter known as the "vorticity thickness", designated by $\Delta\omega$. The vorticity thickness can be defined as,

$$\Delta\omega = \frac{\Delta U}{\left(\frac{d\bar{u}}{dy}\right)_{max}}$$

where ΔU is the velocity difference U_1-U_2 between the upper and lower surface of the mixing layer and $\left(\frac{d\bar{u}}{dy}\right)_{max}$ corresponds to the maximum slope of the mean velocity profile across the mixing layer. Z-R have experimentally measured the mean velocity profile across the wake region of the mixing layer and fount it to be in good agreement with the exact solution of the Stuarts nonlinear model at vorticity concentration parameter of $\alpha=0.7$. From the graph of y/θ_R vs. $2(\bar{u}-U_a/\Delta U)$, a maximum slope $(d\bar{u}/dy)_{max}$ can be found graphically. Then, using the previous definition, the vorticity thickness $\Delta\omega$ can be calculated.

For the given experimental conditions, the value of vorticity thickness $\Delta\omega$ turns out to be approximately 9 mm. If the exact solution of the mean velocity profile from Stuart's model,

$$\bar{u} = U_a + \frac{\sinh(2\pi y/\lambda)}{[1-\alpha^2+\sinh^2(2\pi y/\eta)]^{\frac{1}{2}}}$$

is used to obtain the maximum slope,

$$(d\bar{u}/dy)_{max} = \Delta U \frac{\pi}{\lambda(1-\alpha^2)^{\frac{1}{2}}}$$

then the theoretical value of $\Delta\omega$ can be calculated. Using the vorticity concentration parameter of α=0.7 and the experimentally measured wavelength λ=35 mm for the given incident vorticity field, $\Delta\omega$ is found to be approximately 8 mm. This value is in good agreement with the previously obtained $\Delta\omega$ of 9 mm.

The circulation of the incident vorticity field can also be easily calculated by integrating across the flow over one wavelength λ to obtain,

$$|\Gamma| = \lambda(U_1-U_2) = \lambda\Delta U$$

The absolute value of the circulation Γ is calculated to be 41.7 cm^2/s. The value of the circulation can be nondimensionalized by using previously obtained value of $\Delta\omega$,

$$\Gamma^* = \frac{|\Gamma|}{\Delta\omega\Delta U} = \frac{\lambda}{\Delta\omega} = f(\alpha) = 3.9$$

where Γ^*, a nondimensionalized circulation becomes a function only of α, the vorticity concentration factor. Now the physical thickness of the edge can be transformed to the more meaningful nondimensionalized value of $2T/\Delta\omega$, where 2T is the actual thickness of the leading-edge as stated previously. The edge thickness can also be nondimensionalized with respect to θ_R, the local momentum thickness at the streamwise station $11\theta_o$ upstream of the leading-edge (θ_o is the sum of momentum thickness at the higher-speed side (θ_{o1}) and the momentum thickness at the lower speed side (θ_{o2})). The corresponding values of $2T/\theta_R$ for the three edge thickness are 3.30, 6.7, and 20.1. Figure 27 shows the vortex interaction with 5:1 elliptical leading-edge for $2T/\Delta\omega=0.7$. In comparison, the elliptical leading-edge used in the preliminary visualization study would correspond to $2T/\Delta\omega=2.8$. One can clearly see the dramatic effect of the edge thickness (scale) on the interaction process. In this case, the primary vortex splits almost equally above and below the leading-edge. This is in sharp contrast to the thicker edge of $2T/\Delta\omega=2.8$. The secondary vortex formation below the edge surface, however, does not differ markedly from the previous case. The lower part of the distorted primary vortex induces the formation of secondary vortex and the primary-secondary vortex pair travels downstream relatively intact. In the case of thicker leading-edge of $2T/\Delta\omega=1.4$, almost the same interaction process takes place. Figure 28 again shows the "severing" of the incident vortex and subsequent formation of the secondary vortex along the lower surface of the leading-edge. One can note that

even at this thickness (scale), the apparent size of the vortex seems to be of the same order as the thickness of the leading-edge.

However, when the edge thickness is substantially increased as in the case of $2T/\Delta\omega=4.2$, a much different interaction process takes place. Figure 29 shows that the incident primary vortex is no longer severed by the leading-edge. For that matter, all of the (marked) incident primary vortex dives below the leading-edge and though dis torted, remains relatively intact as it travels downstream. The formation of the secondary vortex, however, does not seem to differ much from any of the previous cases. Figure 30 shows the overview of the effect of edge thickness on the interaction by comparing three different thicknesses side by side. In conclusion, one can see that when the thickness of the leading-edge remains relatively small, the interaction process emulates that of the thin leading-edge interaction process, except that there is no longer "sweeping" of the flow from the top to the bottom. However, when the thickness scale becomes relatively large with respect to the incident vortex, then a different process takes place; most or all of the incident vortex dives below the surface of the leading-edge. The formation and the scale of the secondary vortex, on the other hand, do not seem to be effected by the edge thickness scale. Judging from the previous studies, the edge offset rather than the thickness (scale) seems to have a more drastic effect on the formation of the secondary vortex.

Effect of Edge Offset on the Interaction Process

As discussed earlier, Knisely and Rockwell (1979) found that the interaction dynamics of the vortex-corner impingement case were very sensitive to the alignment between the corner and the vortex. In the case where the corner and the center of the incident vortex were nearly aligned, "severing" of the vortex and generation of the secondary vortex occurred on the vertical wall. Z-R also found that the alignment of the thin leading-edge and the incident vortex center had a strong influence on the interaction process. Z-R found that the strength and the relative scale of the secondary vortex was greater for the case where the center of the incident vortex passed slightly above the leading-edge. Clearly all these studies have shown that the edge offset relative to the oncoming vortex plays an important role in the interaction process.

For this investigation, cases of three different offsets for the 5:1 elliptical leading-edge were examined. The edge offset, relative to the center of the incident vortex, is denoted as ξ (Figure 17) and is nondimensionalized with respect to the edge thickness 2T. The nondimensional thickness for the 5:1 elliptical leading edge used for this study is $2T/\Delta\omega=2.8$. Figure 31 shows the interaction process for zero offset case of $\xi/2T=0$. This series of photos is very similar to that of Figures 16, 18 and 19. A block of hydrogen bubble lines is generated upstream of the leading-edge to show the incident vortex and the subsequent edge-impingement process. One can clearly

see the distortion of the incident primary vortex and subsequent separation of the flow near the tip of the leading-edge. The formation of the secondary vortex is well defined in the latter part of the series. For this offset case and thickness scale, all of the incident primary vortex dives below the leading-edge and the "splitting" process does not occur. Figure 32 shows a series of photos of finely pulsed hydrogen bubble lines generated at the tip of the leading-edge. One can see a slight distortion of the boundary layer above the leading-edge but clearly no part of the primary vortex is visible. The secondary vortex, once generated, stays close to the lower surface of the edge and travels downstream, nested within the primary vortex. Figure 33 shows the same interaction process using the continuous hydrogen bubble lines instead of finely pulsed lines. Not much more information is evident in this series except one can clearly see the secondary vortex generation and the boundary layer development above the leading-edge.

In the next series of pictures a slightly positive offset case of $\xi/2T=0.1$ is examined. Figure 34 shows a sequence of photos somewhat similar to the previous series. There is, however, some difference between the two offset cases. In this case of slightly positive offset, the generation of the secondary vortex is suppressed and the roll-up process of the secondary vortex is not as well defined. Again, all of the incident primary vortex passes below the leading-edge surface and no action can be seen above the edge. Figure 35

shows that, in this offset case, the flow along the upper surface of the leading edge is not at all disturbed by the vortex impingement. The secondary vortex also does not complete the roll-up process and disintegrates downstream of the edge. A similar process can also be seen in Figure 36. Thus, much like the findings of Z-R, the positive offset case produces a much less well-defined and weaker secondary vortex and all of the incident primary vortex passes below the leading-edge. Also, as is evident from the pictures, a slight change in the offset produces a significantly different interaction process, i.e. for the case of negative offset corresponding to $\xi/2T = -0.4$.

Figure 37 shows that for the case of negative offset the incident vortex is relatively undisturbed by the solid boundary. The primary vortex moves away from the leading-edge as it travels downstream, and continues to roll-up. Figure 38 shows this process even more clearly. The primary vortex is relatively undistorted and rapidly moves away from the upper surface of the edge; as it travels downstream, there is no evidence of any secondary vortex formation at any time during the interaction process. The same information can also be gathered from Figure 39. It is not clear, however, why the incident vortex, instead of deforming against the solid boundary, moves away from the surface. Perhaps the incident vortex causes a separation at the tip of the leading-edge and the

ensuing rapid boundary layer growth moves it away from the surface. The pictures themselves, however, do not offer sufficient information to confirm this. In Figures 40, 41 and 42, all different offset cases are compared side by side for different hydrogen bubble visualization techniques. It is clear from these series of pictures that the edge offset, relative to the center of incident vortex, has a much stronger effect on the formation of the secondary vortex than the effect of edge thickness (scale). Now the effect of edge offset on the interaction process can be further studied by examining the mean and instantaneous pressures along the surface of the leading-edge.

Amplitude and Phase Variation of Pressure in Leading-Edge Region

The amplitude and phase distribution of the fluctuating pressure field along the lower and upper sides of the edge is obtained from the cross-spectral analysis described in the section on the experimental system and technique. Figure 43 shows the variation of the pressure amplitude and phase along the lower and upper surfaces of the leading-edge for the three different offset cases ($\xi/2T$ = 0, 0.1, -0.4) discussed previously. The corresponding pictures are representative photos taken at time t/T = 0 where T is the period of the vortex shedding cycle. Time t=0 is arbitrarily chosen as the instant when the incident vortex is just impinging on the leading-edge.

The upper and lower surface pressures are respectively denoted as $\tilde{P}_u$ and $\tilde{P}_\ell$. The value of $\tilde{P}_{max}$ corresponds to the maximum rms pressure value for each offset case. Symbol X represents the linear distance along the centerline of the leading-edge and is non-dimensionalized with respect to T, the half thickness of the edge. For the case of $\xi/2T=0$, along the upper surface, the pressure amplitude rapidly decreases along the downstream direction. The amplitude decreases so charply that beyond X/T=2.5 no meaningful information could be gathered. The phase $\phi_{\tilde{P}u}$, on the other hand, jumps by more than π along the tip region then remains relatively constant. In order to interpret this information we need to examine the following equation

$$C_{u,\ell} = f\lambda_{u,\ell} = 2\pi f/[d\phi_{u,\ell}/dx]$$

where C is the wave propagation or convective speed, λ is the wavelength and f is the frequency. Thus relatively constant phase ϕ or $d\phi_{u,\ell}/dx \simeq 0$ corresponds to very high propagation speed on the upper surface of the edge. This can be directly related to the physics of the flow. From the previous visualizations one can see that the major portion, if not all, of the incident primary vortex passes below the edge surface. Hence, along the upper surface there is no wavelike motion and from potential flow theory one can deduce that the upstream perturbation translates to a simultaneous loading of all the pressure taps along the upper surface of the edge. This, in turn, would lead to a seemingly constant phase along the upper surface. The lower surface, however, shows a markedly different result. The maximum pressure amplitude occurs at X/T=0.0 (steady

flow stagnation point), peaks again at X/T=0.4, and then decreases downstream. The reason for the second peak at X/T=0.4 may be due to separation and onset of the secondary vortex formation near that location. The phase, on the other hand, continues to increase downstream at the tip region. The wave propagation speed C_ℓ, calculated from the mean phase speed, agrees well with that value obtained from the actual visualization data. From the change in the slope $d\phi_\ell/dx$, one can see that the flow is initially accelerated at the tip region than is decelerated along the region of decreasing curvature (i.e. decreasing favorable pressure gradient).

The positive offset case of $\xi/2T=0.1$ produces a slightly different result. Along the upper surface, again there is a rapidly decreasing pressure amplitude and a relatively constant phase. The same explanation applies to this case as in the previous offset case. Along the lower surface, the phase data seems to be very similar to the no offset case. Again, the calculated wave propagation speed is in good agreement with the actual data obtained from the visualization. The pressure amplitude, on the other hand, differs slightly from the previous case; the maximum pressure amplitude, instead of occurring at X/T=0.0 occurs at X/T=0.1. This can be explained by noting that the slight positive offset causes the incident primary vortex to impinge slightly below the tip of the leading edge; this causes the peak pressure to occur slightly downstream of the steady flow stagnation point.

The last offset case of $\xi/2T=-0.4$ produces quite a different result. As expected, along the lower surface, the pressure amplitude rapidly decreases to a very small value and the phase variation remains relatively constant. Since no part of the incident primary vortex passes below the leading-edge, the same explanation as in the two previous cases can be applied. The vortex dynamics along the upper surface dominates the interaction. The maximum pressure amplitude occurs at $X/T=0.8$; this location corresponds to the primary vortex impingement region. Why there is such a sharp decrease in the amplitude past $X/T=2.0$ is not very clear. Perhaps the fact that the primary vortex moves away from the surface downstream of $X/T=2.0$ may explain the amplitude result. The phase variation, on the other hand, is very similar to those of two previous cases. The only difference is that instead of covering 8π, this case only covers 4π, indicating a substantially longer wavelength. The visualization result seems to confirm this observation. The reason for the drastic change in the wavelength may be attributed to the nature of the experimental set up which generates the mixing layer. Since the extreme negative offset forces the vortex to travel along the upper surface of the leading-edge, where the flow speed is substantially higher than that of below, elongation of the vortex wavelength may occur. In general, one can see that the resultant amplitude and phase variations along the edge surface for the three offset cases agree well with the physics of the flow and the visualization data.

Instantaneous Pressure Fields

Utilizing the same technique successfully employed by K-R, it is possible to construct the instantaneous pressure field on the upper and lower surfaces of the leading-edge at successive instants time of t; t=0 is chosen arbitrarily as the instant in time just before the distortion of the primary vortex due to the impingement process. In each composite showing the instantaneous pressure field, and corresponding flow visualization (Figures 45 through 62), the instantaneous distribution of the pressure waves along the upper and lower surfaces of the edge and the photos of the interaction process at that instant are given at five values of time t over the oscillation cycle period T (t=0, 1/5T, 2/5T, 3/5T, 4/5T). The symbol $\tilde{P}(x)$ denotes the rms pressure amplitude envelope which is a function of the distance x only and the $P'(x,t)$ denotes the instantaneous pressure which is a function of the distant x as well as the time t. The corresponding nondimensional distance along the centerline of the edge x/T is indicated on the pressure plot as well as on the photos. Figure 45 shows the case of $\xi/2T=0$. Along the upper surface, the pressure amplitude is relatively small and constant (i.e. no wavelike motion). On the other hand, along the lower surface, one can clearly see the propagating pressure wave as a function of time. The pressure plot corresponding to the third photo of flow separation at t=2/5T shows a maximum negative pressure near the separation point. As expected, the onset of the separation

process produces the maximum instantaneous pressure at that location. The lack of wave-like motion along the upper surface of the edge can be attributed to the major share of incident vortex passing below the edge.

Figure 46, for the case of $\xi/2T=0.1$, shows a similar result. Along the upper surface, the pressure amplitude is again very small and relatively constant. Along the lower surface the same basic propagating pressure wave as a function of time t can be seen. Comparing the plot of the two offset cases, however, one can see that the zero offset case seems to produce pressure waves of shorter wavelength evidenced by more cycles covered along the same distance. This is not evident in the corresponding photos. However, further downstream the positive offset case shows a faster advancing primary-secondary vortex pair relative to the zero offset case, reflecting the longer wavelength of the vortices.

The case of negative offset $\xi/2T=-0.4$ produces a similar result except that the wavelength is significantly longer than for the previous two cases. This time, the pressure amplitude along the lower surface is relatively small and constant. Again no wave-like motion can be seen since the phase remains relatively constant along the lower surface. The upper surface plot shows the peak pressure locations approximately corresponding to the centers of the incident vortices. One can also see that only about two cycles (or 4π) is covered along the upper surface. The corresponding pictures also

show the significantly longer wavelength between the vortices. In all offset cases, however, the frequency f remains relatively constant; only the wavelength changes. The remaining Figures 48 through 62 show the instantaneous pressure fields and corresponding three types of visualization of the flow field at three different offsets.

DISCUSSION AND CONCLUSIONS

Overall, the mixing layer generated vortex, interacting with either the 5:1 elliptical leading-edge or the finite-length airfoil, produces a different result from the interaction process involving a thin leading-edge. The interaction process for both the elliptical leading-edge and the airfoil leads to the distortion of the primary vortex and subsequent formation of a secondary vortex for the range of offset cases examined except for the negative offset case of $\xi/2T=-0.4$. The secondary vortex formation process differs from that of the thin leading-edge case. Unlike the thin leading-edge case where there is "sweeping" of flow about the tip leading to induction of fluid from top surface to bottom surface and subsequent formation of a secondary vortex, the case of the more "blunt" leading-edge vortex interaction produces a secondary vortex without the sweeping of the flow about the tip regions. The impinging primary vortex induces a strong instantaneous adverse pressure gradient along the lower surface of the edge; this leads to separation of the wall viscous layer and subsequent formation of a secondary vortex of opposite sense.

The actual distortion process of the incident vortex, on the other hand, is similar for the two cases for certain edge thickness scales. In the thin leading-edge case, one can clearly see the "splitting" of the primary vortex to upper and lower portions of

the edge surface. For the 5:1 elliptical leading-edge, if the edge scale thickness is sufficiently small compared to the incident vortex scale (i.e. $2T/\sigma\omega \leq 1.4$), then a similar severing of the incident primary vortex occurs. However, if the edge scale thickness becomes large with respect to the scale of incoming vorticity field, then the major portion of the incident vortex passes below the leading-edge surface. The thicker edge also produces a stronger vortex "image effect" upstream of the tip in such a way that the incident vortex begins to dive early as it approaches the tip of the leading-edge; this effect was not noticeable for the thinner leading-edges. Hence the edge thickness scale strongly affects the trajectory and distortion of the incident primary vortex during and after the impingement process. The generation of the secondary vortex, on the other hand, does not seem to be significantly affected by the various thicknesses of the leading-edges. The scale and the roll-up process of the secondary vortex remains relatively constant for all the edge thickness scales examined.

In contrast, the transverse offset of the edge with respect to the center of the incident vortex has a strong effect on the generation of the secondary vortex. For the zero offset case ($\xi/2T=0$), almost all of the incident vortex dives below the surface and produces a strong secondary vortex along the lower surface of the edge. For the positive offset case ($\xi/2T=0.1$), all of the incident vortex dives below the surface and the impingement point moves downstream

of the tip of the edge. The secondary vortex breaks down before the roll-up process is completed. In the case of $\xi/2T=-0.4$, all of the (marked) incident vortex passes above the plate relatively undistorted and moves away from the surface downstream of the edge: no apparent secondary vortex generation can be detected from the visualization. The pressure amplitude and phase data seem to reflect the physics of the flow discussed above. For both cases of $\xi/2T=0$ and $\xi/2T=0.1$, along the upper surface where no significant portions of the primary vortex pass by, the phase remains relatively constant.

The instantaneous pressure data also shows this lack of wave-like motion along the upper surface of the edge. Along the lower surface, however, there is a definite increase in the phase in downstream direction and the corresponding instantaneous pressure plot exhibits a travelling wave-like motion as a function of time. The rms pressure amplitude along the top and bottom edge surfaces for the two offset cases are of the same order but distributed differently; the peak amplitude occurs at $x/T=0.0$ for the zero offset case and at the $X/T=0.25$ for the positive offset case. The amplitude values downstream of the leading-edge is also greater for the positive offset case compared to the negative offset case. The case of negative offset ($\xi/2T=-0.4$) shows a similar characteristic as the two previous cases, but in reverse; the upper surface shows an ever-increasing phase and corresponding wave-like motion of the instantaneous pressure as a function of time, whereas the lower surface shows a constant phase and pressure

amplitude. Hence, one can conclude that the unsteady pressure fields exhibit wave-like motion in agreement with the convection of the vortex instability and lack of such connection leads to nearly constant streamwise phase of the pressure field which provides large local loading there.

Proposed Investigation

In the previous investigation a single row of concentrated vortices interacting with the leading-edge was examined. In many practical situations, however, the impingement process involves more than one row of vortices. For the case of two rows of vortices of opposite sense, it would be interesting to see how the impingement process of one row affects the other row, or how the simultaneous impingement of the two rows of vortices alters the interaction process. This can be done by using a thin plate upstream of the leading-edge to generate a von Karman vortex street. This set-up will produce two rows of vortices of opposite sense for the impingement process. The various edge offsets would probably have a drastic effect on the distortion or subsequent agglomeration of the two rows of vortices following the impingement upon the edge. Both the visualization and pressure and phase measurements can be carried out to understand the details of the interaction mechanisms. The shedding frequency of the von Karman vortex street can be changed by increasing or decreasing the flow speed as well as by changing the thickness of the plate from which shedding occurs. Using this method, one would be able to see the effect of different Reynolds numbers and frequencies of vortex streets on the interaction process. It would also be interesting to observe the effect of all these parametric variations on the subharmonic and harmonic components of the pressure field. Proper filtering, in conjunction with cross spectral analysis, can allow characterization of the pressure amplitude and phase of the subharmonic and harmonic components.

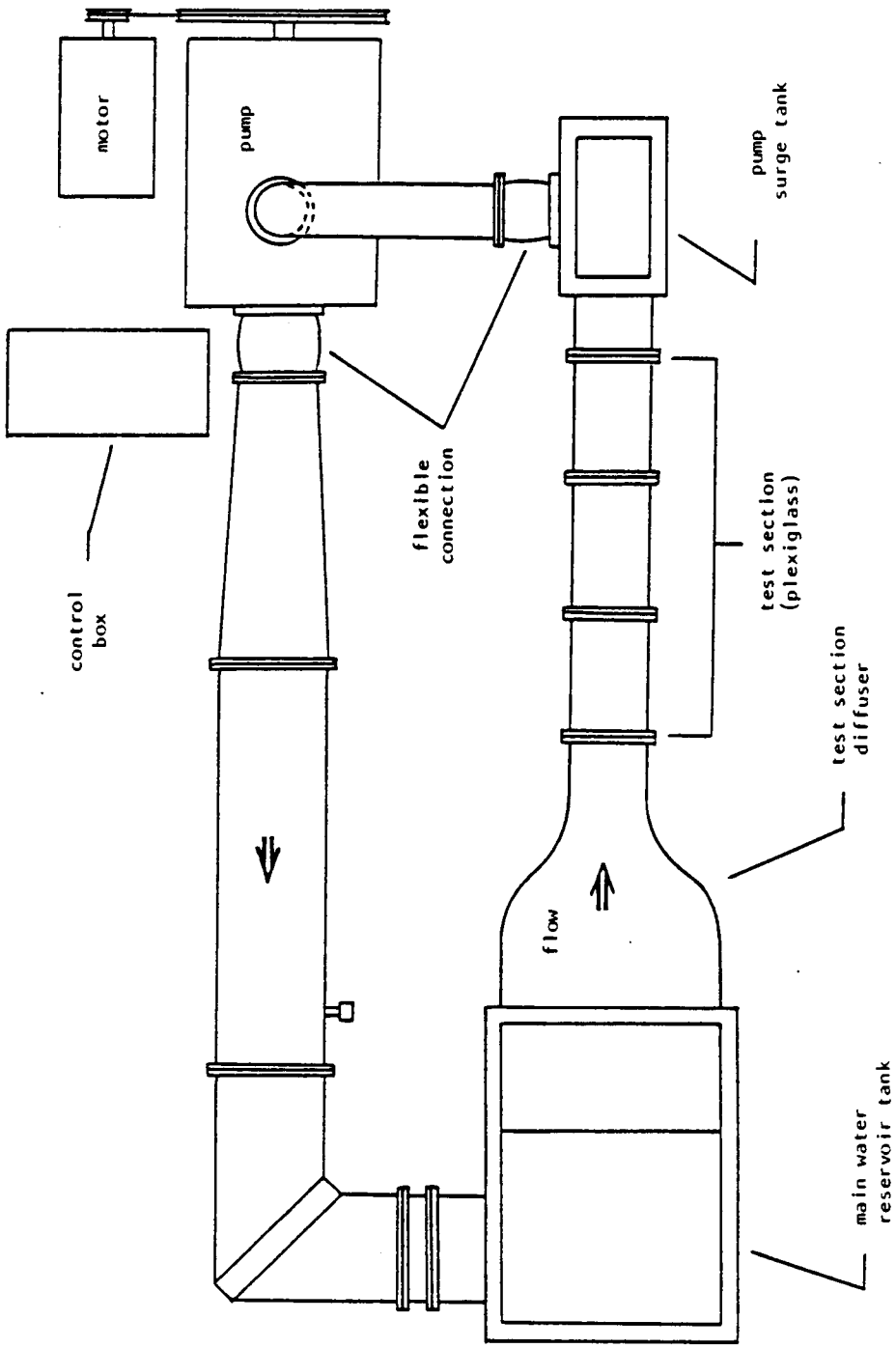

Figure 1. Top view of the closed loop water channel.

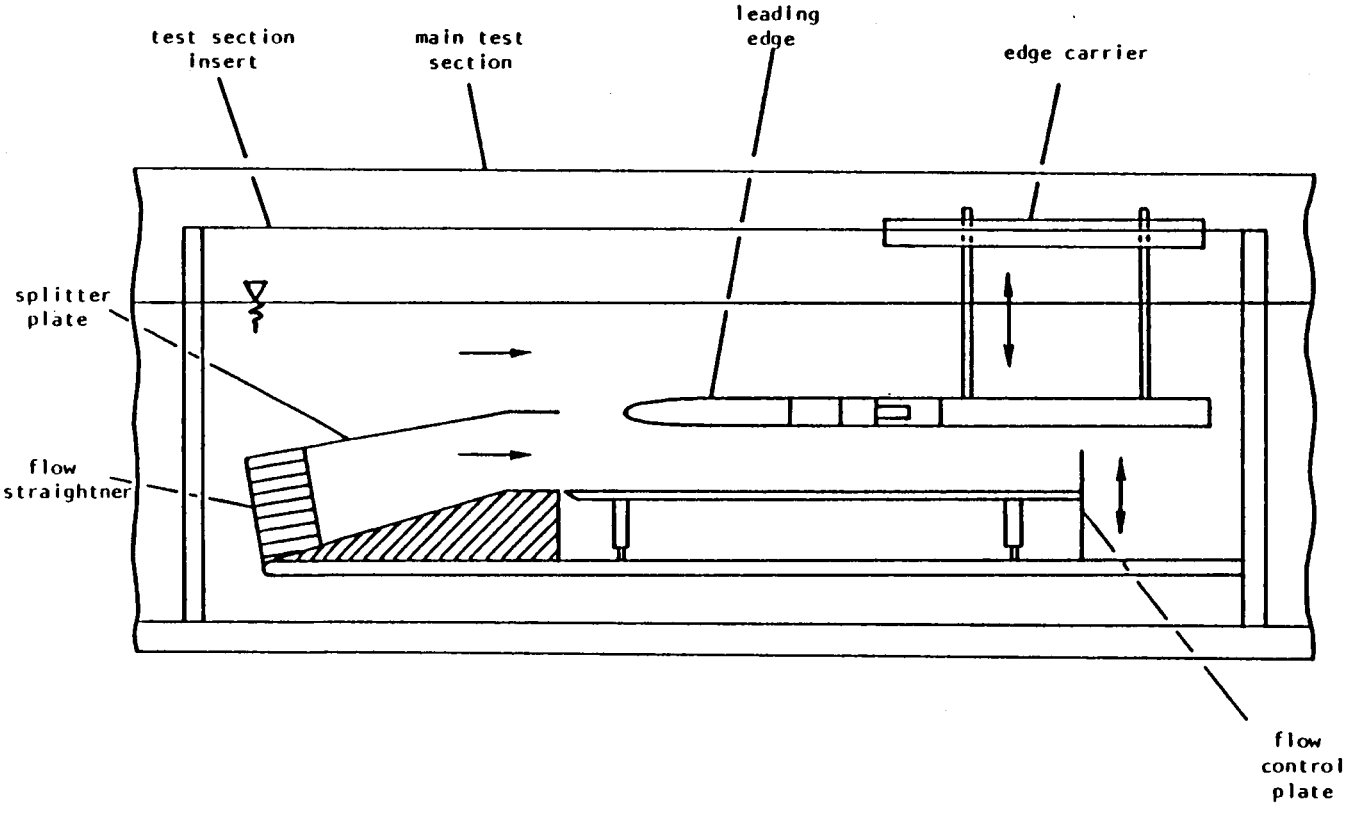

Figure 2. Side view of the test section for 5:1 elliptical leading edge set-up.

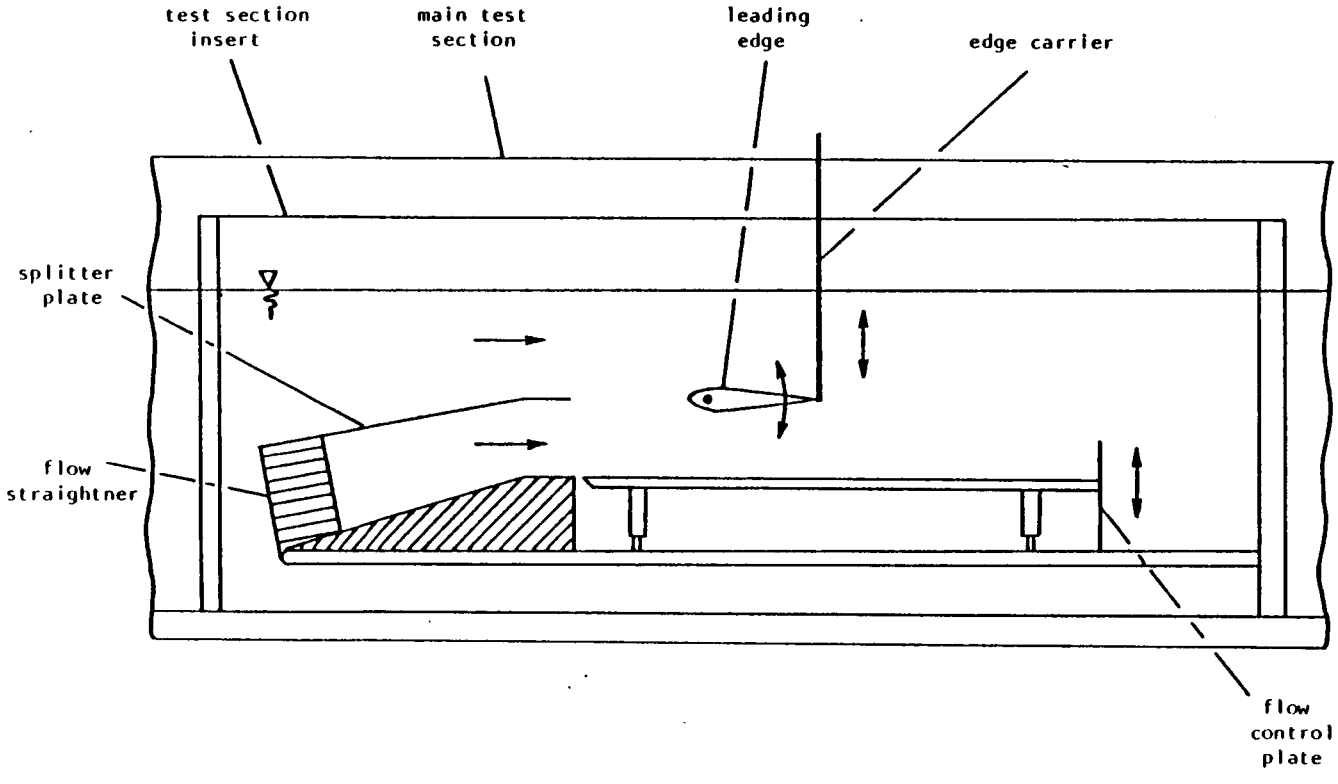

Figure 3. Side view of the test section for airfoil set-up.

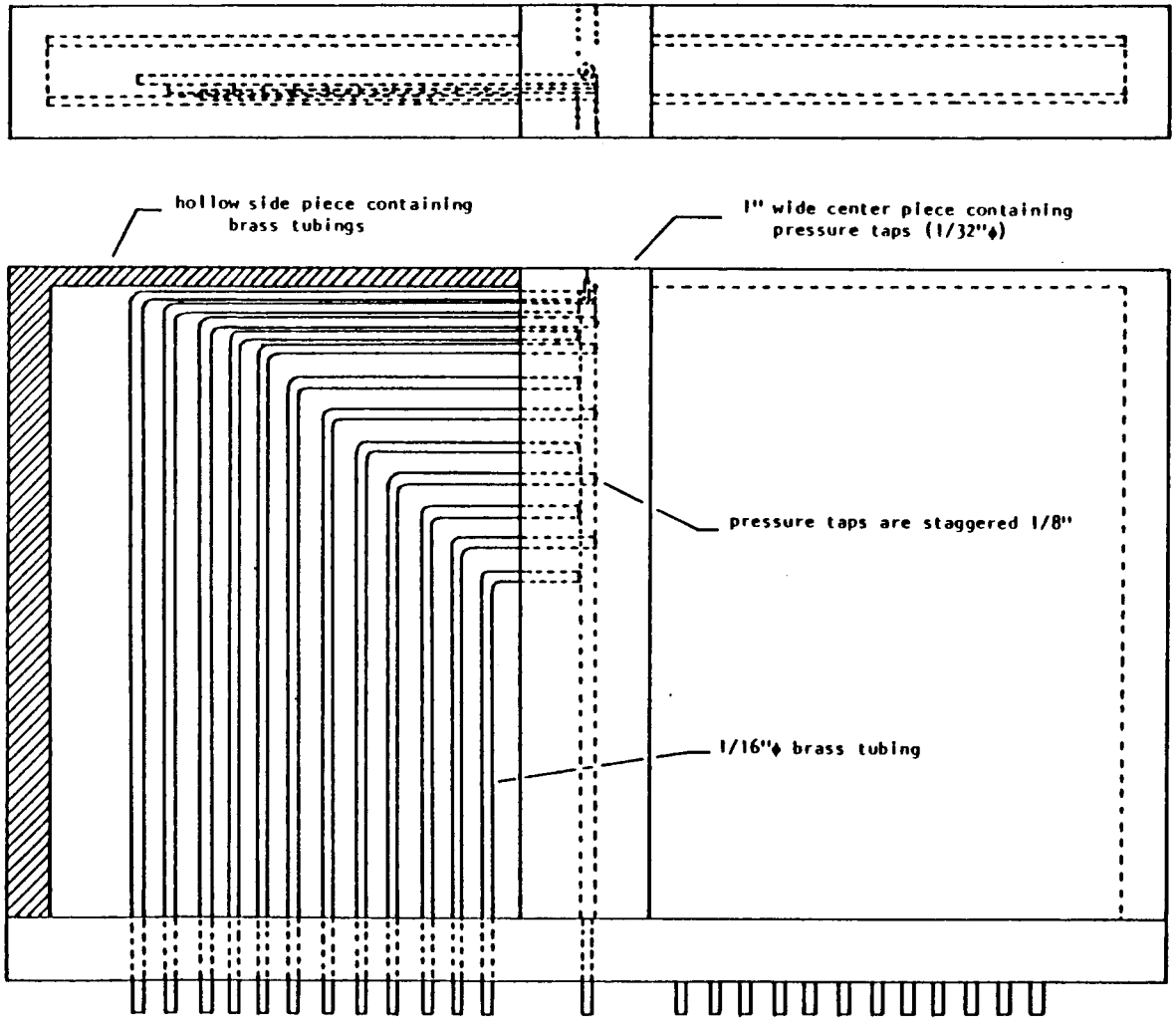

Figure 4. Brass tubing layout for 5:1 elliptical leading edge. (Scale 1.42:1)

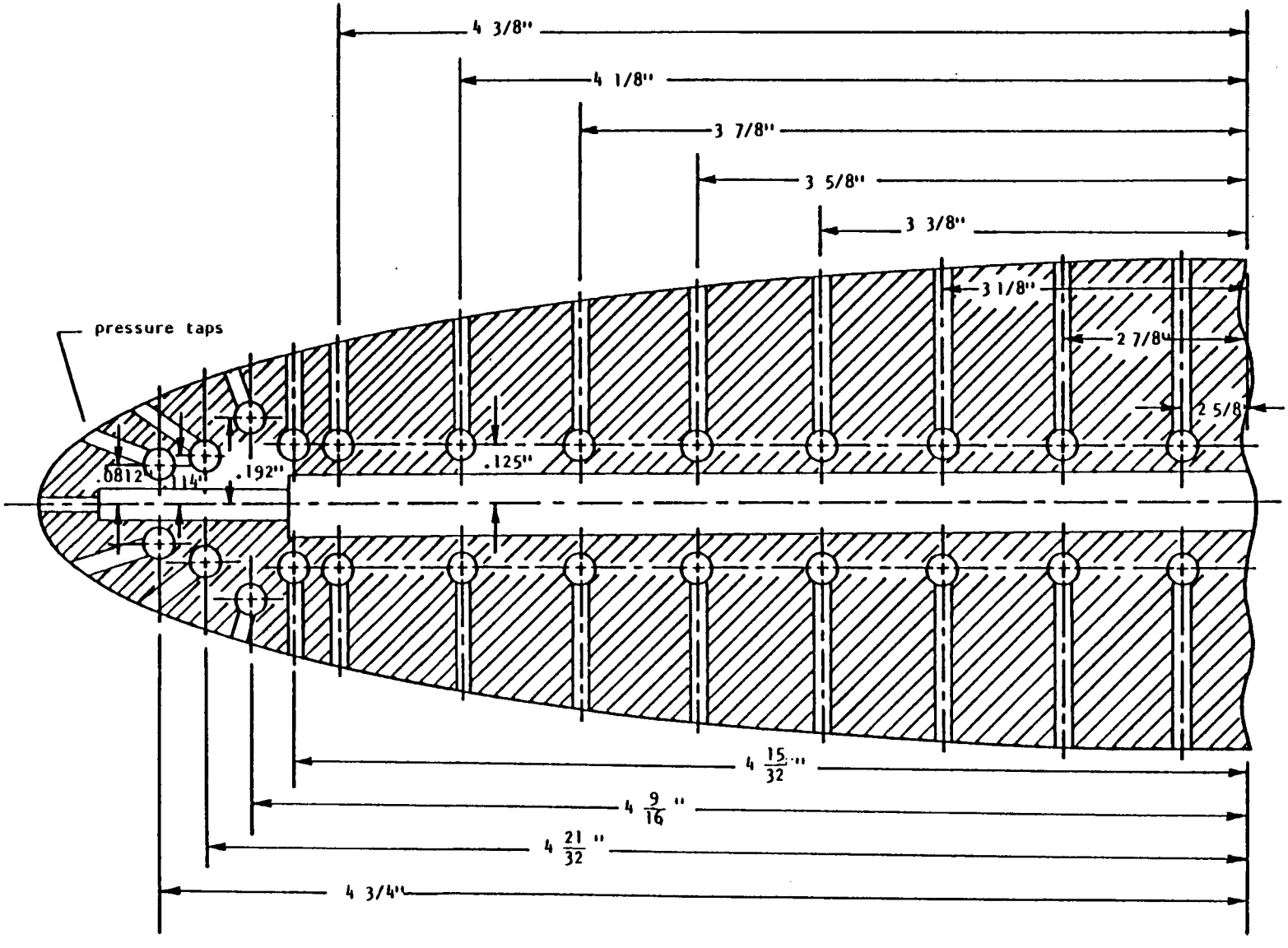

Figure 5. Details of tap and brass tubing locations on the elliptical leading edge. (Scale 1:3)

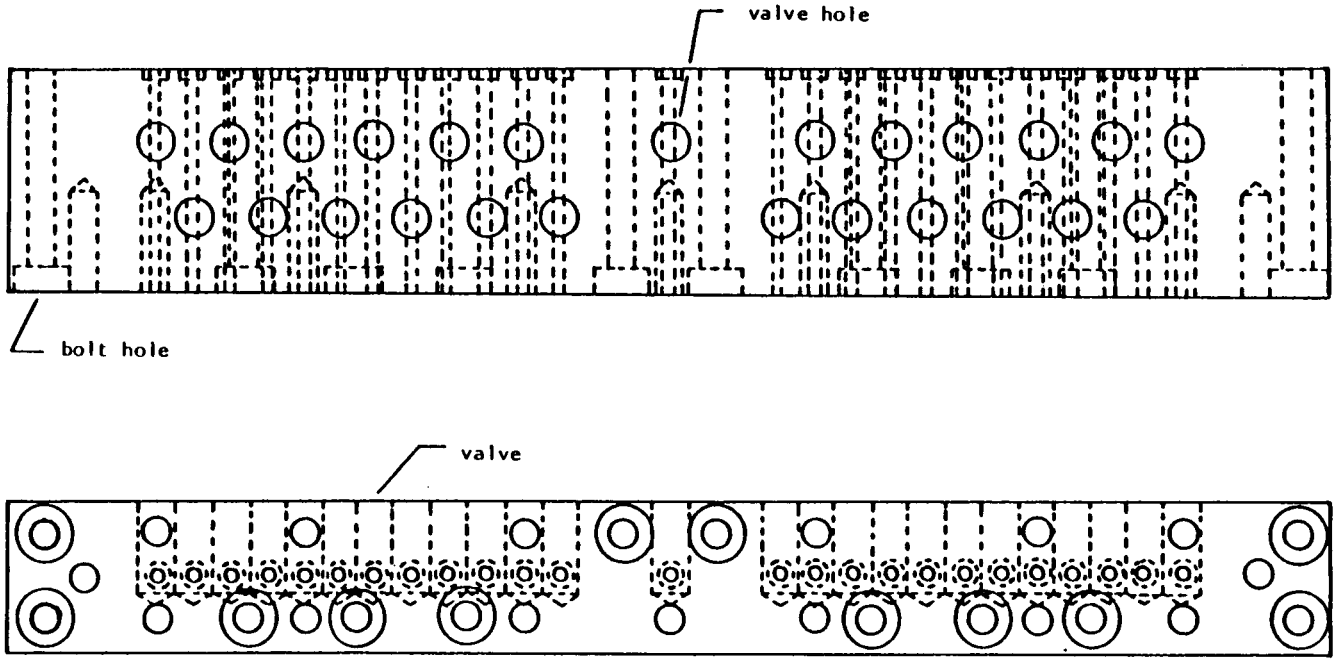

Figure 6. Valve body section containing 25 valves for the individual pressure taps. (Scale 1.25:1)

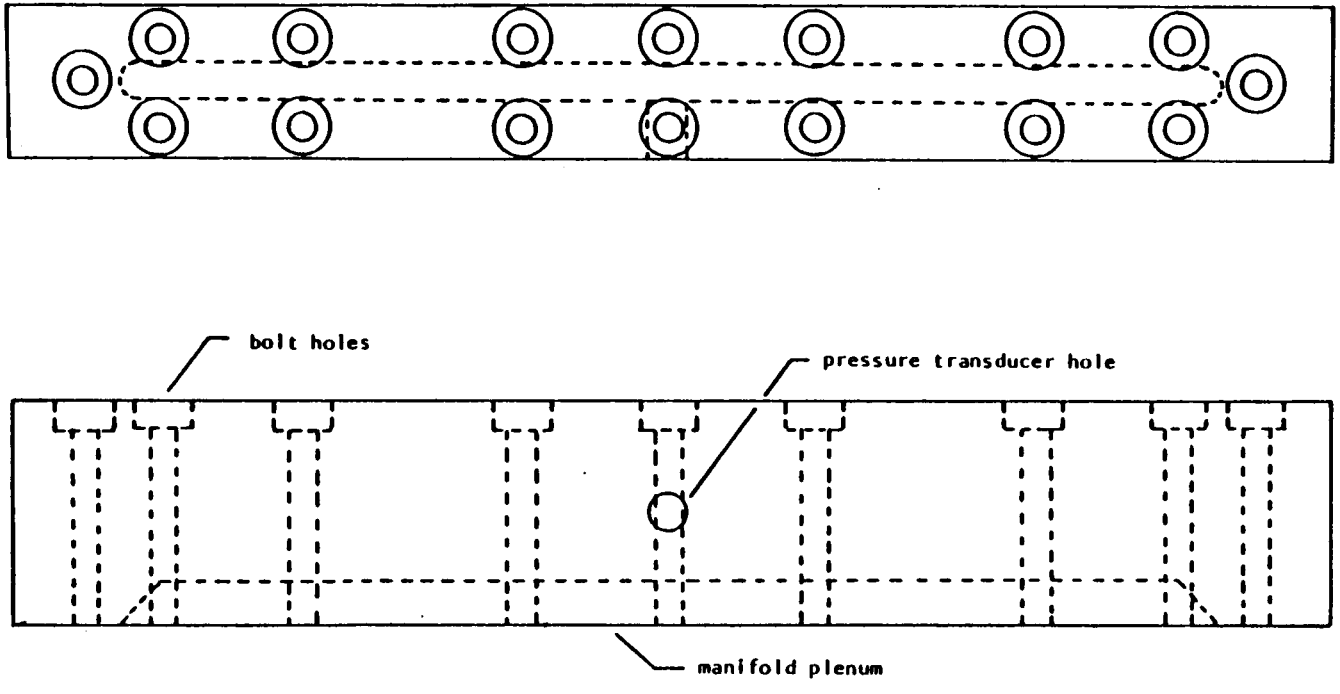

Figure 7. Manifold plenum containing the pressure transducer. (Scale 1.25:1)

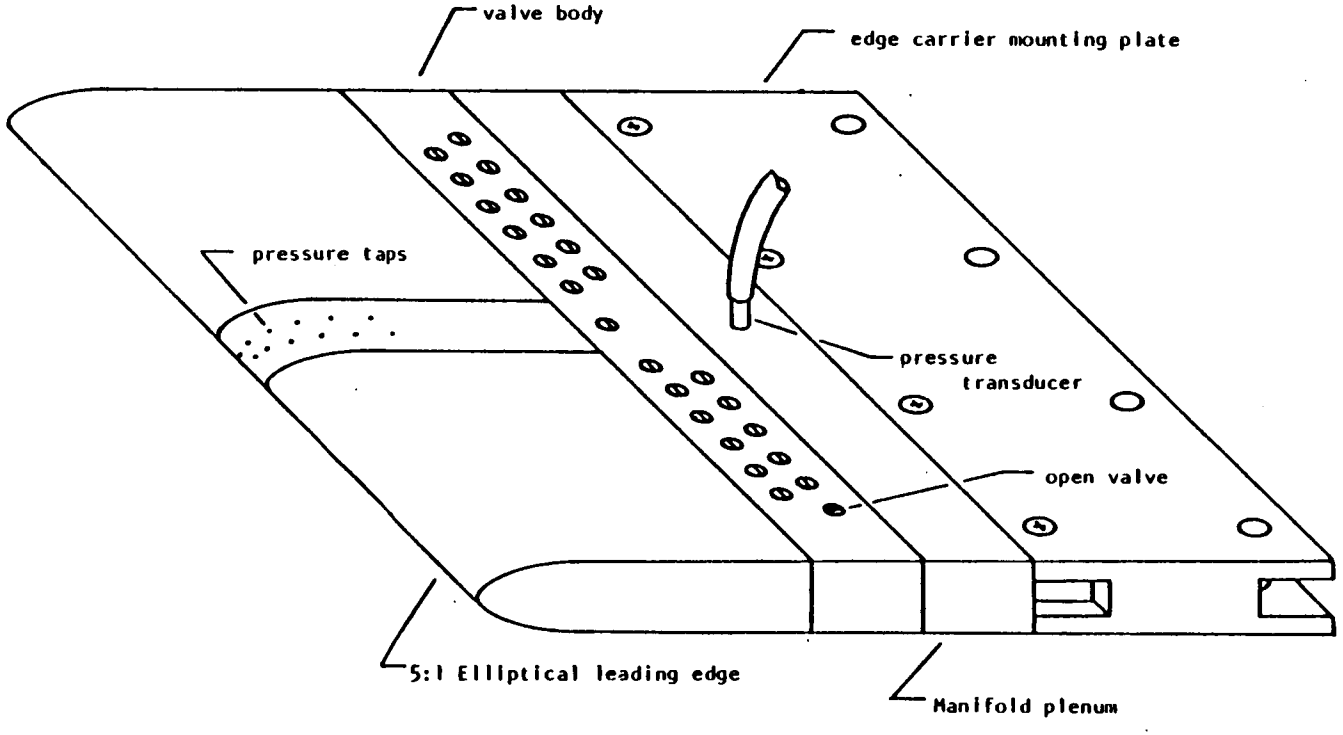

Figure 8. Overall view of all the pieces clued and bolted together and ready to mount on the edge carrier. (Scale 2.5:1)

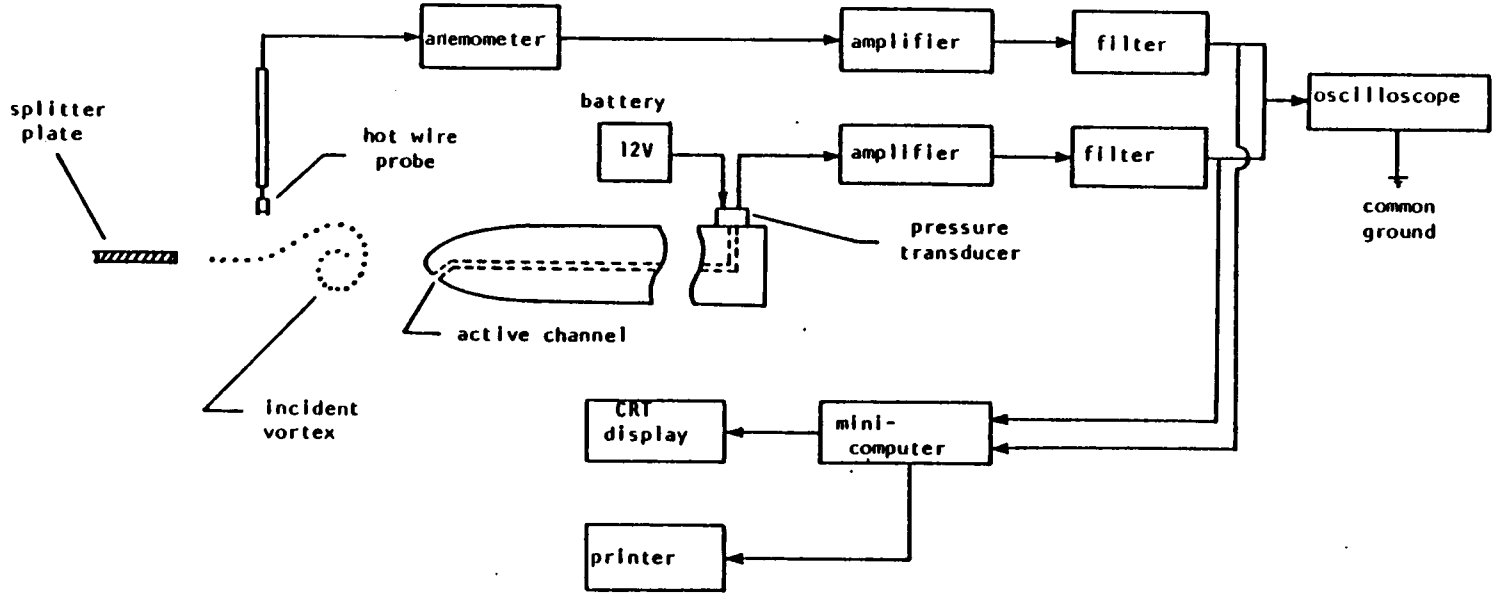

Figure 9. Electrical schematic for the cross spectra data taking (velocity signal: reference, pressure signal: active).

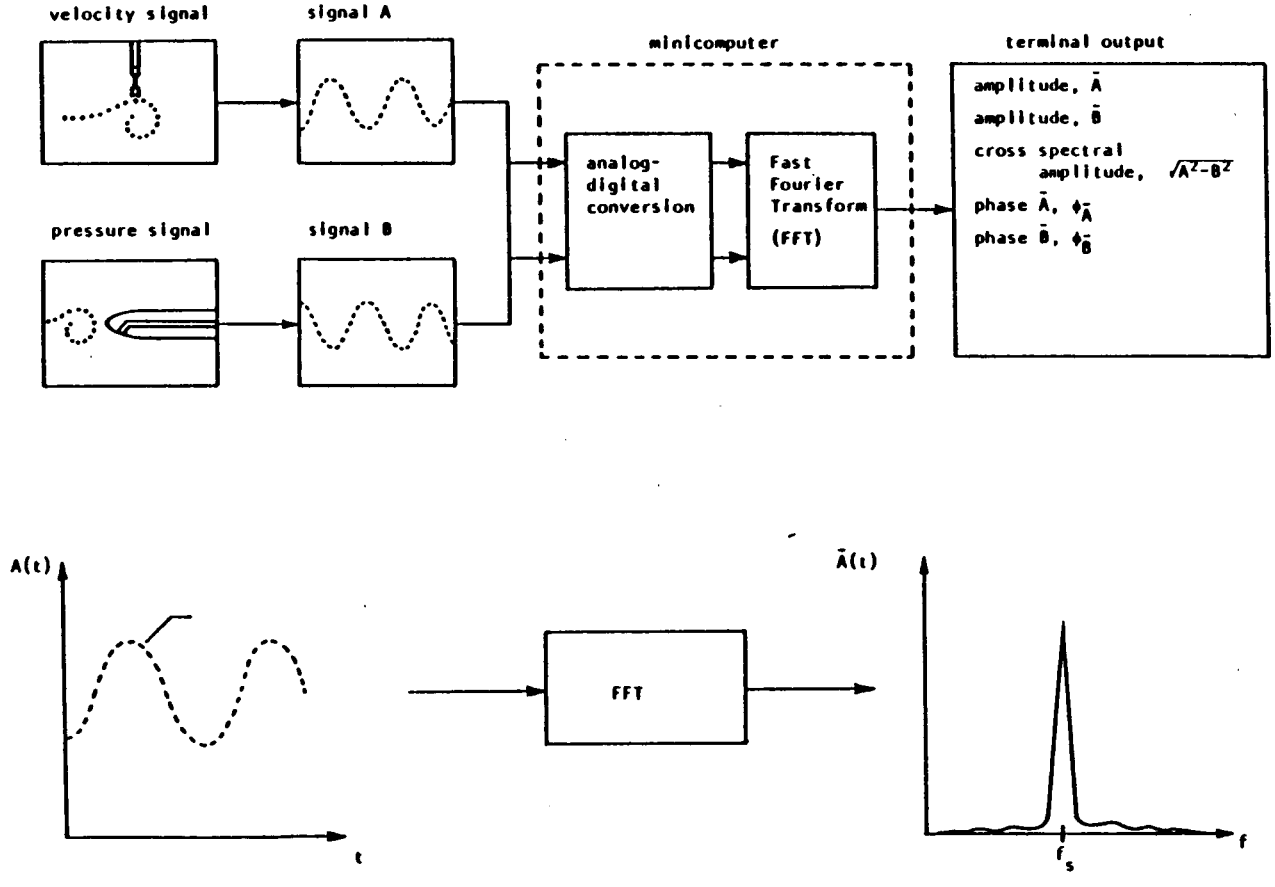

Figure 10. Schematic for digital data acquisition and cross spectral analysis.

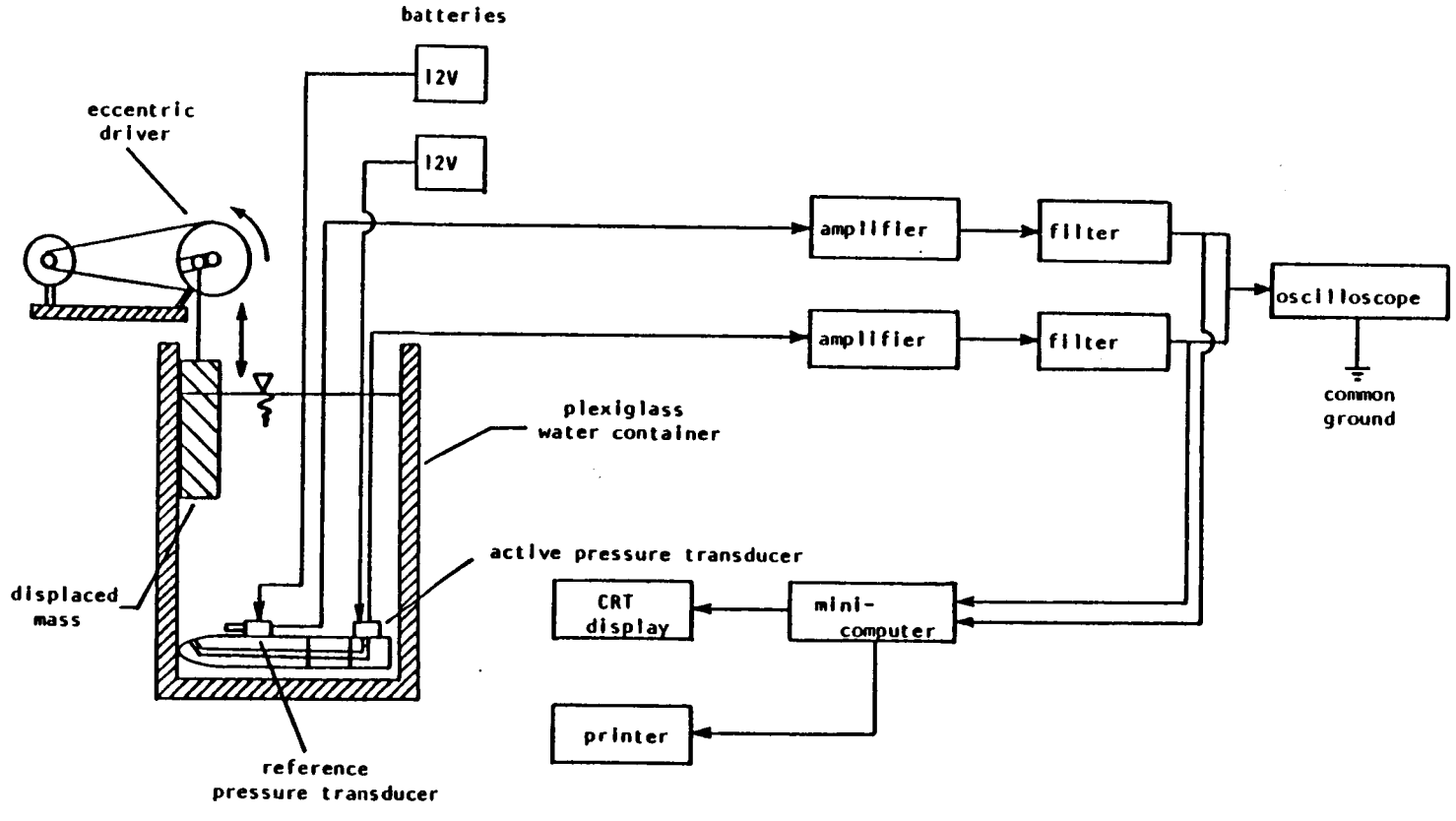

Figure 11. Electrical and mechanical schematic for pressure transducer/tap system calibration.

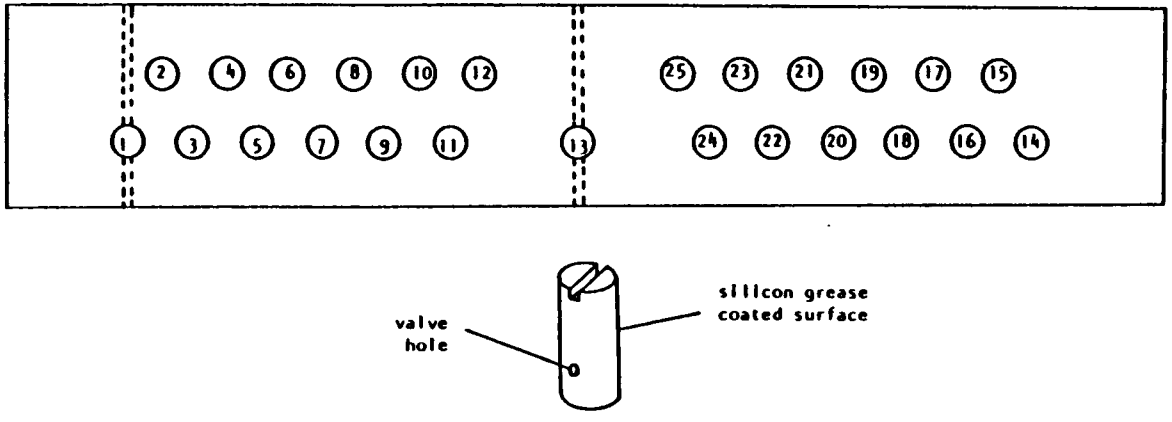

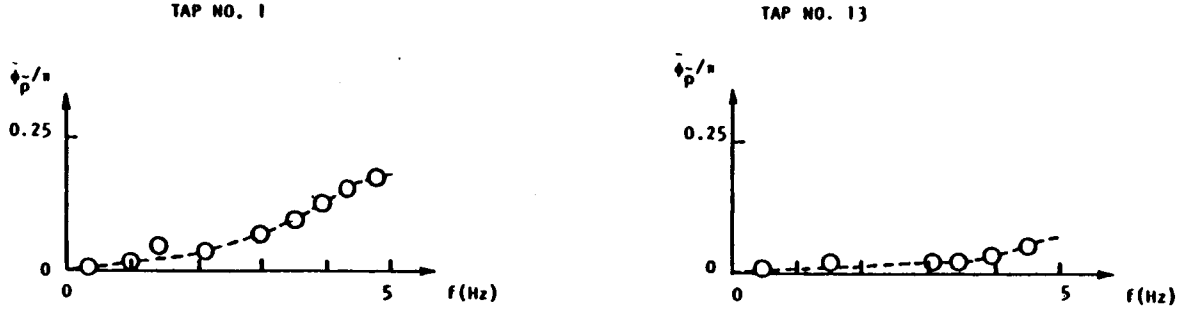

Figure 12. Valve numbering notation and calibration result (phase of fluctuating pressure vs. frequency)

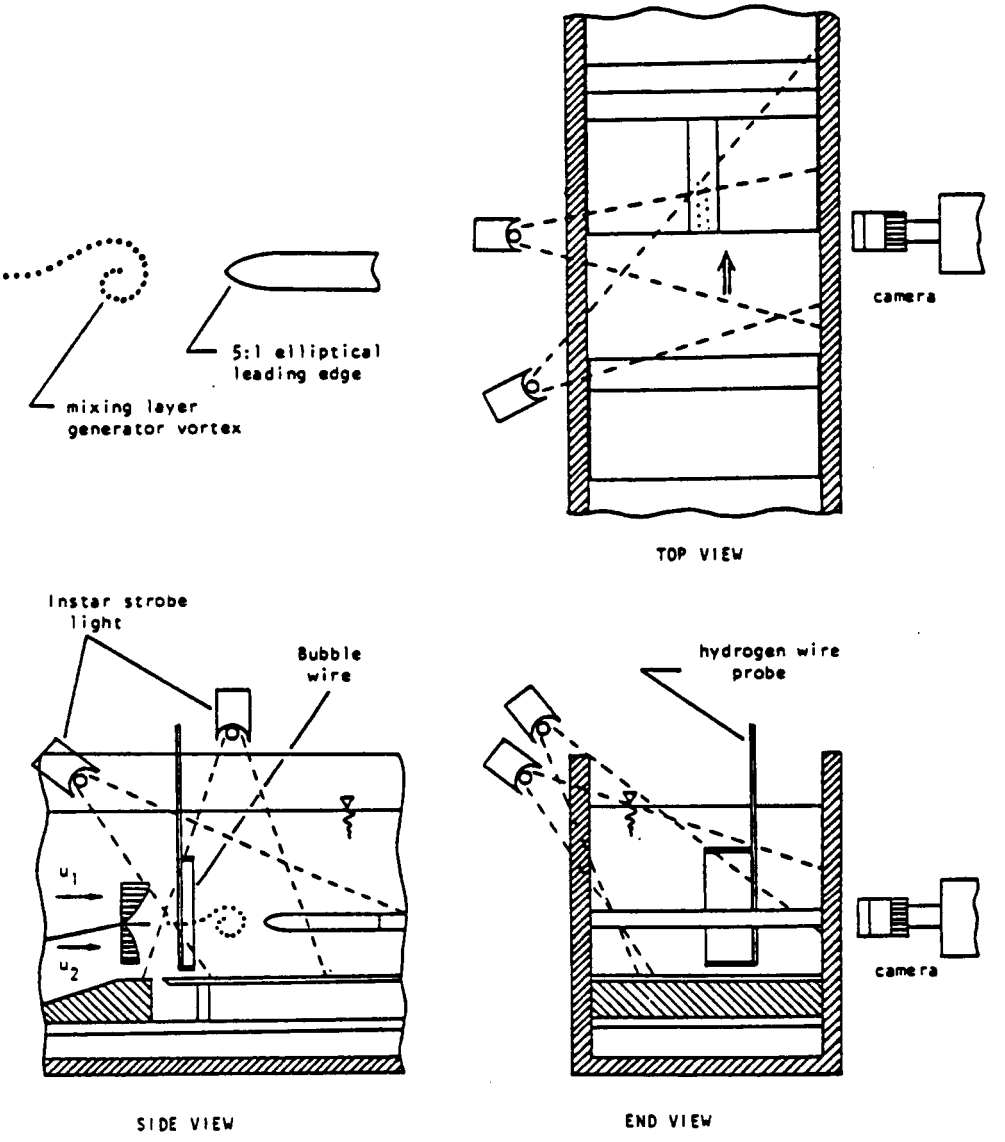

Figure 13. Overview of hydrogen bubble time-line visualization set-up.

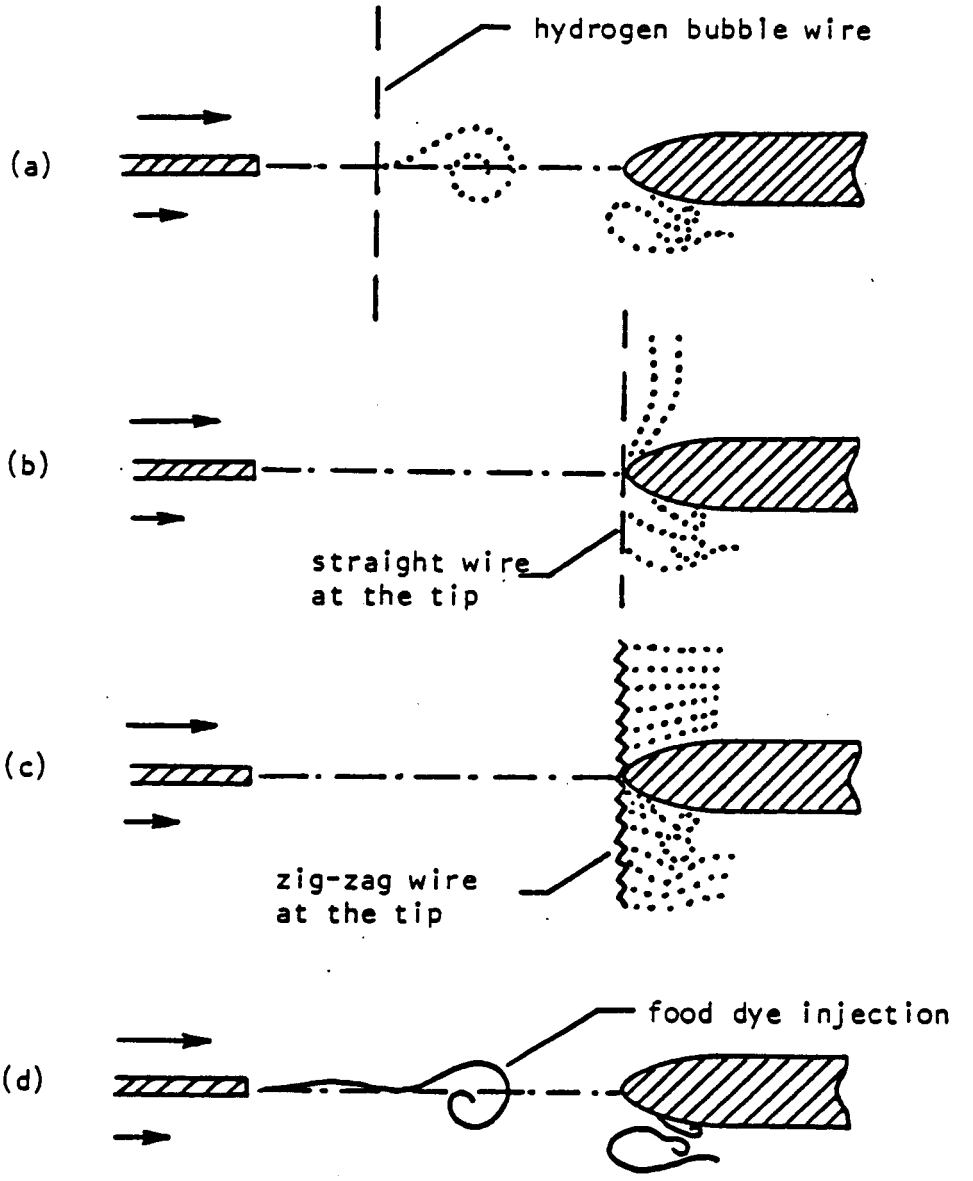

Figure 14. Various hydrogen bubble line visualization technique.

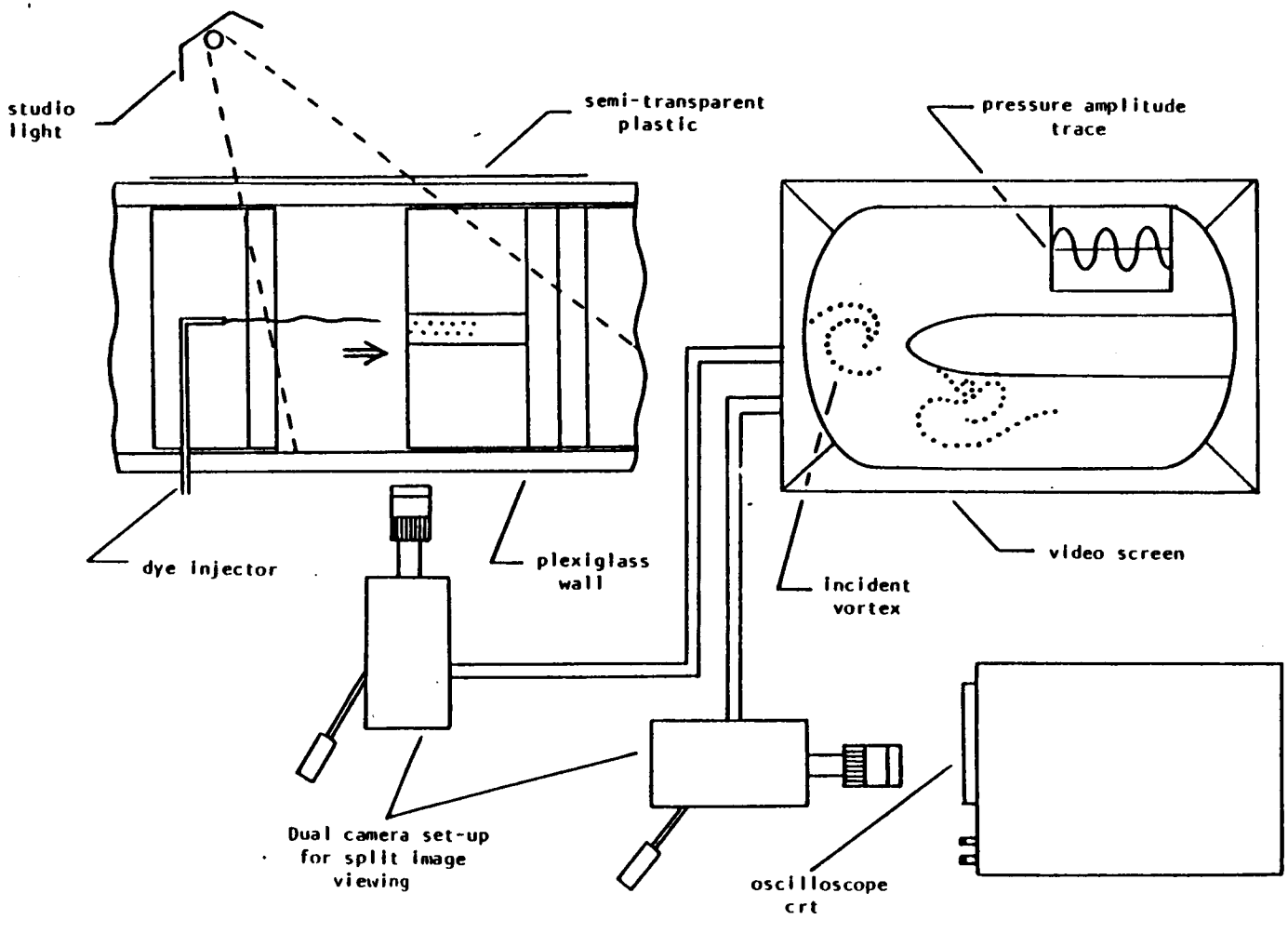

Figure 15. Overview of simultaneous pressure/dye injection visualization technique for correlating visualized data to instantaneous pressure.

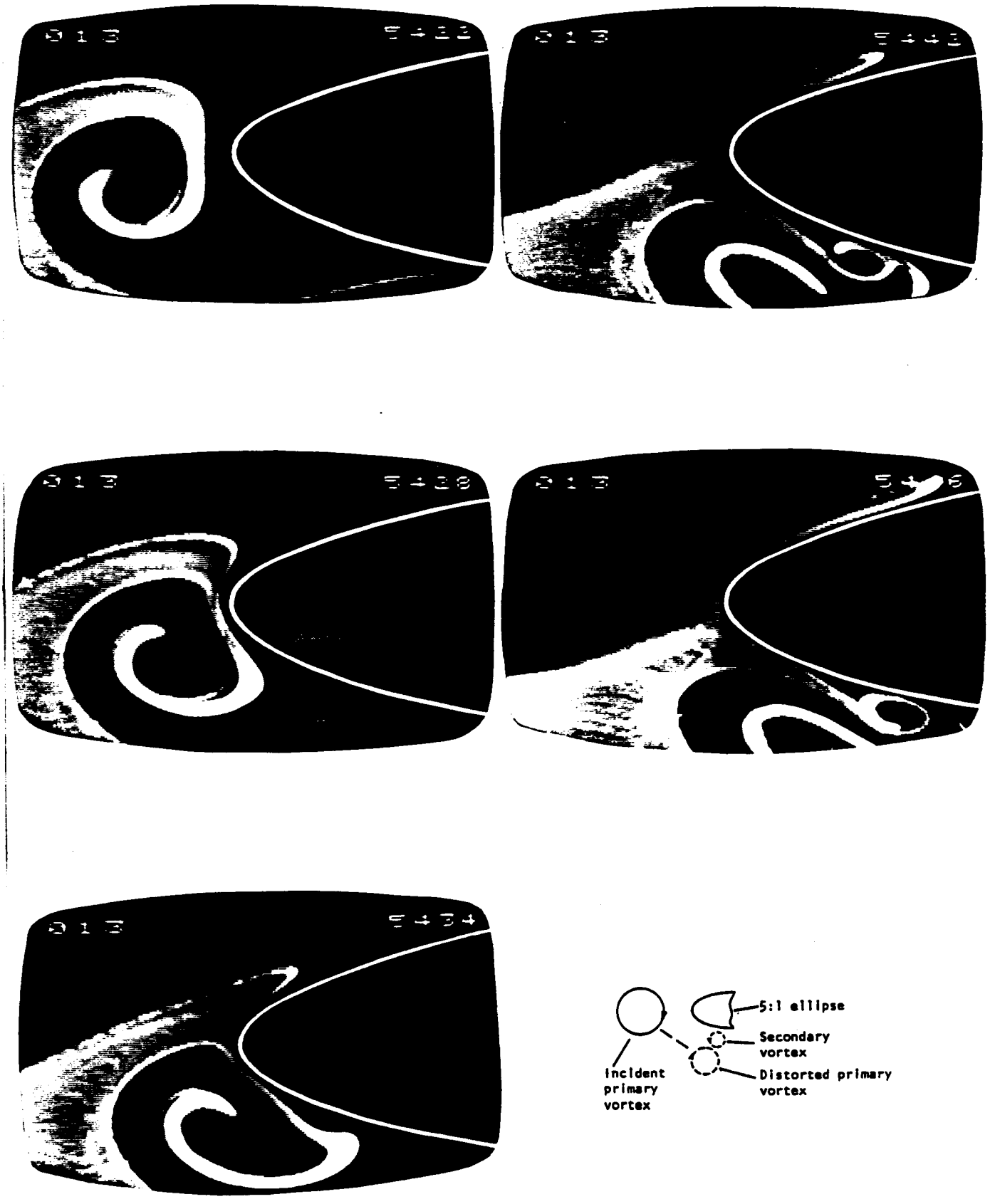

Figure 16. Vortex incident upon a 5:1 elliptical leading-edge. ($\xi/2T = 0$)

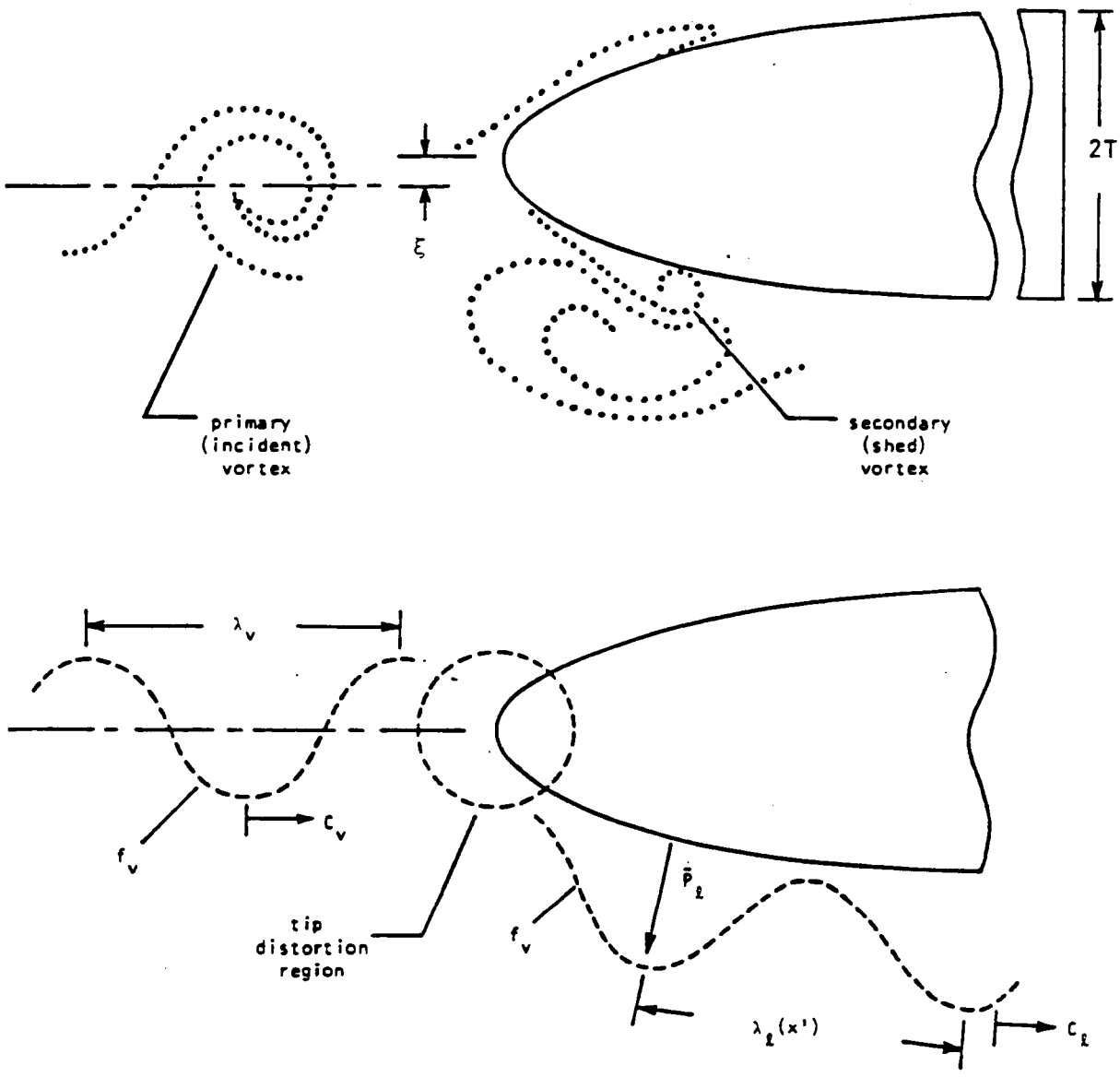

Figure 17. Details of primary vortex-leading edge interaction and subsequent secondary vortex shedding.

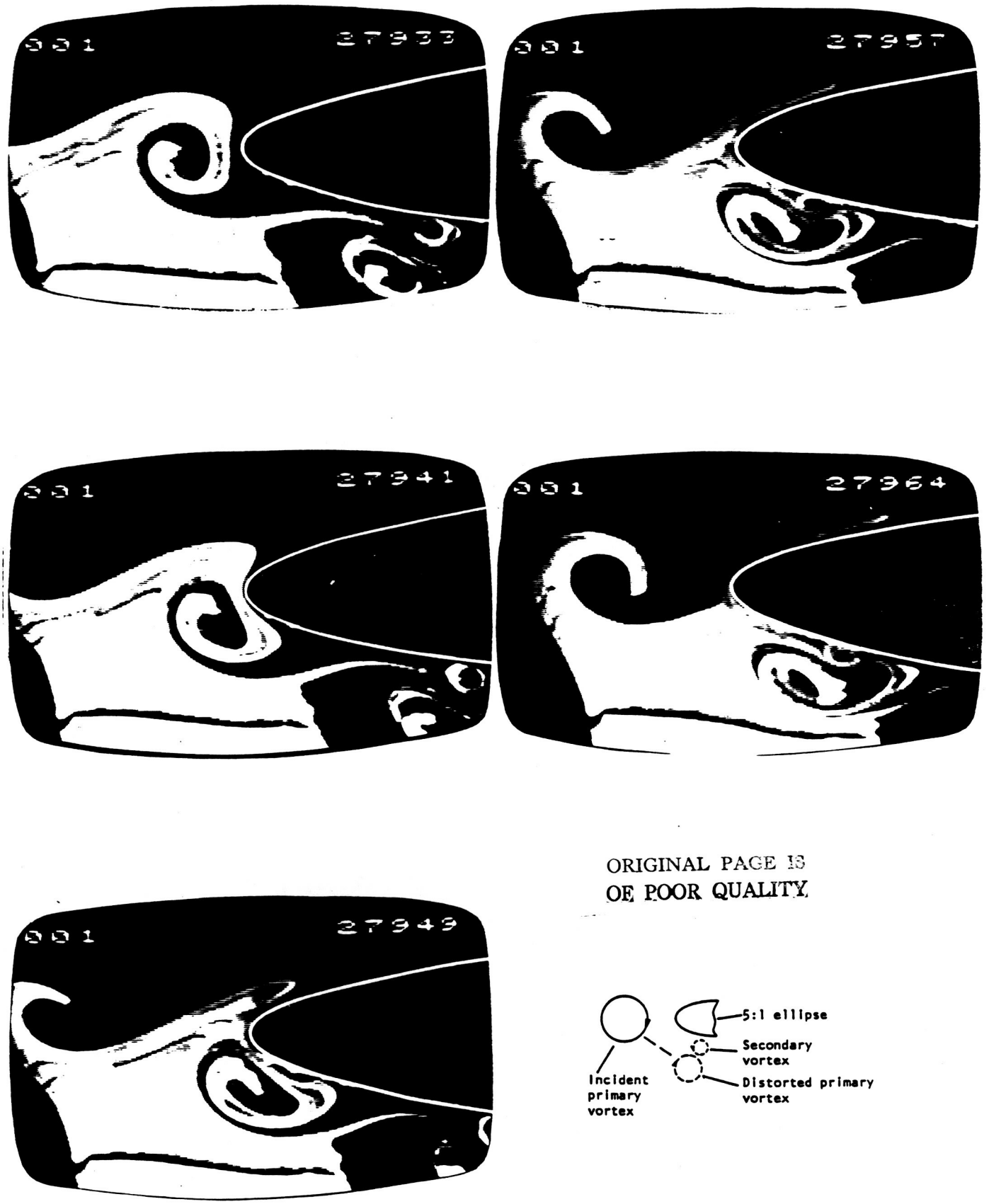

ORIGINAL PAGE IS
OF POOR QUALITY

Figure 18. Wider view of vortex-leading edge interaction (5.1 elliptical leading edge). ($\xi/2T = 0$)

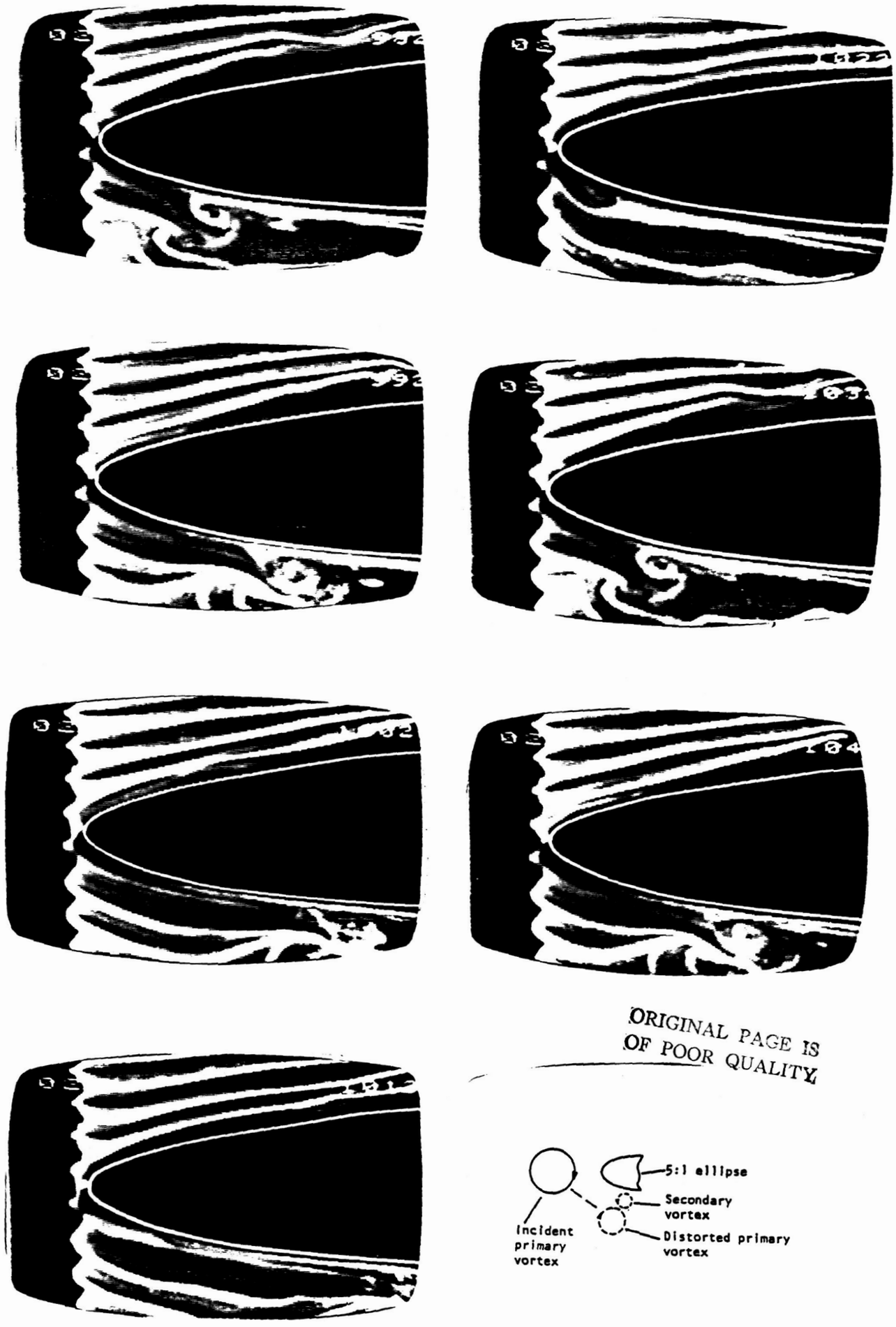

Figure 19. Notched hydrogen bubble wire is used for the visualization of same set-up as in Figures 16 and 18. ($\xi/2T = 0$)

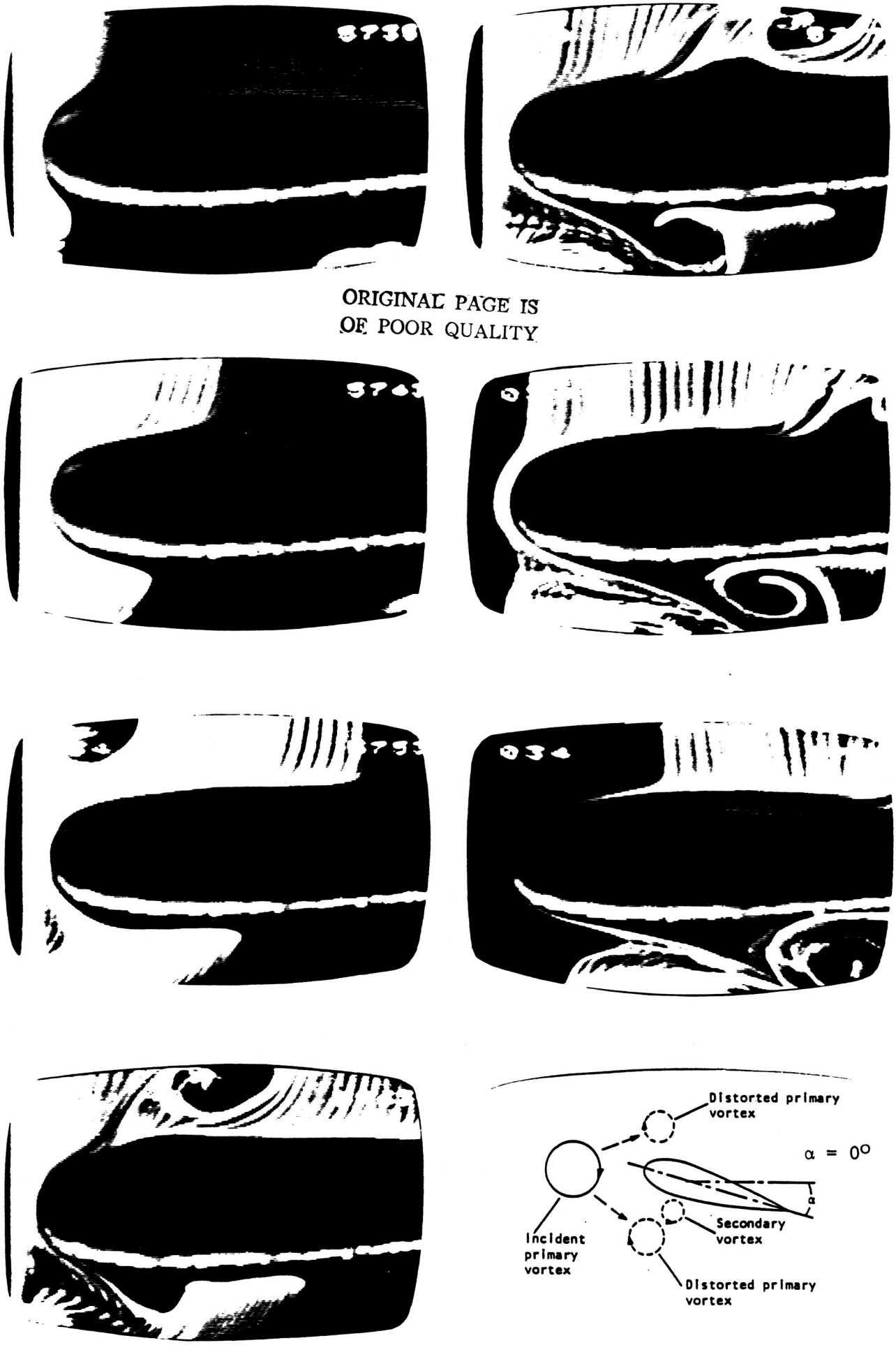

ORIGINAL PAGE IS
OF POOR QUALITY

Figure 20. Vortex incident upon a NACA 0012 airfoil (0° angle of attack). ($\xi/2T = 0$)

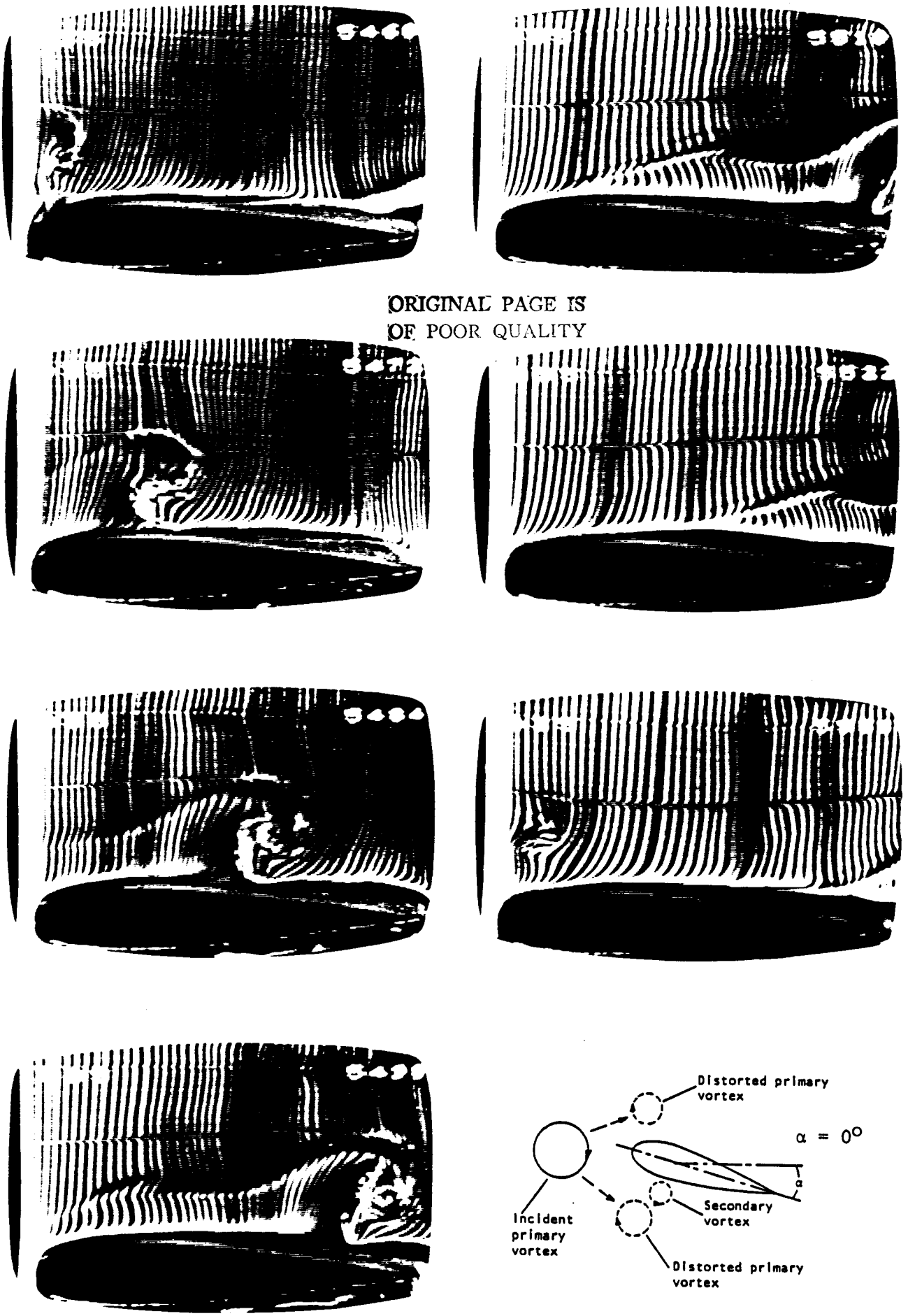

Figure 21. Fine time-line visualization of distorted primary vortex on the upper surface of the airfoil (0^{o} angle of attack). ($\xi/2T = 0$)

Figure 22. Vortex incident upon an airfoil with -10° angle of attack. $(\xi/2T = 0)$

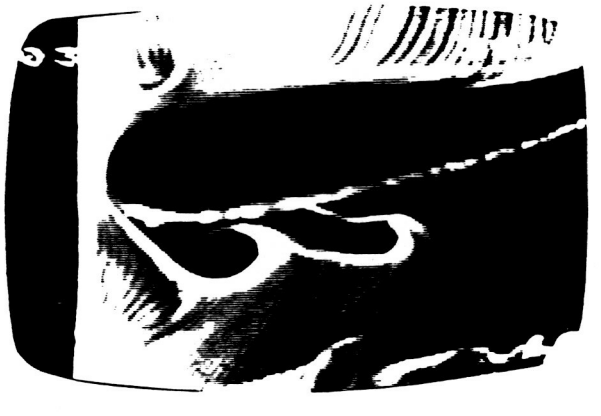

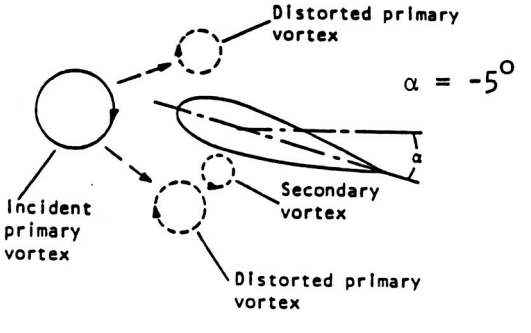

Figure 25. Vortex incident upon an airfoil with -5° angle of attack. ($\xi/2T = 0$)

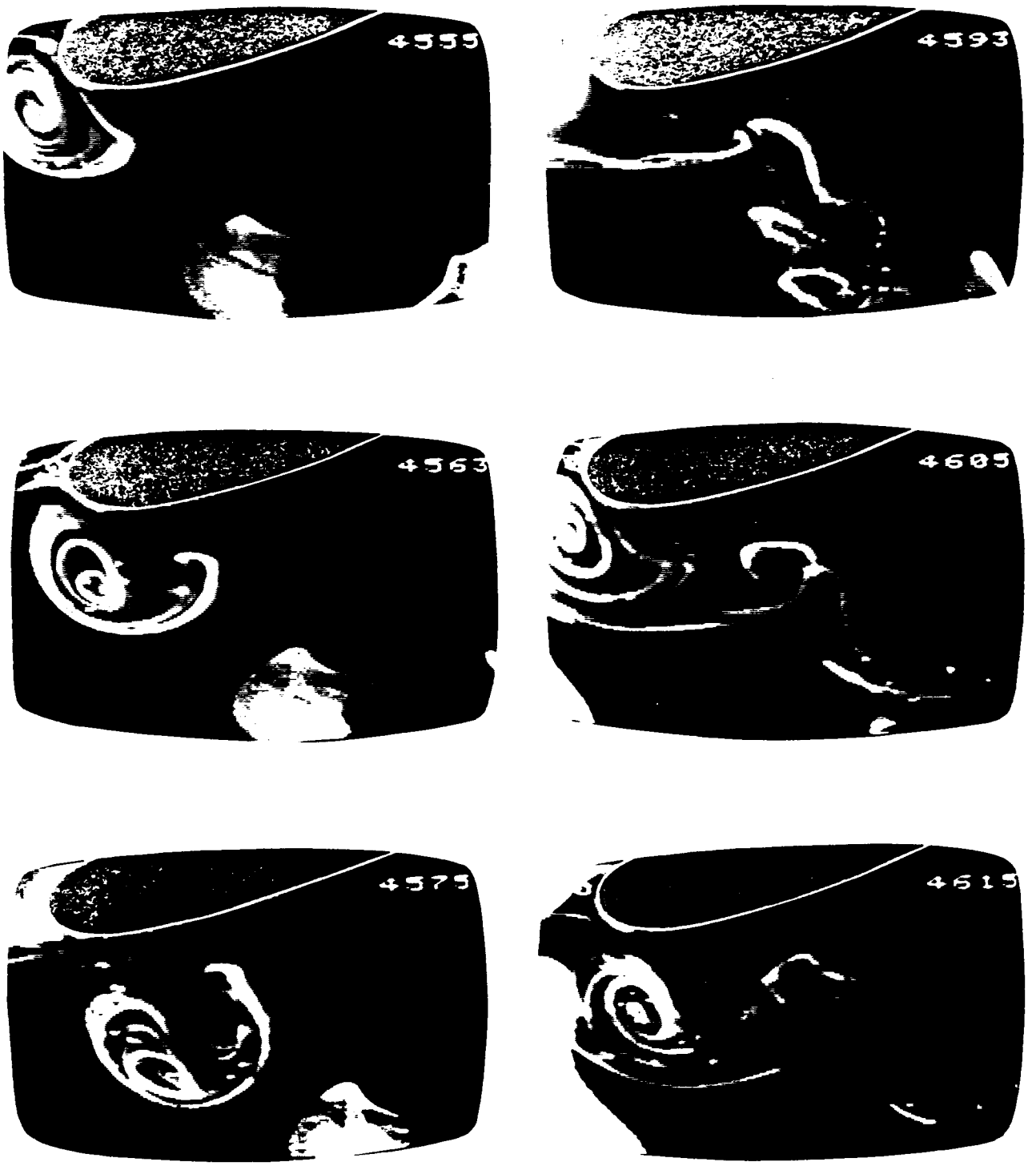

Figure 24. Wider view of vortex incident upon an airfoil with -10° angle of attack. ($\xi/2T = 0$)

ORIGINAL PAGE IS
OF POOR QUALITY

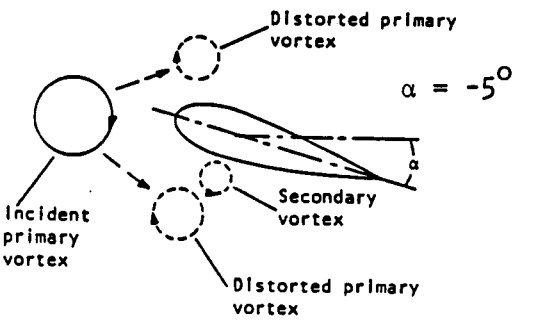

Figure 25. Vortex incident upon an airfoil with -5° angle of attack. ($\xi/2T = 0$)

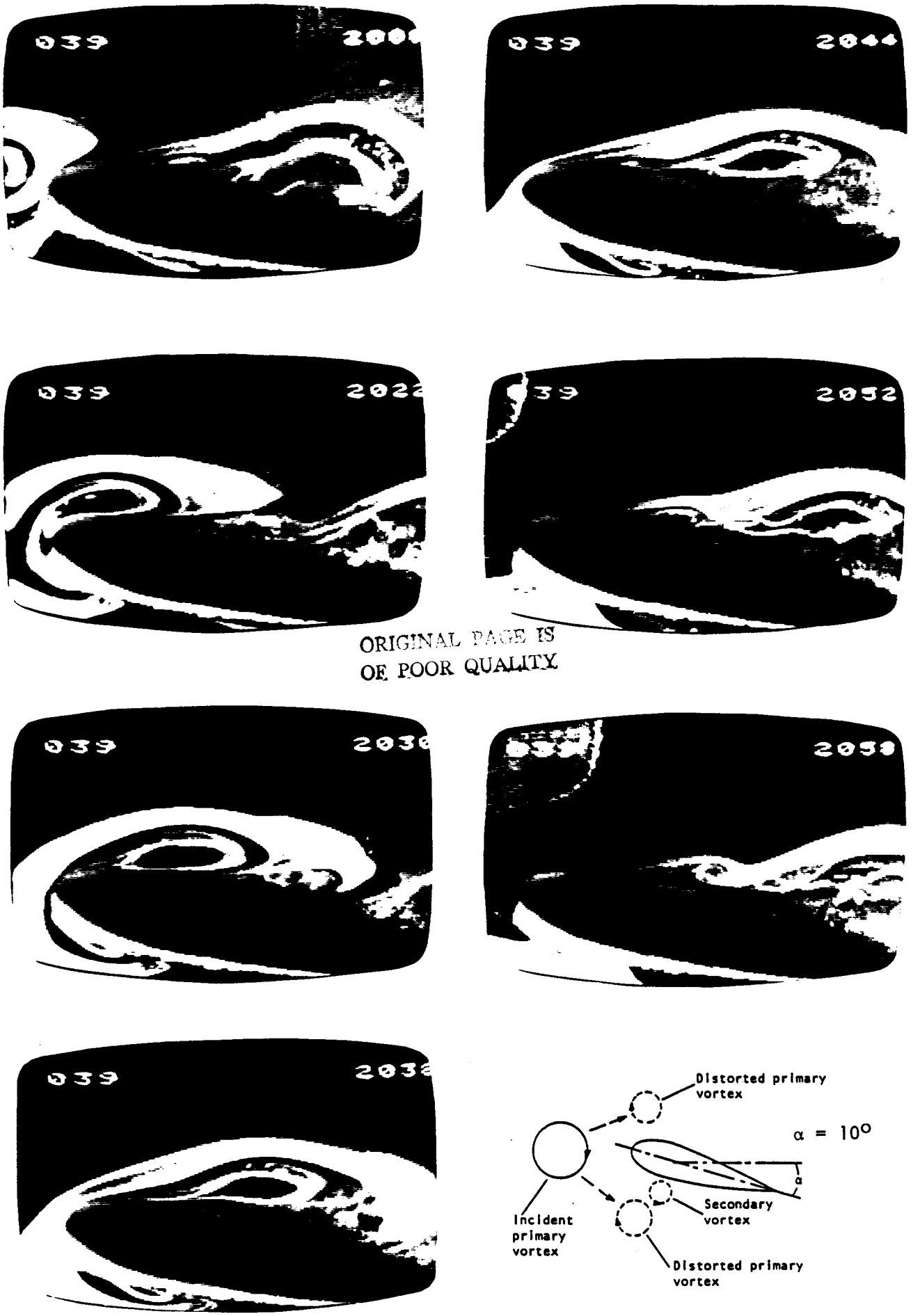

Figure 26. Vortex incident upon an airfoil with 10^{o} angle of attack. ($\xi/2T = 0$)

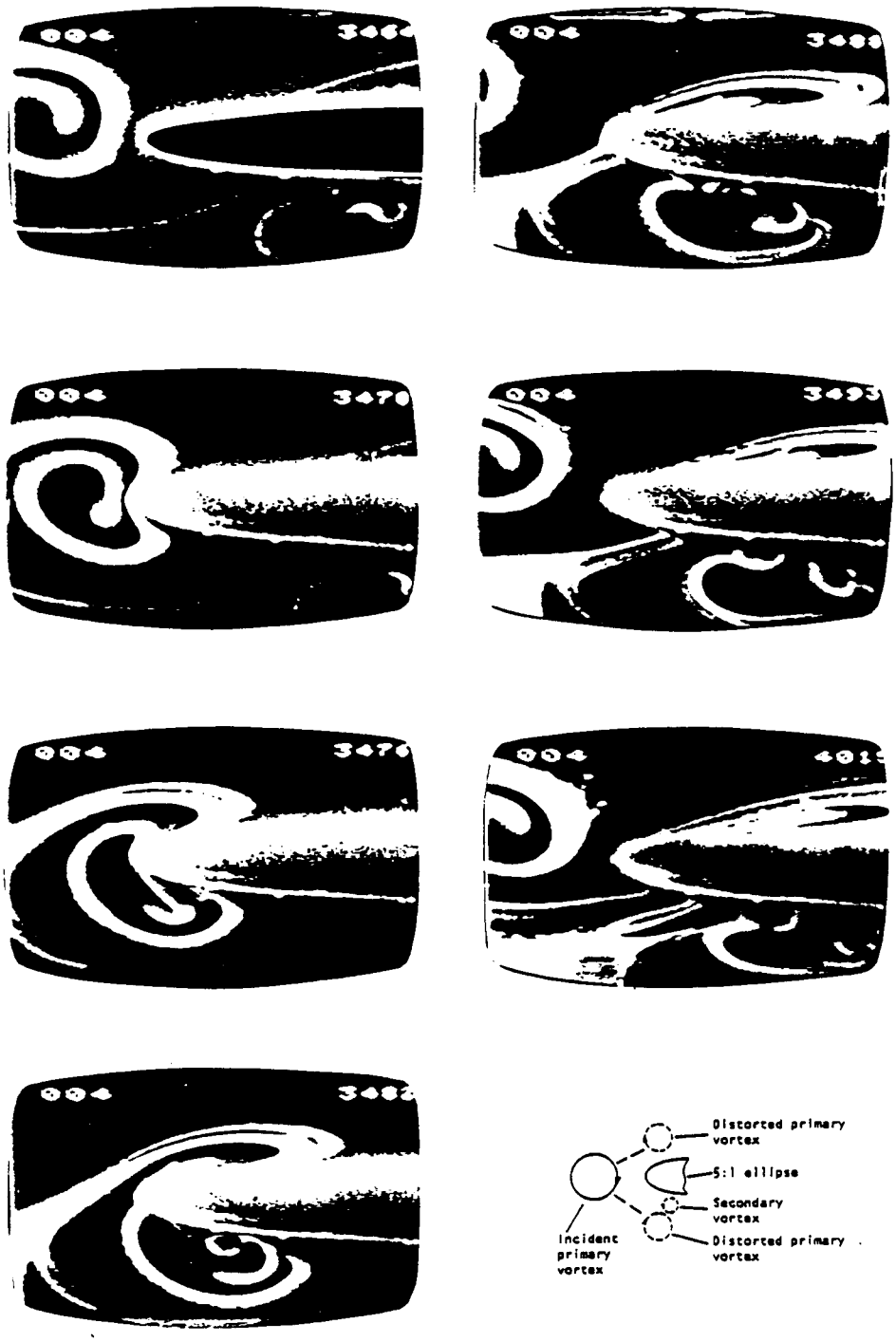

Figure 27. Effect of edge thickness on the interaction; vortex incident upon a 5:1 elliptical leading-edge. ($2T/\Delta\omega = 0.7$; $2T/\theta_R = 3.3$)

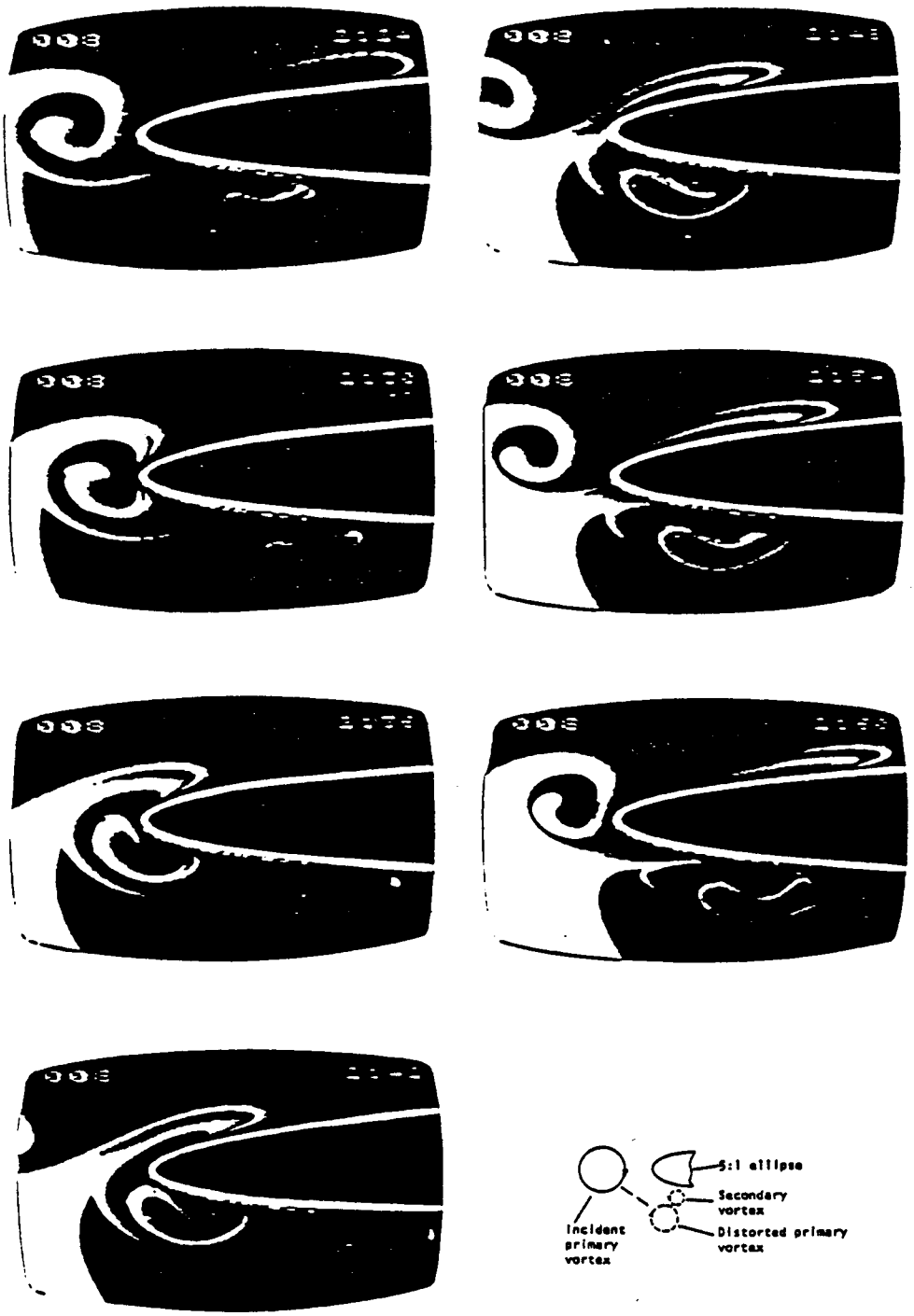

Figure 28. Effect of edge thickness on the interaction; vortex incident upon a 5:1 elliptical leading-edge. ($2T/\Delta\omega = 1.4$; $2T/\theta_R = 6.7$)

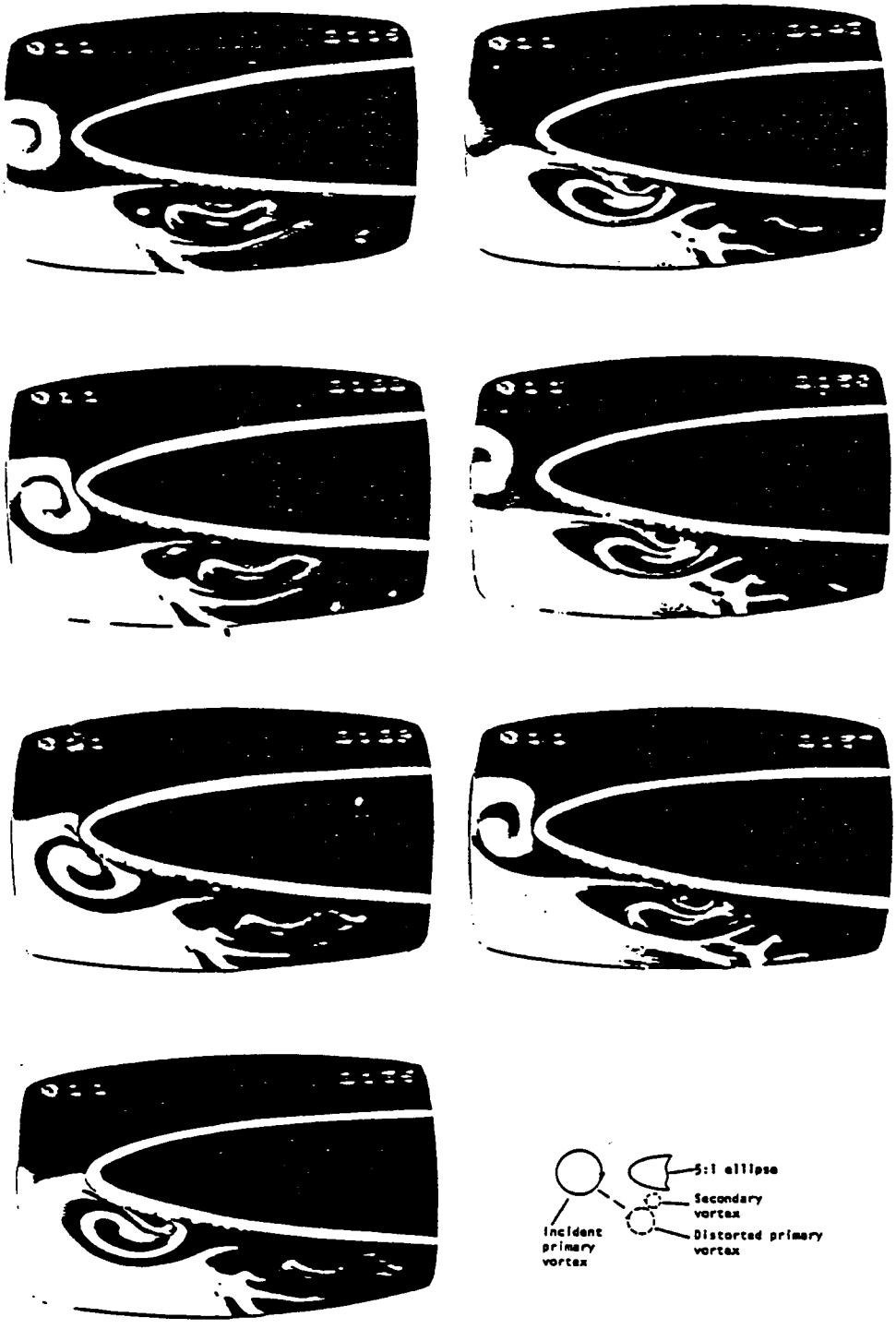

Figure 29. Effect of edge thickness on the interaction; vortex incident upon a 5:1 elliptical leading-edge. ($2T/\Delta\omega=4.2$; $2T/\theta_R=20.1$)

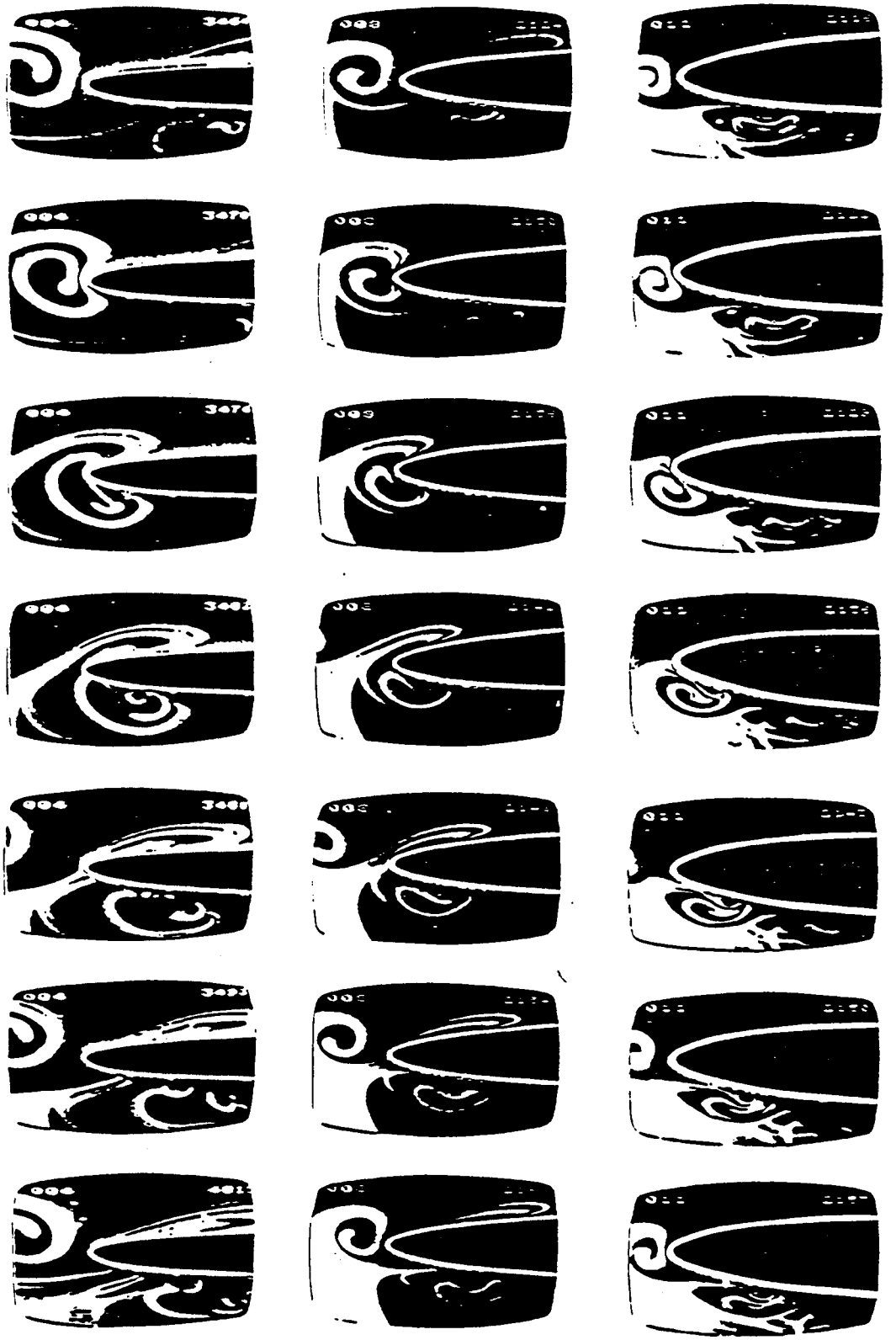

Figure 30. Effect of edge thickness on the interaction; comparison of different thickness 5:1 elliptical leading-edges.

Figure 31. Vortex interaction with 5:1 elliptical leading-edge; block of hydrogen bubble lines generated upstream of the leading-edge. ($\xi/2T = 0$)

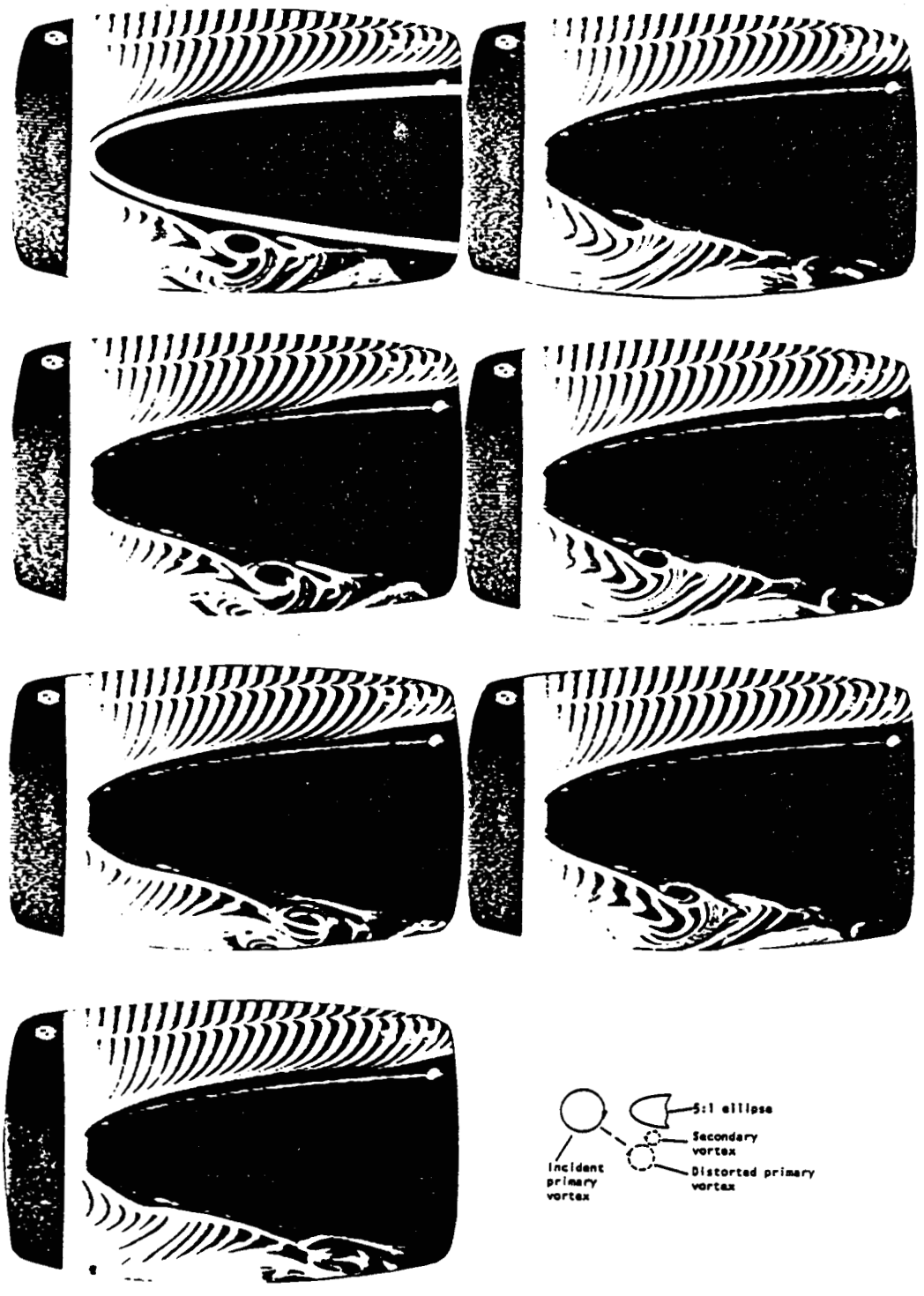

Figure 32. Vortex interaction with 5:1 elliptical leading-edge; finely pulsed hydrogen bubble lines generated at the tip of the leading-edge. ($\varepsilon/2T = 0$)

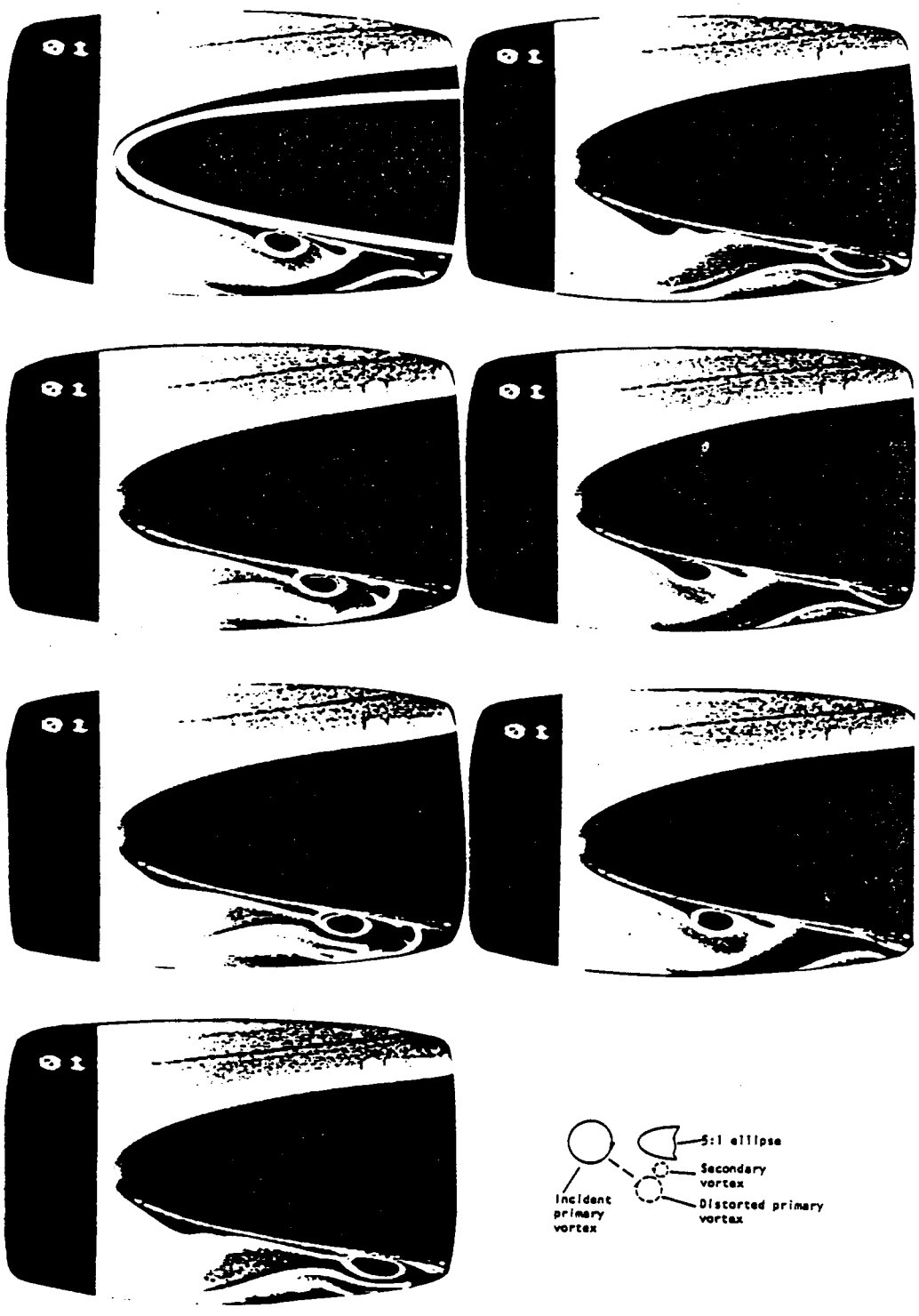

Figure 33. Vortex interaction with 5:1 elliptical leading-edge; continuous hydrogen bubble lines generated at the tip of the leading-edge. ($\xi/2T = 0$)

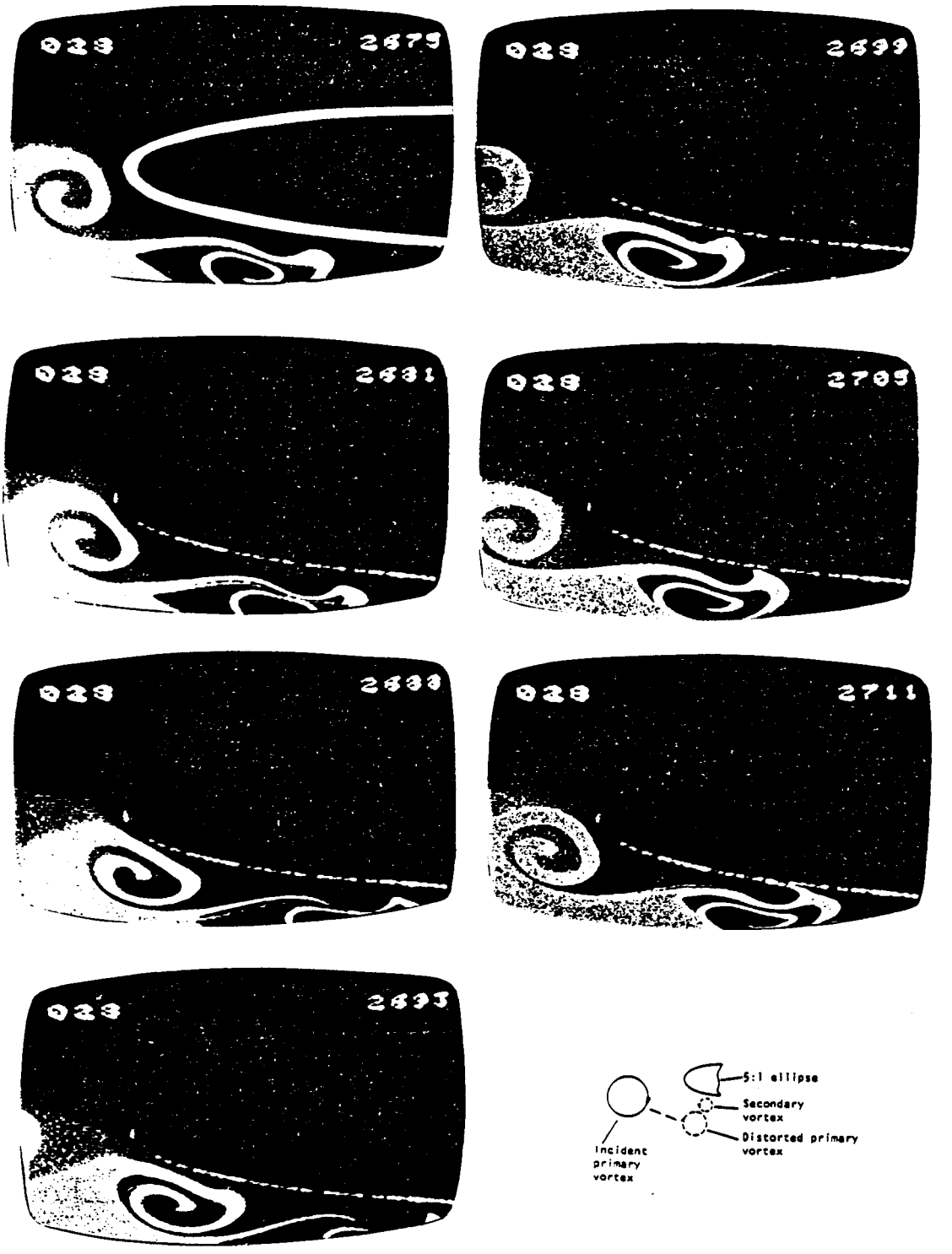

Figure 34. Vortex interaction with 5:1 elliptical leading-edge; block of hydrogen bubble lines generation upstream of the leading-edge. ($\xi/2T = 0.0$)

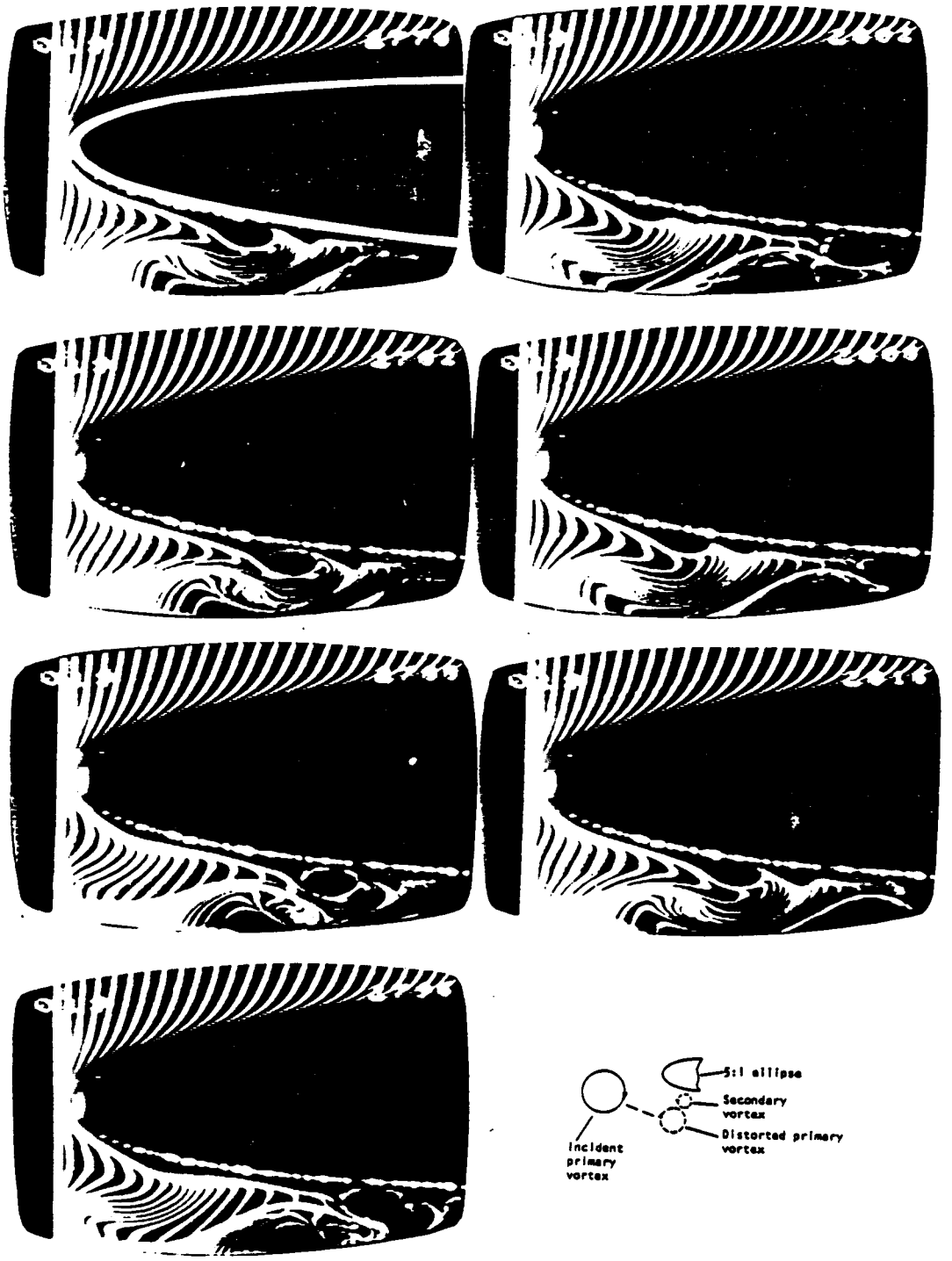

Figure 35. Vortex interaction with 5:1 elliptical leading-edge; finely pulsed hydrogen bubble lines generated at the tip of the leading-edge. ($\xi/2T = 0.1$)

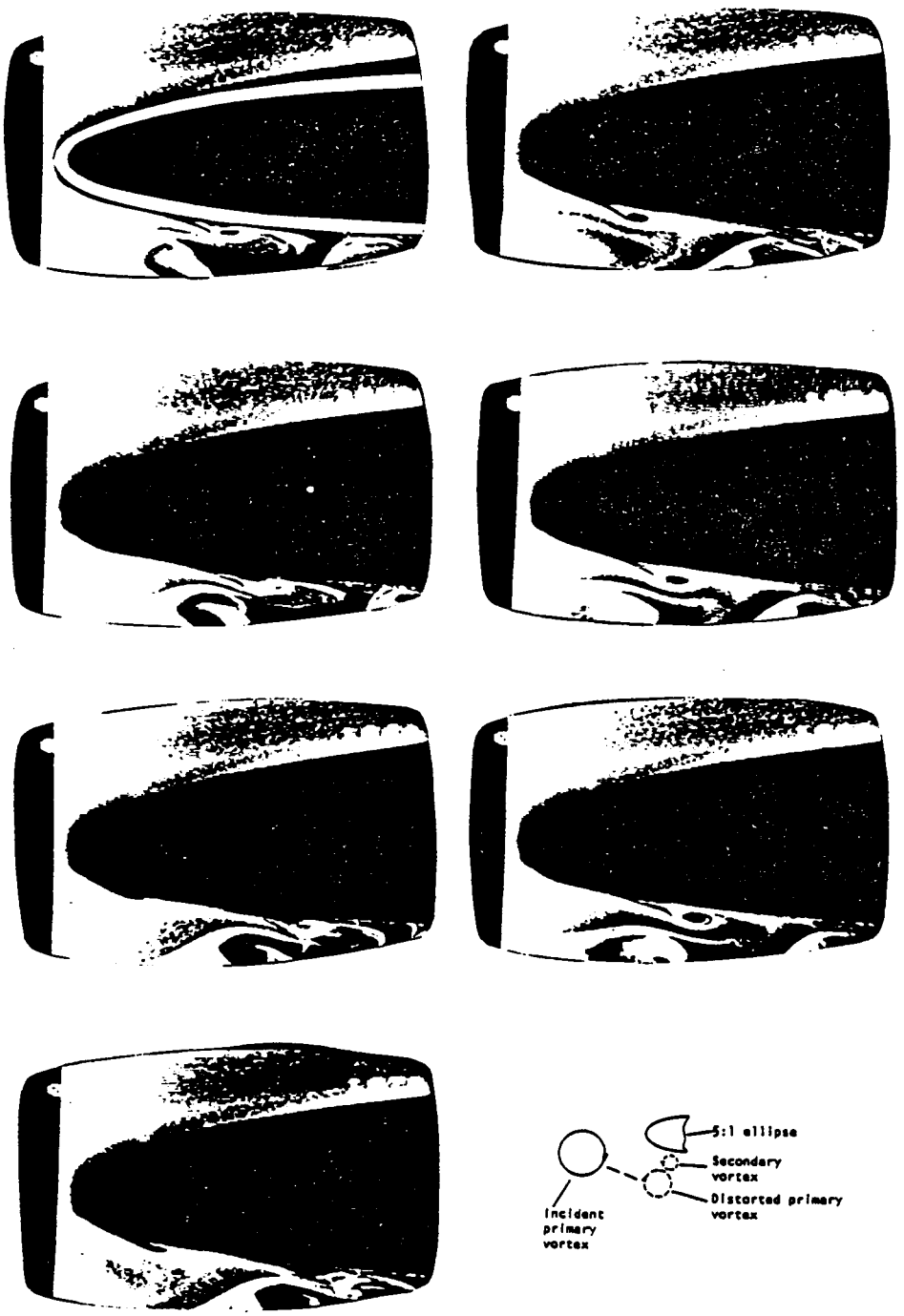

Figure 36. Vortex interaction with 5:1 elliptical leading-edge; continuous hydrogen bubble lines generated at the tip of the leading-edge. ($\xi/2T = 0.1$)

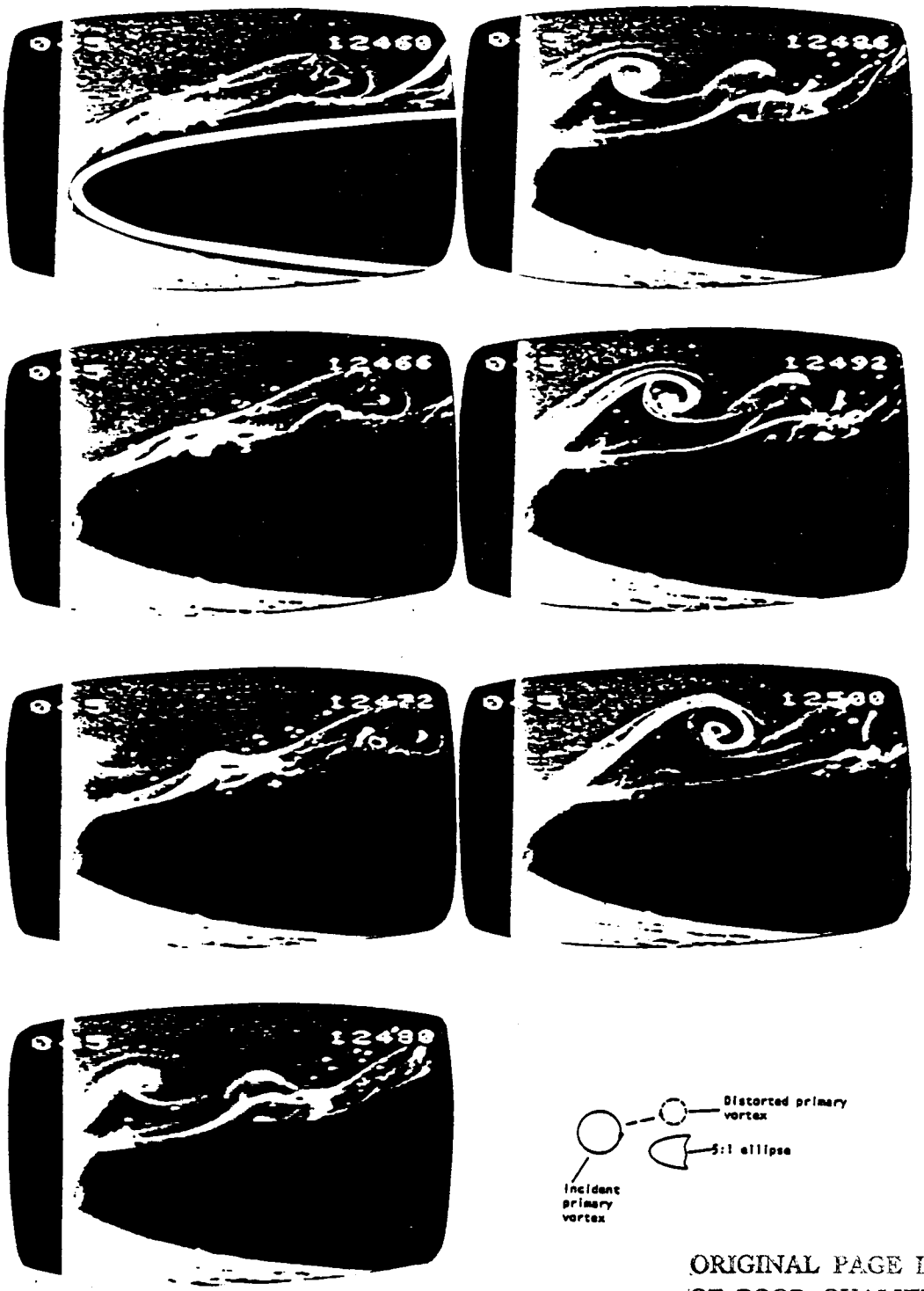

Figure 39. Vortex interaction with 5:1 elliptical leading-edge; continuous hydrogen bubble lines generated at the tip of the leading-edge. ($\xi/2T = -0.4$)

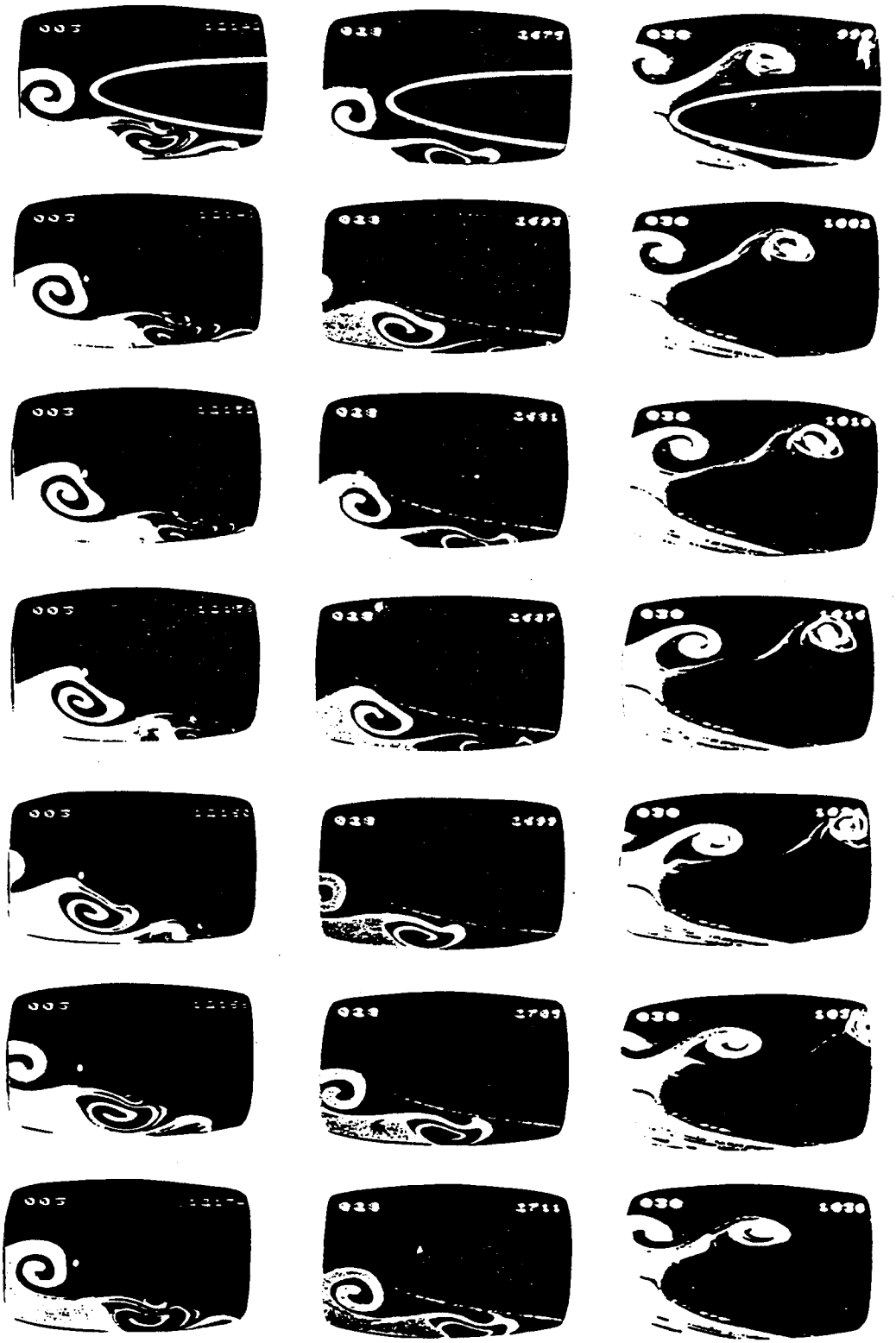

Figure 40. Effect of edge-vortex offset on the interaction; comparison of three different offset cases (block of hydrogen bubble lines generated upstream of the leading-edge).

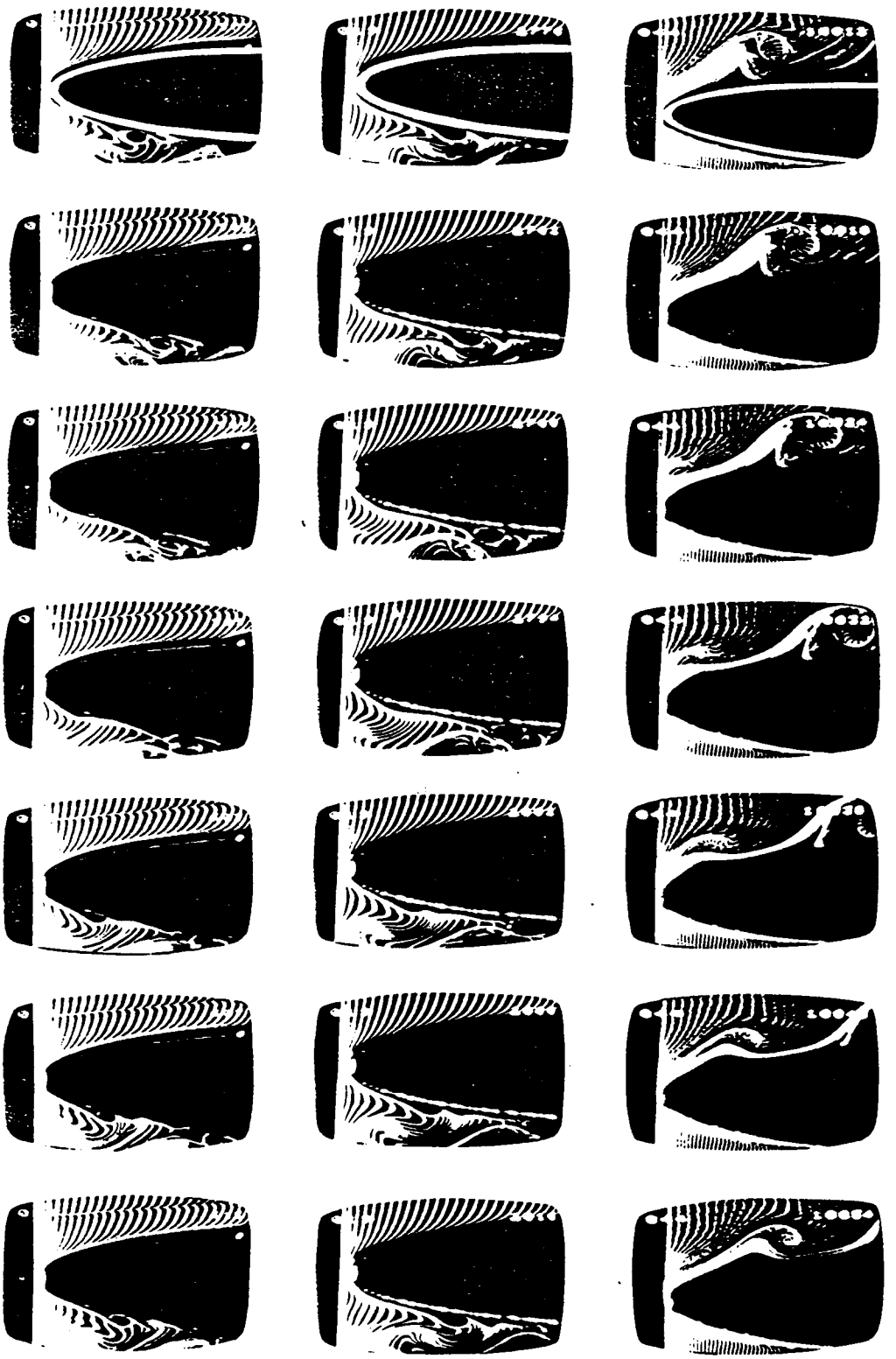

Figure 41. Effect of edge-vortex offset on the interaction; comparison of three different offset cases (finely pulsed hydrogen bubble lines generated at the tip of the leading-edge).

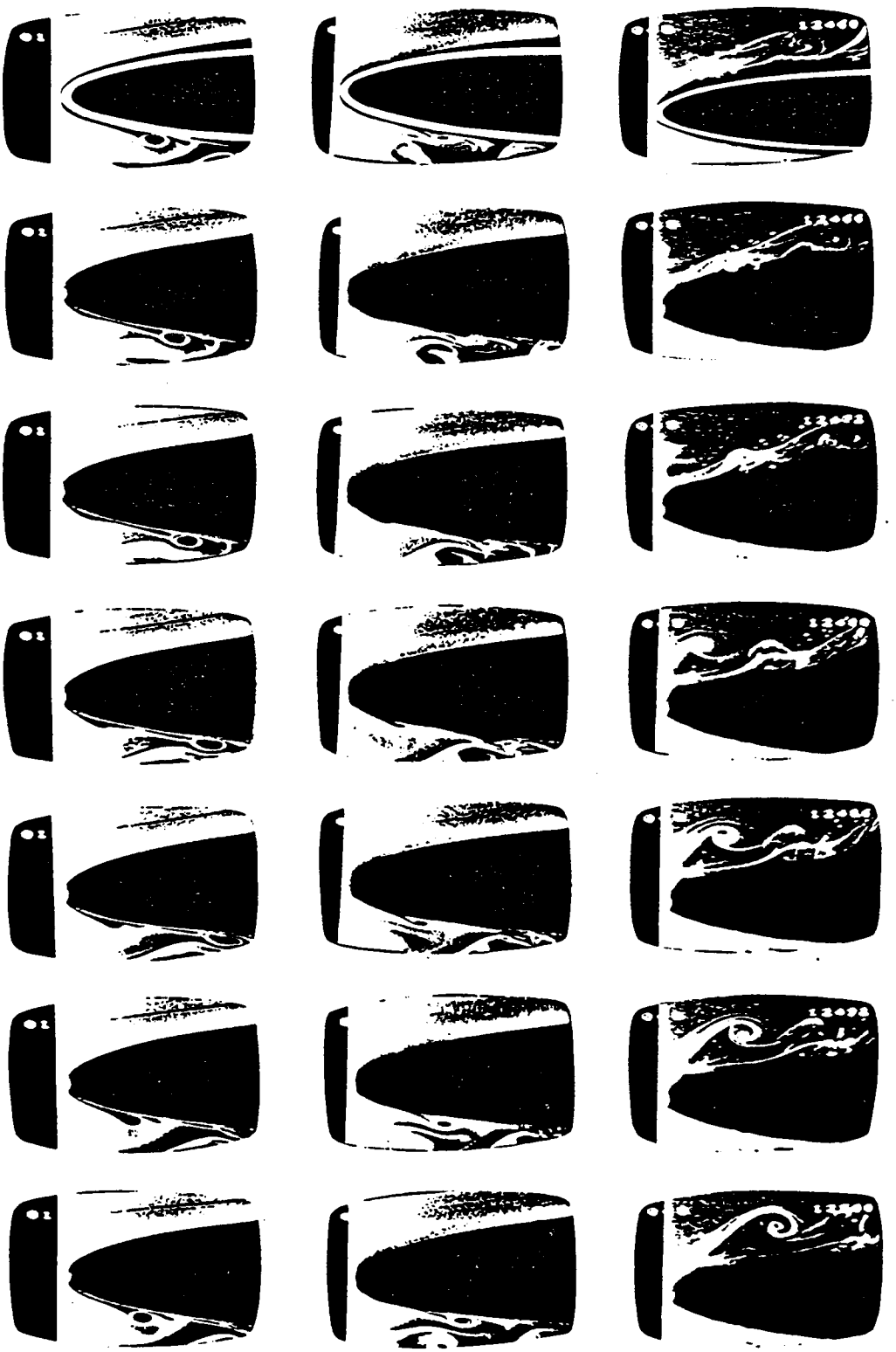

Figure 42. Effect of edge-vortex offset on the interaction; comparison of three different offset cases (continuous hydrogen bubble lines generated at the tip of the leading-edge.

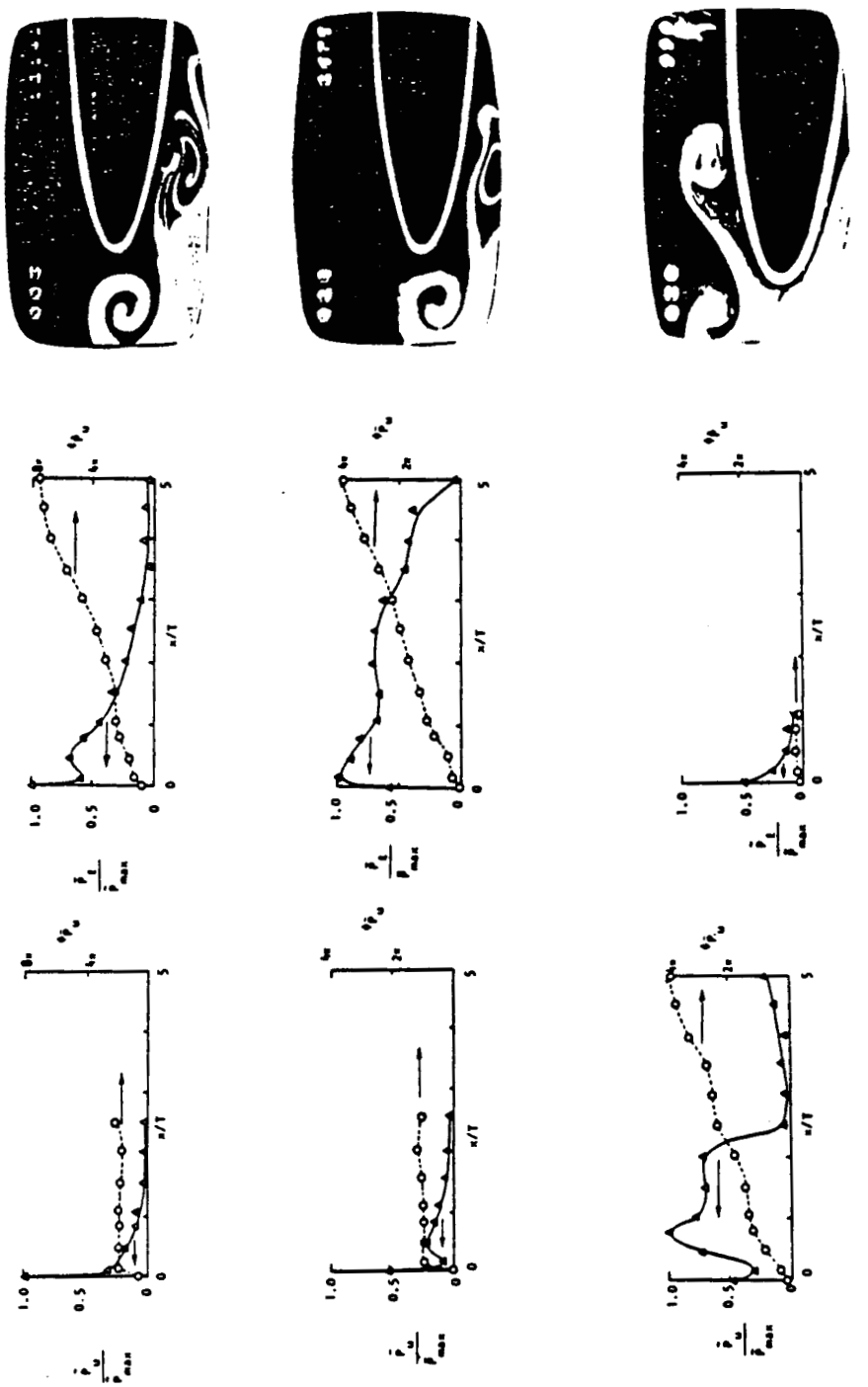

Figure 43. Amplitude and phase variation of fluctuating pressure field on upper and lower surfaces of leading-edge for three different offset cases ($\xi/2T=0$, 0.1, -0.4).

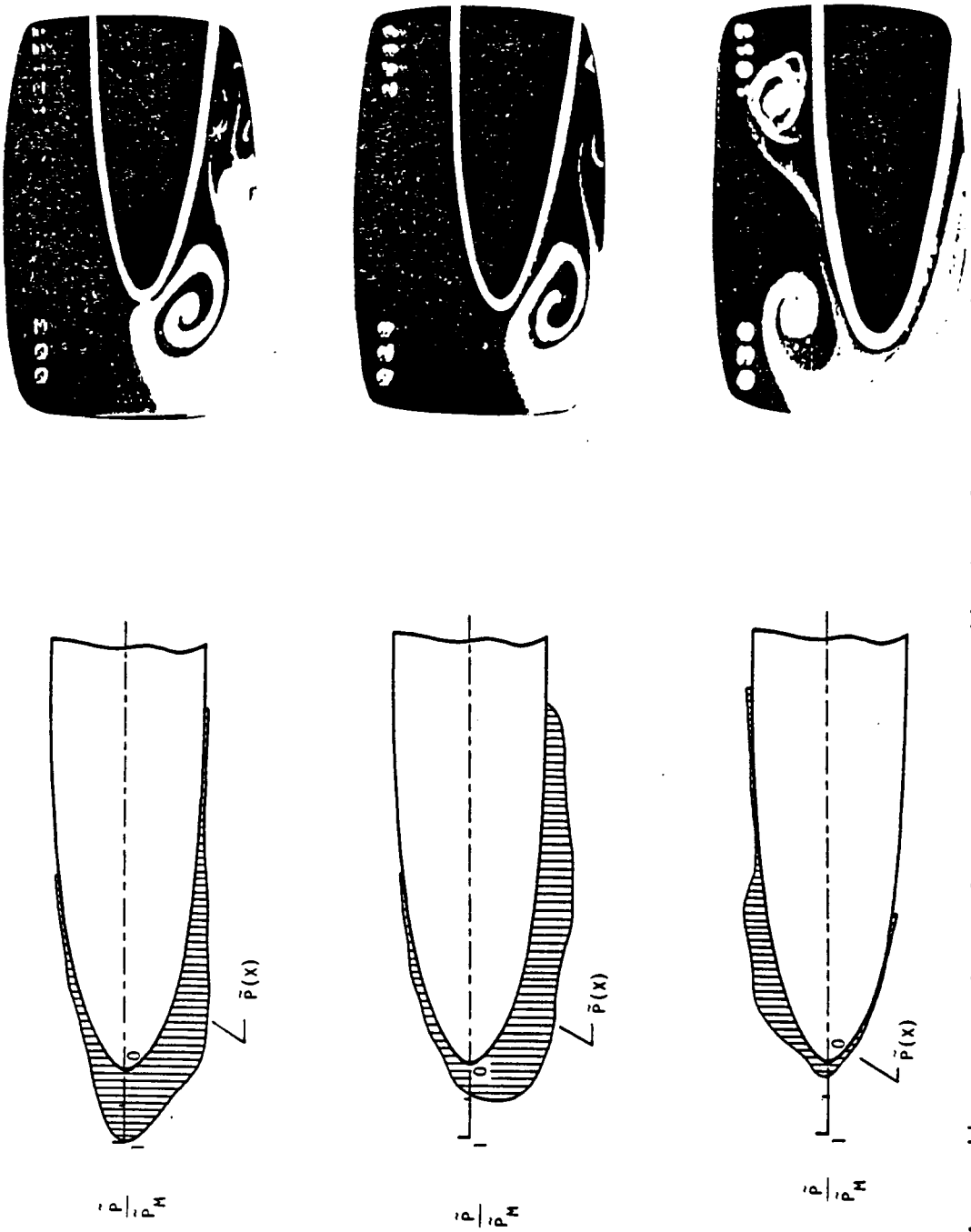

Figure 44. Comparison of rms pressure amplitudes along the leading-edge for three different offset cases; $\tilde{P}$=rms pressure amplitude $\tilde{P}_M$=absolute maximum rms pressure amplitude ($\xi/2T$=0, 0.1, -0.4).

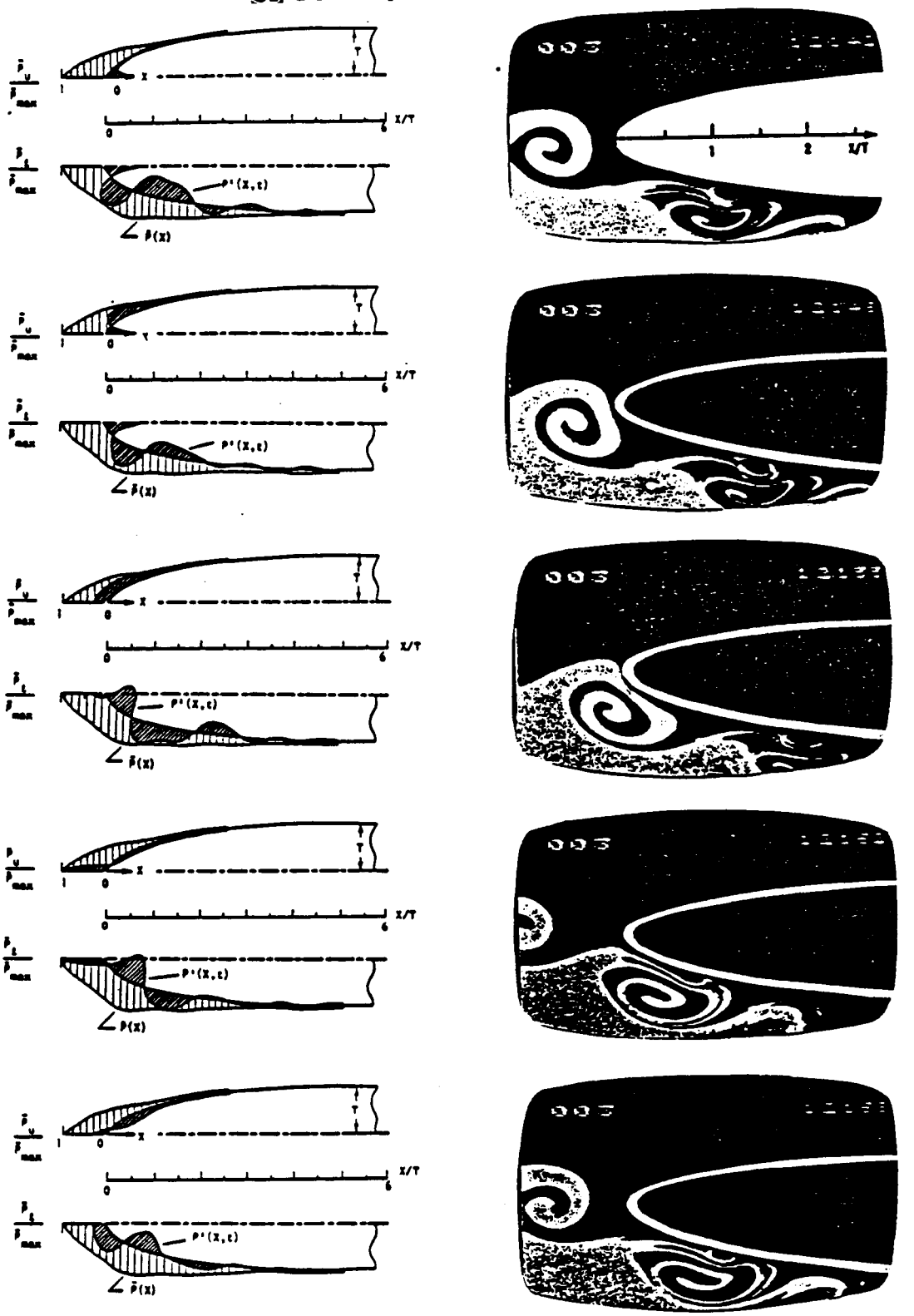

Figure 45. Instantaneous pressure fields and corresponding vortex-edge interaction mechanisms for various locations of vortex relative to leading-edge; i.e. for different times (t=0, 1/5 T, 2/5 T, 3/5 T, 4/5 T; $\xi/2T=0$).

C-2

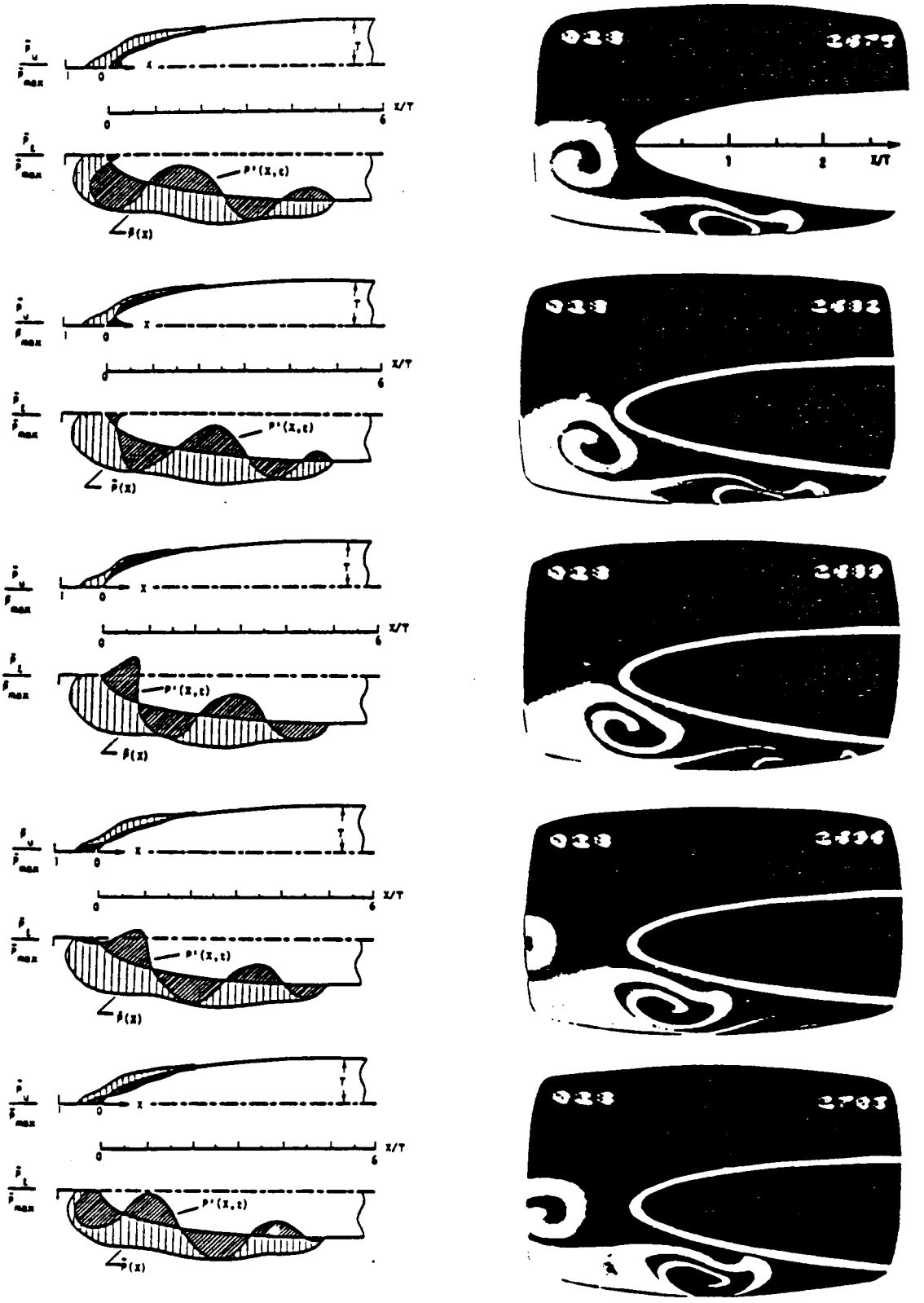

Figure 46. Instantaneous pressure fields and corresponding vortex-edge interaction mechanisms for various locations of vortex relative to leading-edge; i.e. for different times (t=0, 1/5 T, 2/5 T, 3/5 T, 4/5 T; $\xi/2T=0.1$).

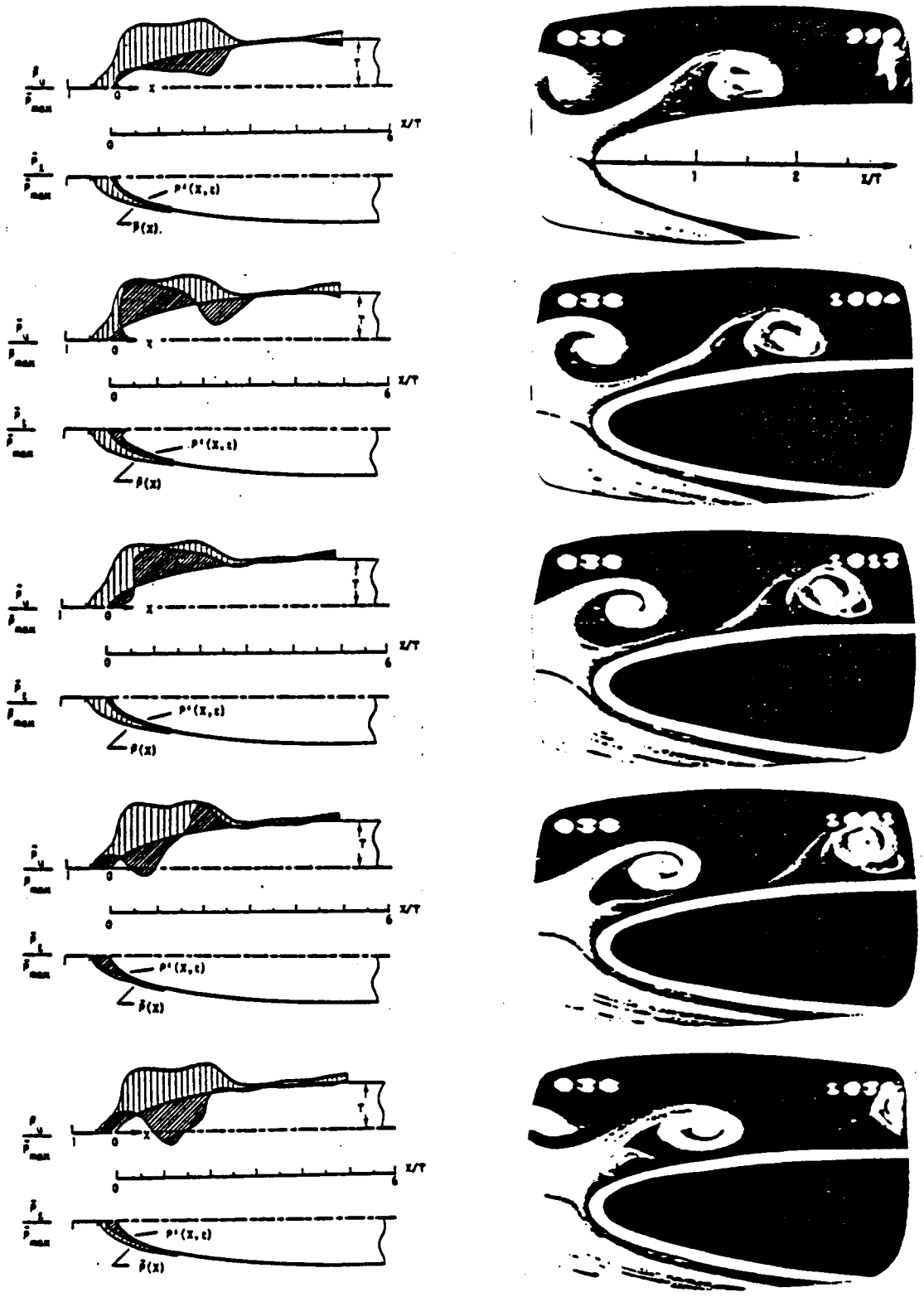

Figure 47. Instantaneous pressure fields and corresponding vortex-edge interaction mechanisms for various locations of vortex relative to leading-edge; i.e. for different times (t=0, 1/5 T, 2/5 T, 3/5 T, 4/5 T; $\xi/2T=-0.4$).

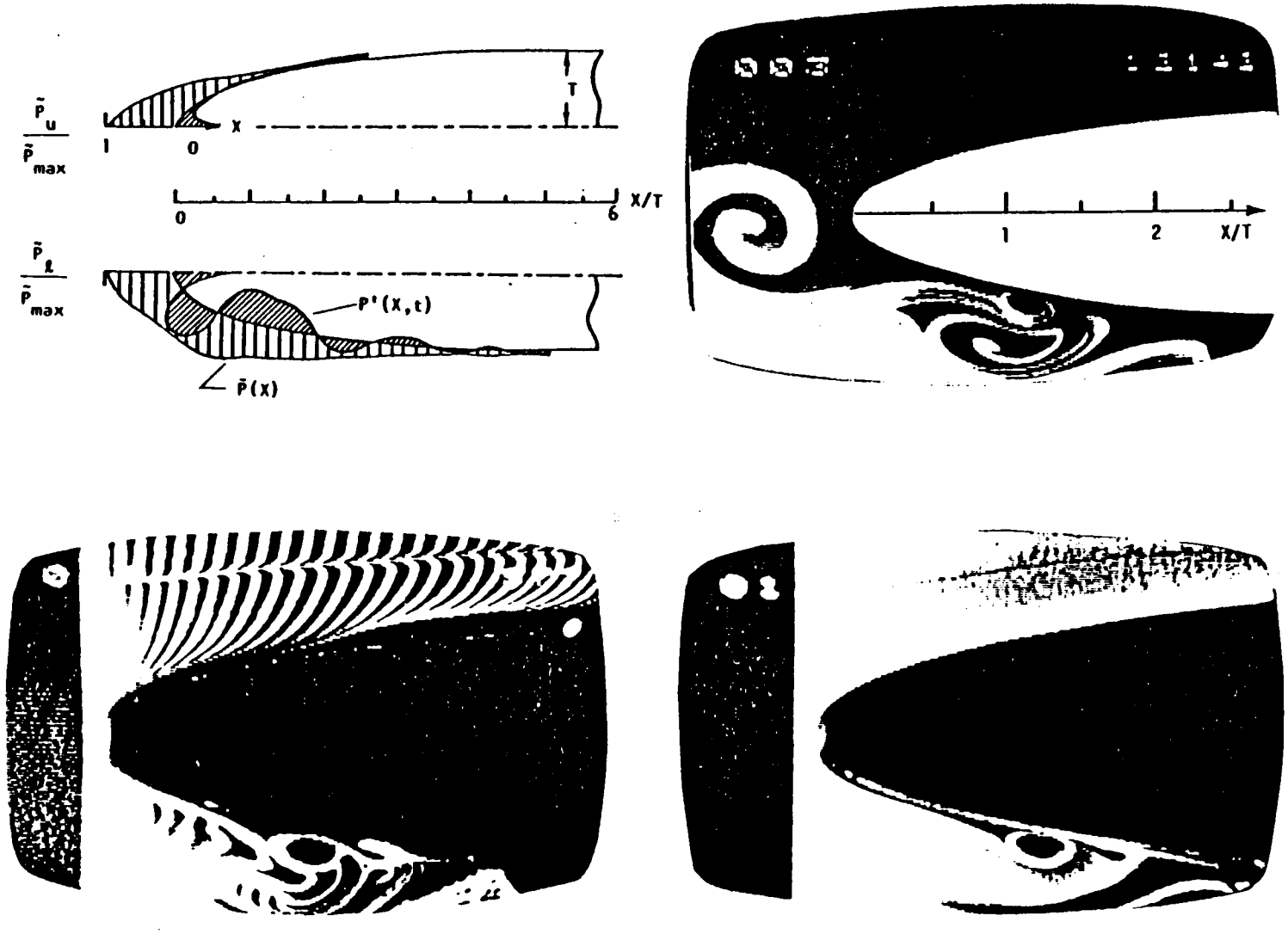

Figure 48. Instantaneous pressure fields and three different visualizations of corresponding flow field at t=0 ($\xi/2T=0$).

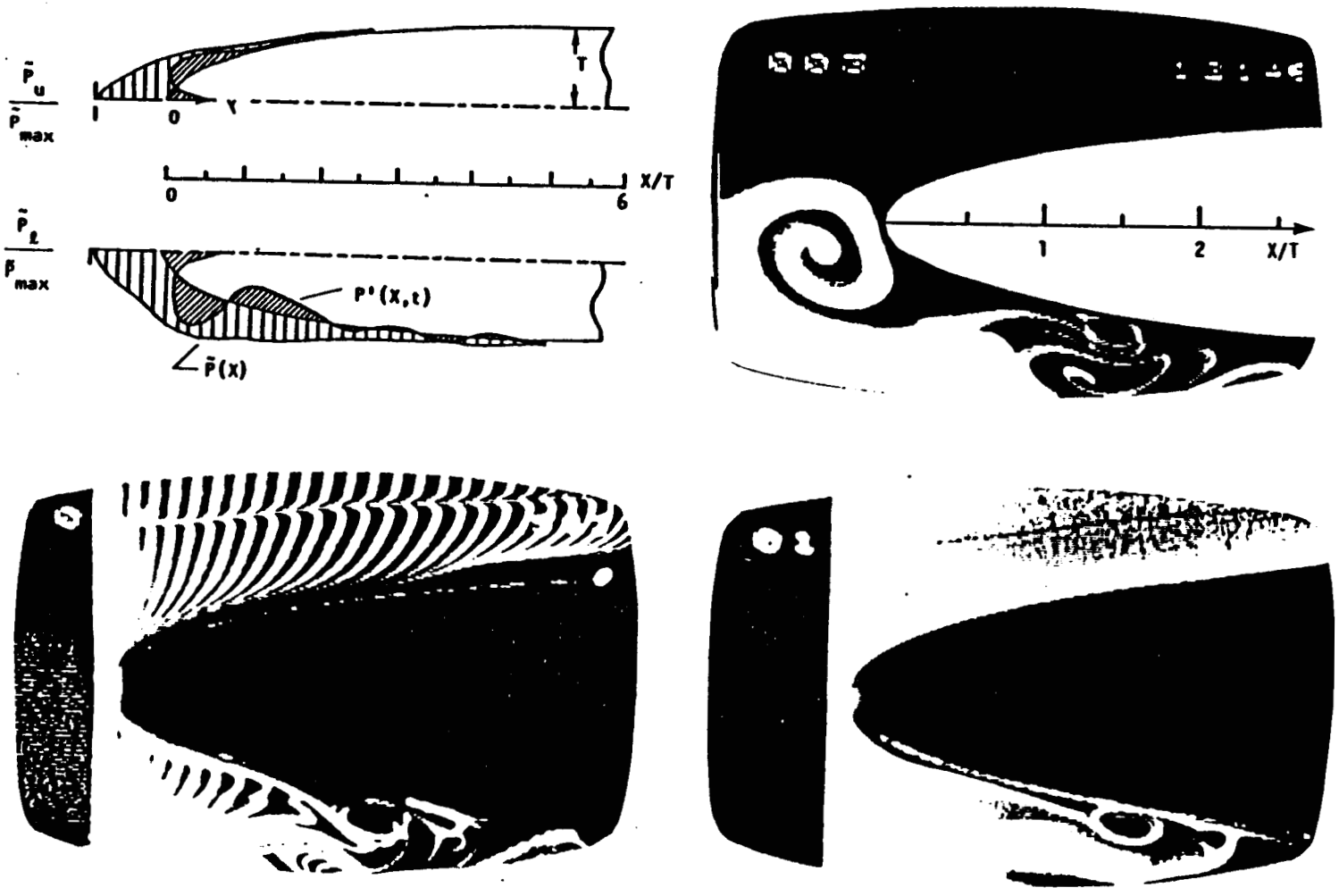

Figure 49. Instantaneous pressure fields and three different visualizations of corresponding flow at t=T/5 ($\xi/2T=0$).

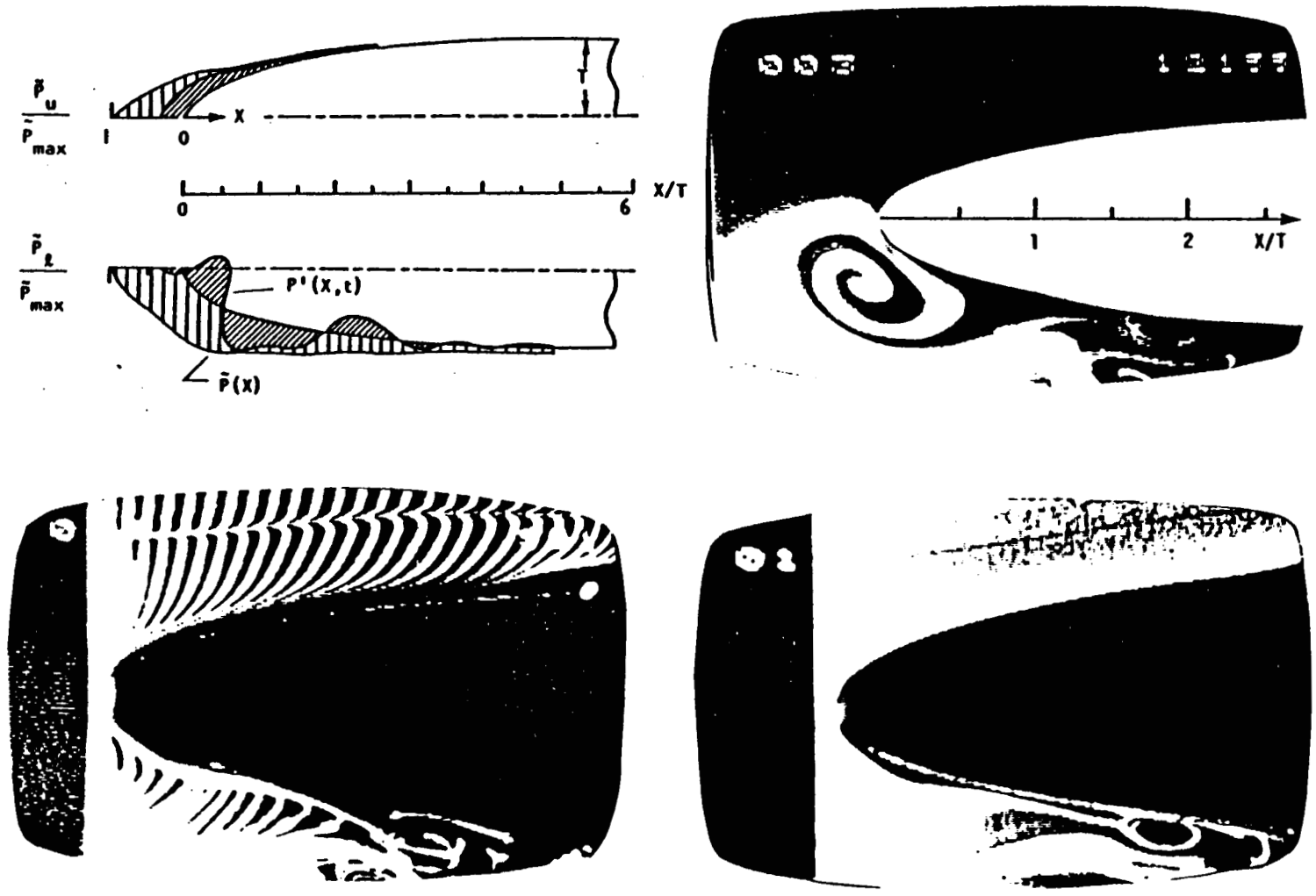

Figure 50. Instantaneous pressure fields and three different visualizations of corresponding flow field at t=2T/5 (ξ/2T=0).

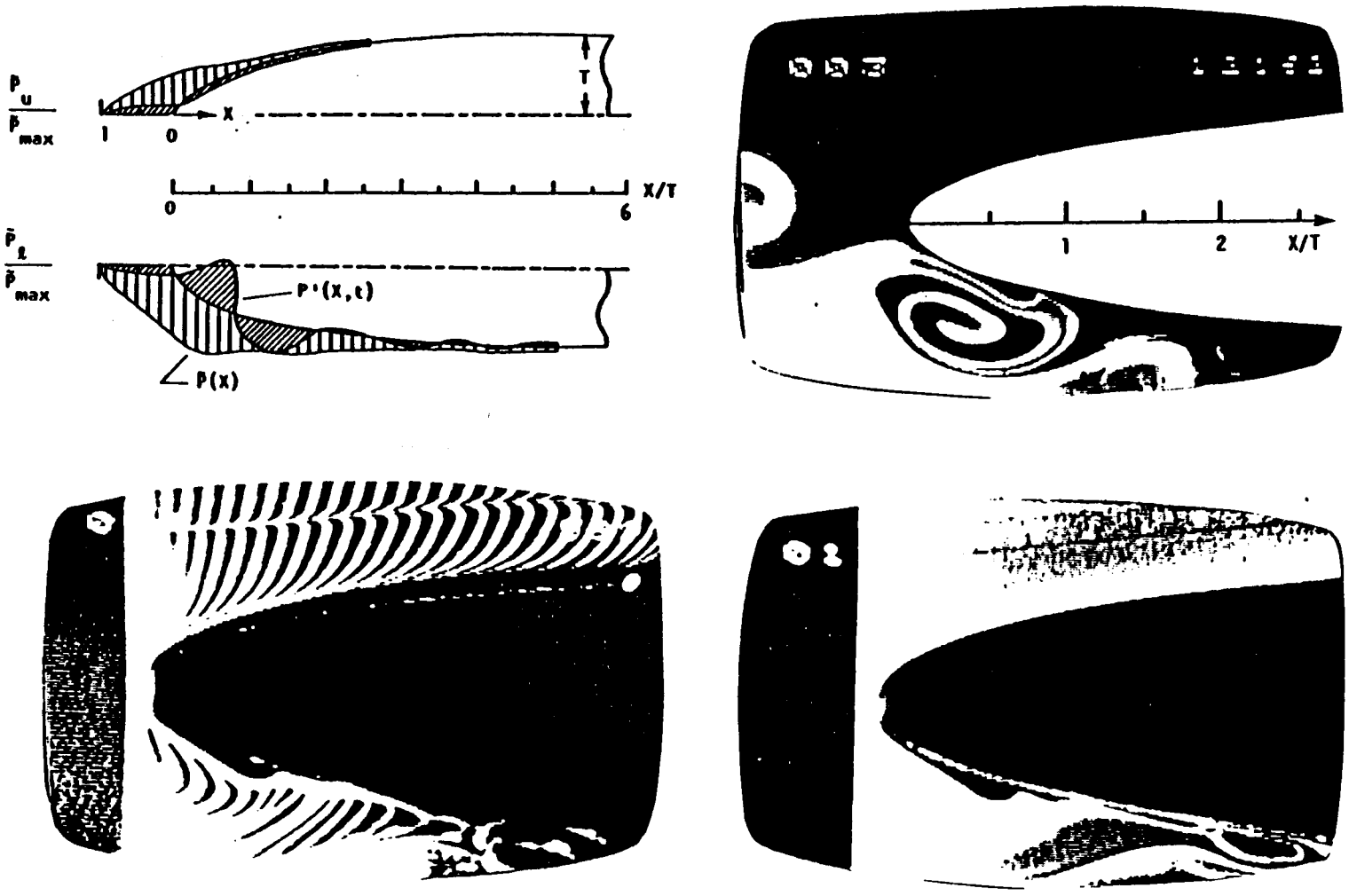

Figure 51. Instantaneous pressure fields and three different visualizations of corresponding flow field at t=3T/5 ($\xi/2T=0$).

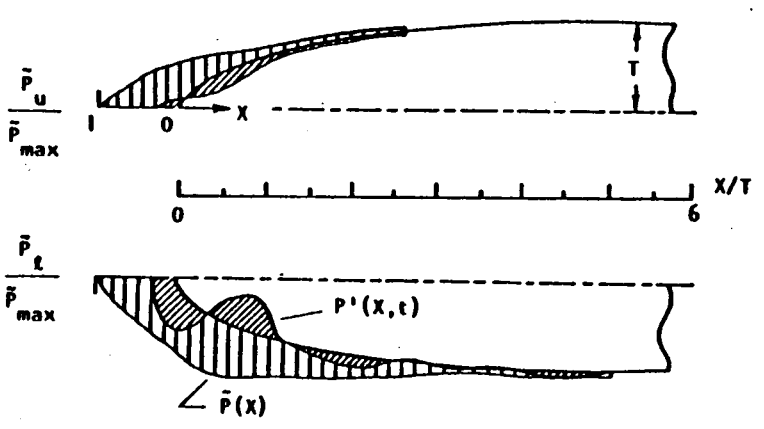

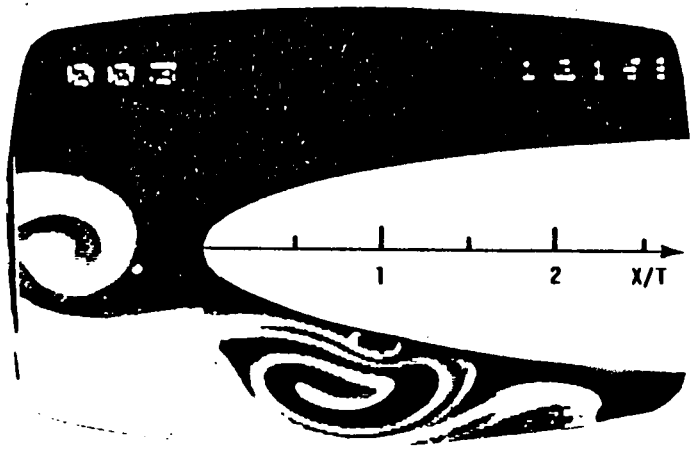

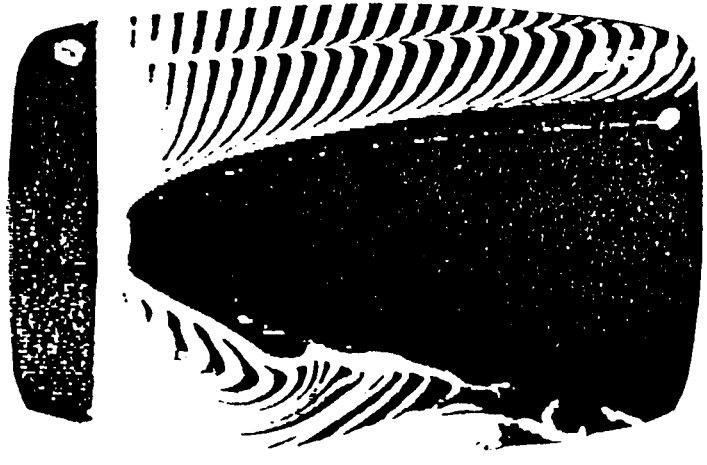

Figure 52. Instantaneous pressure fields and three different visualizations of corresponding flow field at t=4T/5 (ξ/2T=0).

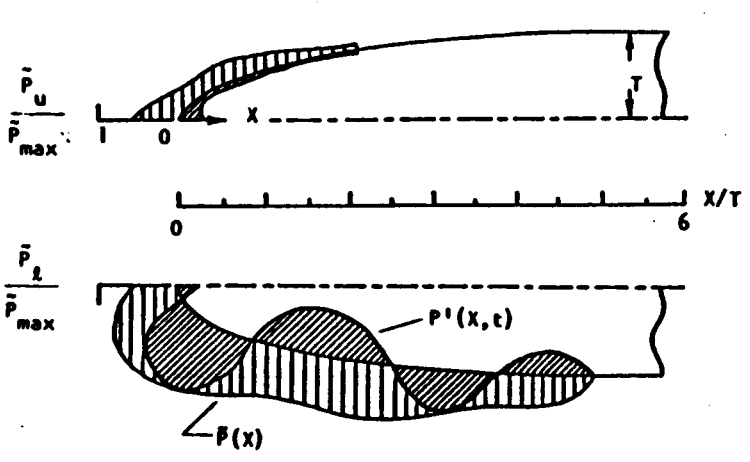

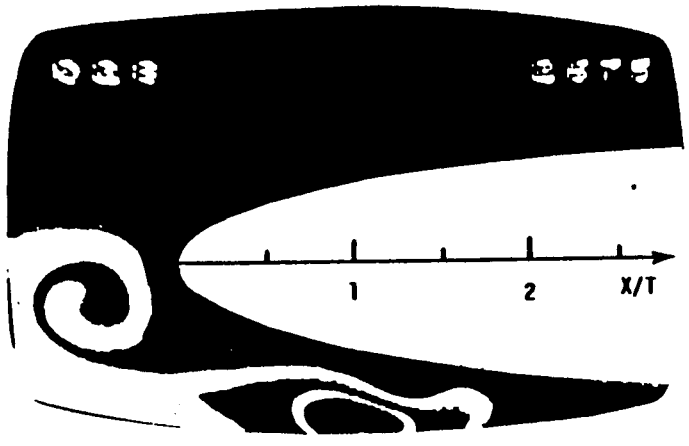

Figure 53. Instantaneous pressure fields and three different visualizations of corresponding flow field at t=0 ($\xi/2T=0.1$).

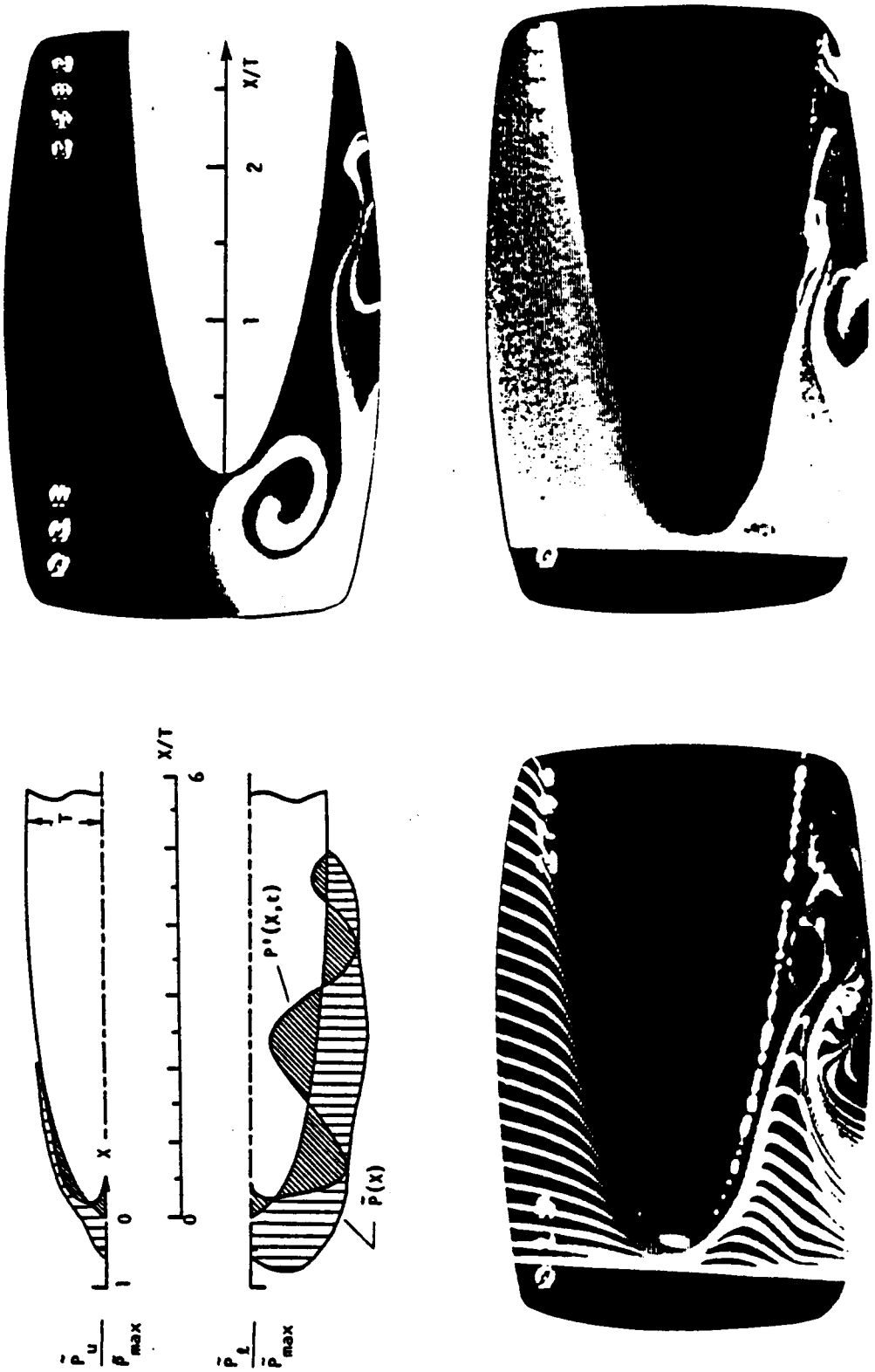

Figure 54. Instantaneous pressure fields and three different visualizations of corresponding flow field at t=T/5 (ξ/2T=0.1).

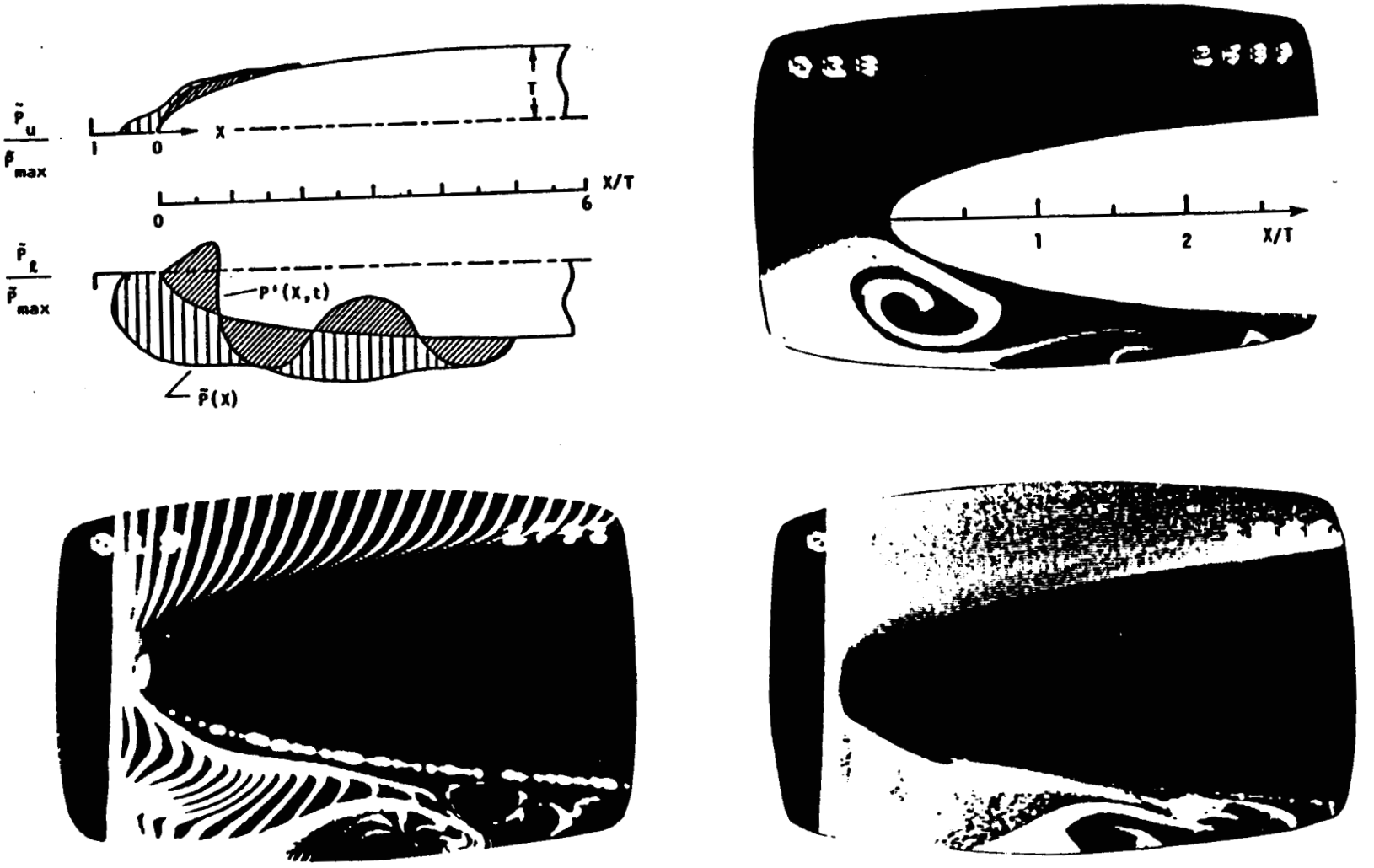

Figure 55. Instantaneous pressure fields and three different visualizations of corresponding flow field at t=2T/5 (ξ/2T=0.1).

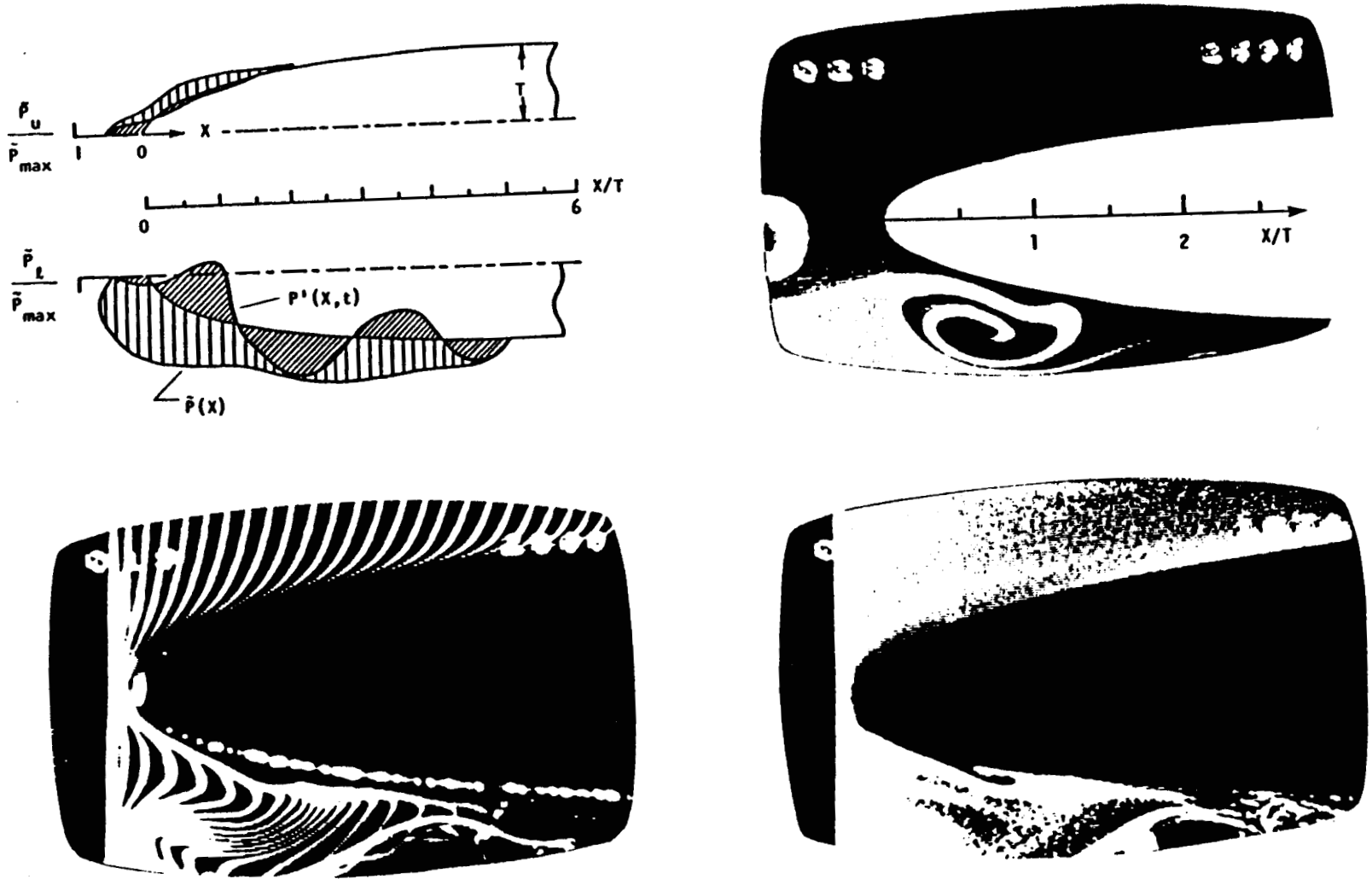

Figure 56. Instantaneous pressure fields and three different visualizations of corresponding flow field at t=3T/5 (ξ/2T=0.1).

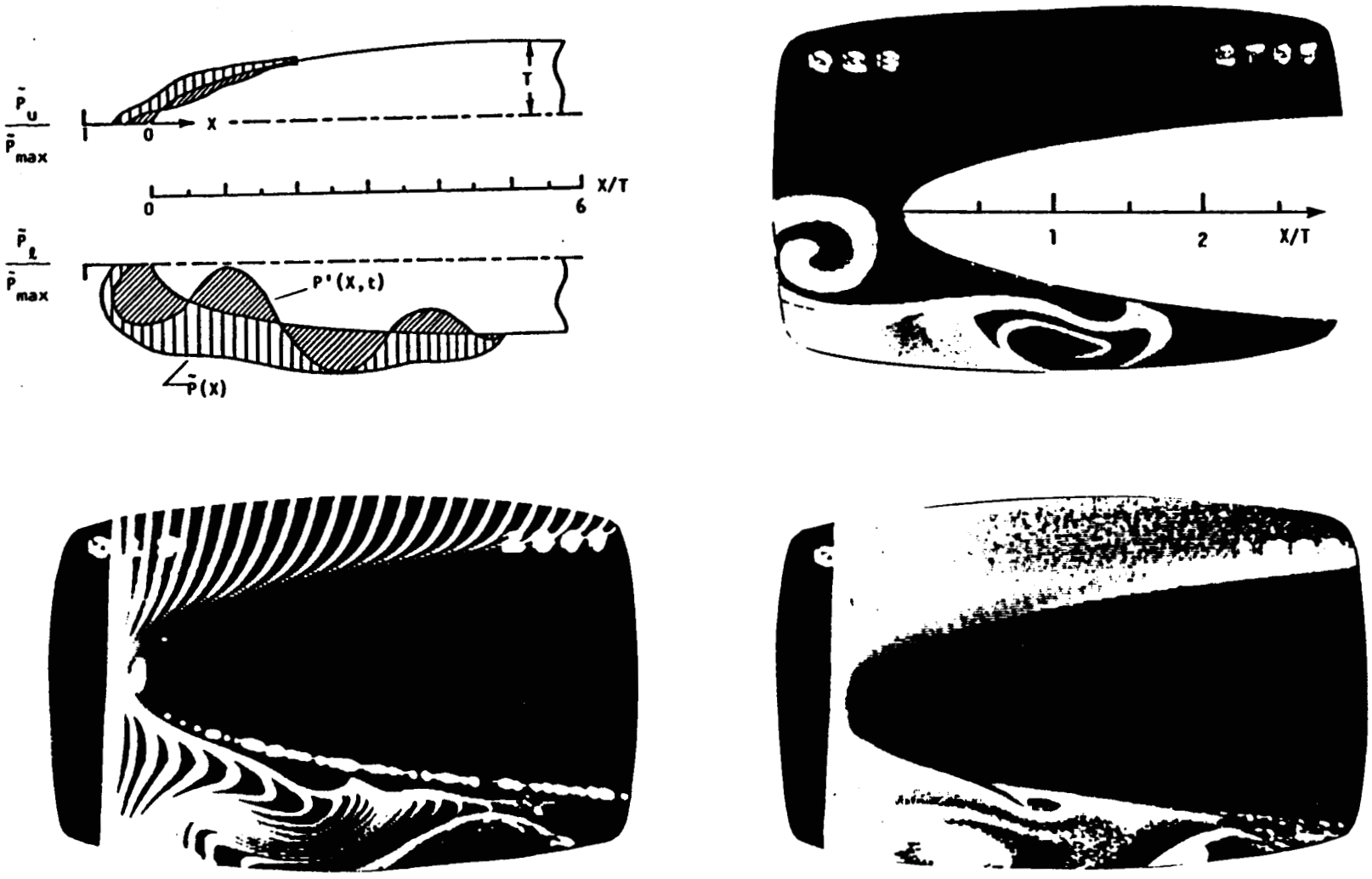

Figure 57. Instantaneous pressure fields and three different visualizations of corresponding flow field at t=4T/5 (ξ/2T=0.1).

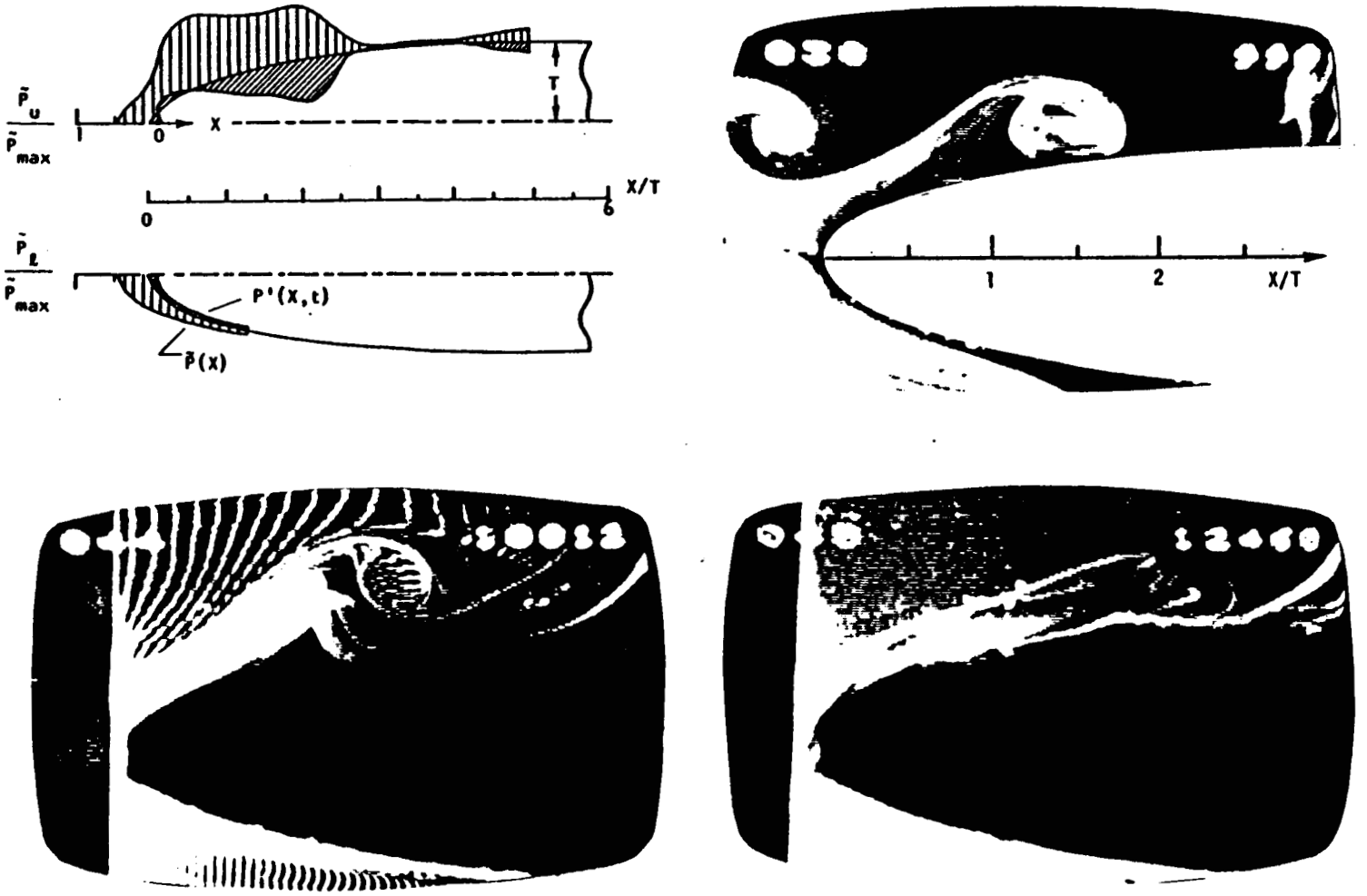

Figure 58. Instantaneous pressure fields and three different visualizations of corresponding flow field at t=0 ($\xi/2T=-0.4$).

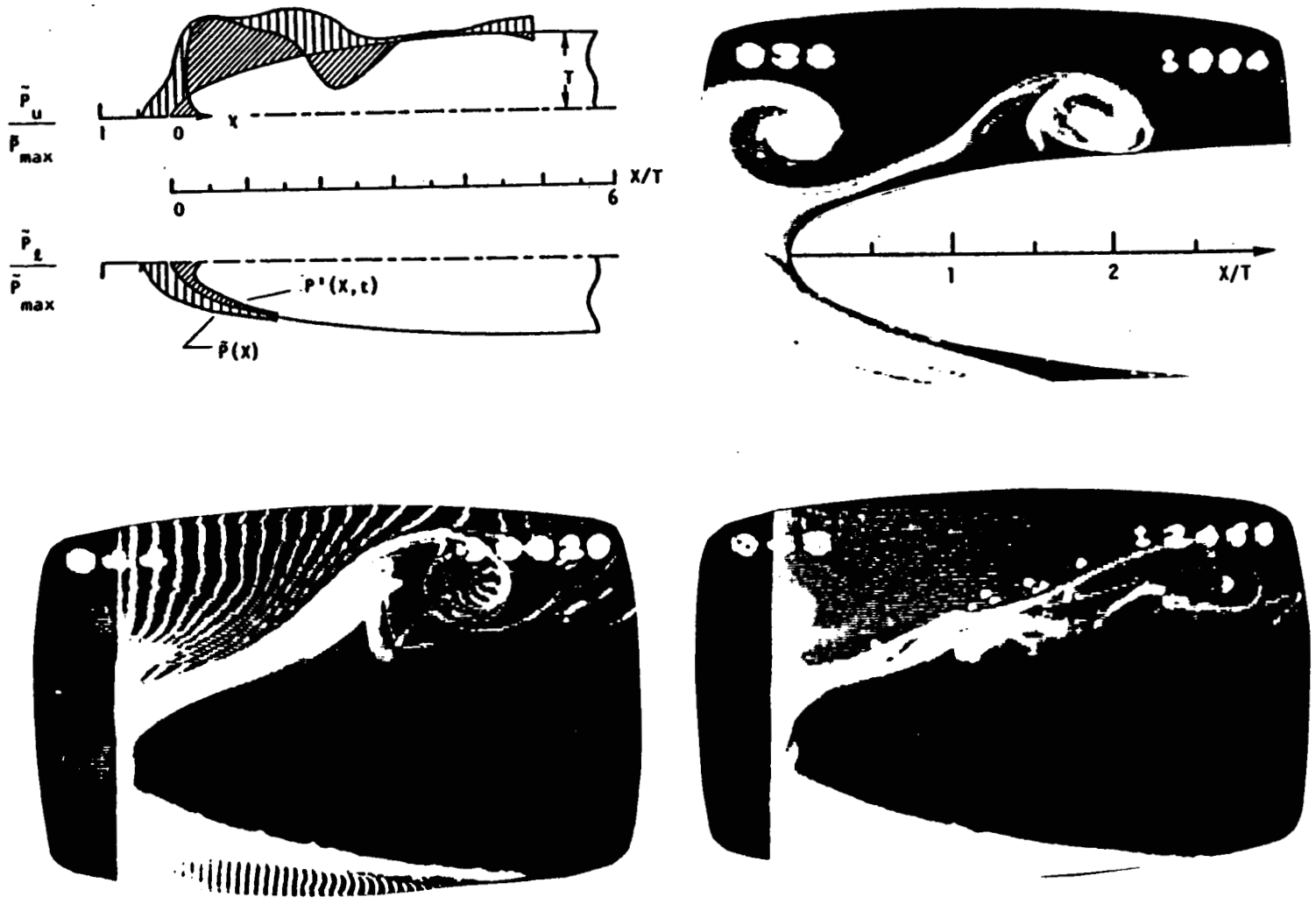

Figure 59. Instantaneous pressure fields and three different visualizations of corresponding flow field at t=T/5 ($\xi/2T=-0,4$).

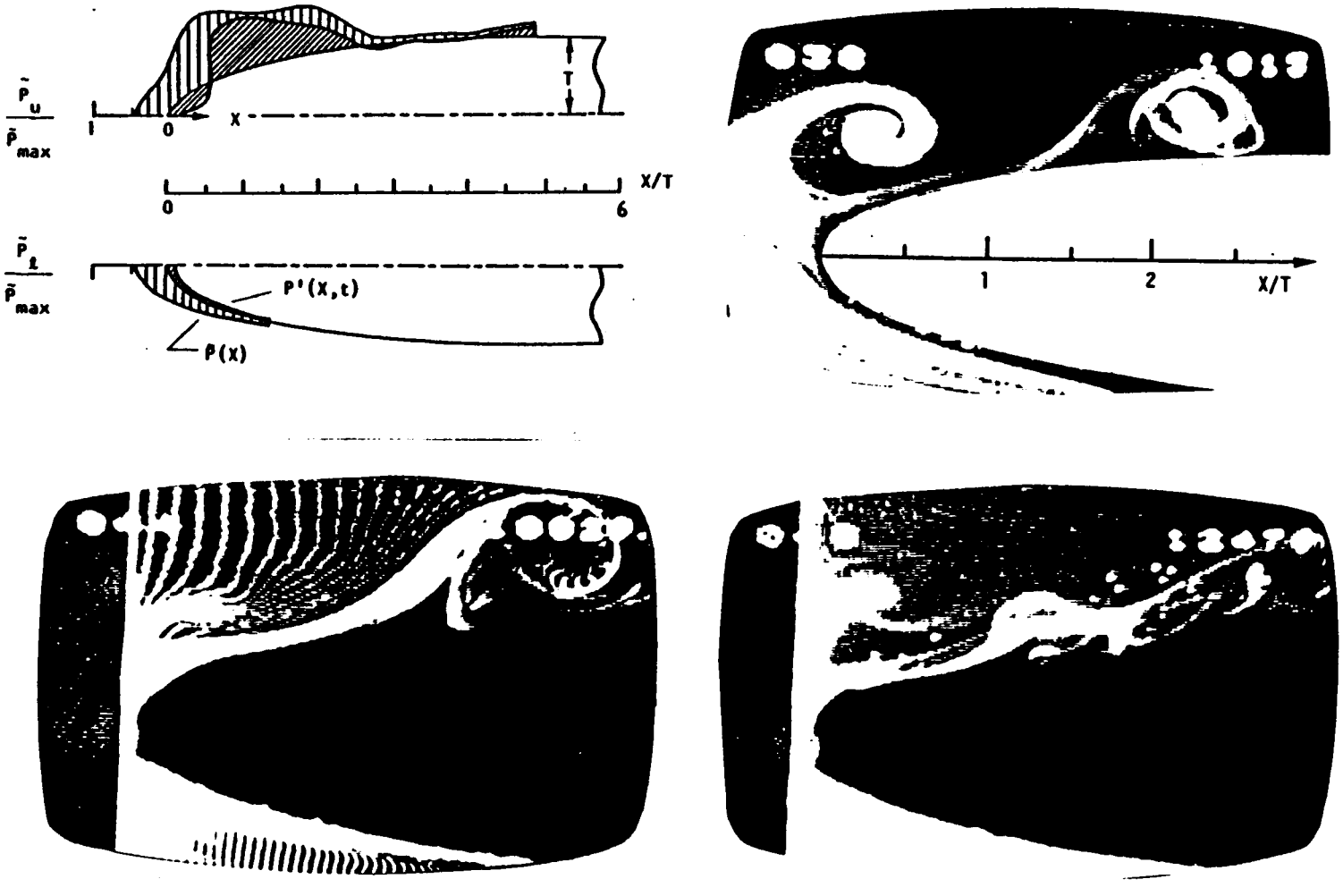

Figure 60. Instantaneous pressure fields and three different visualizations of corresponding flow field at t=2T/5 ($\xi/2T=-0.4$).

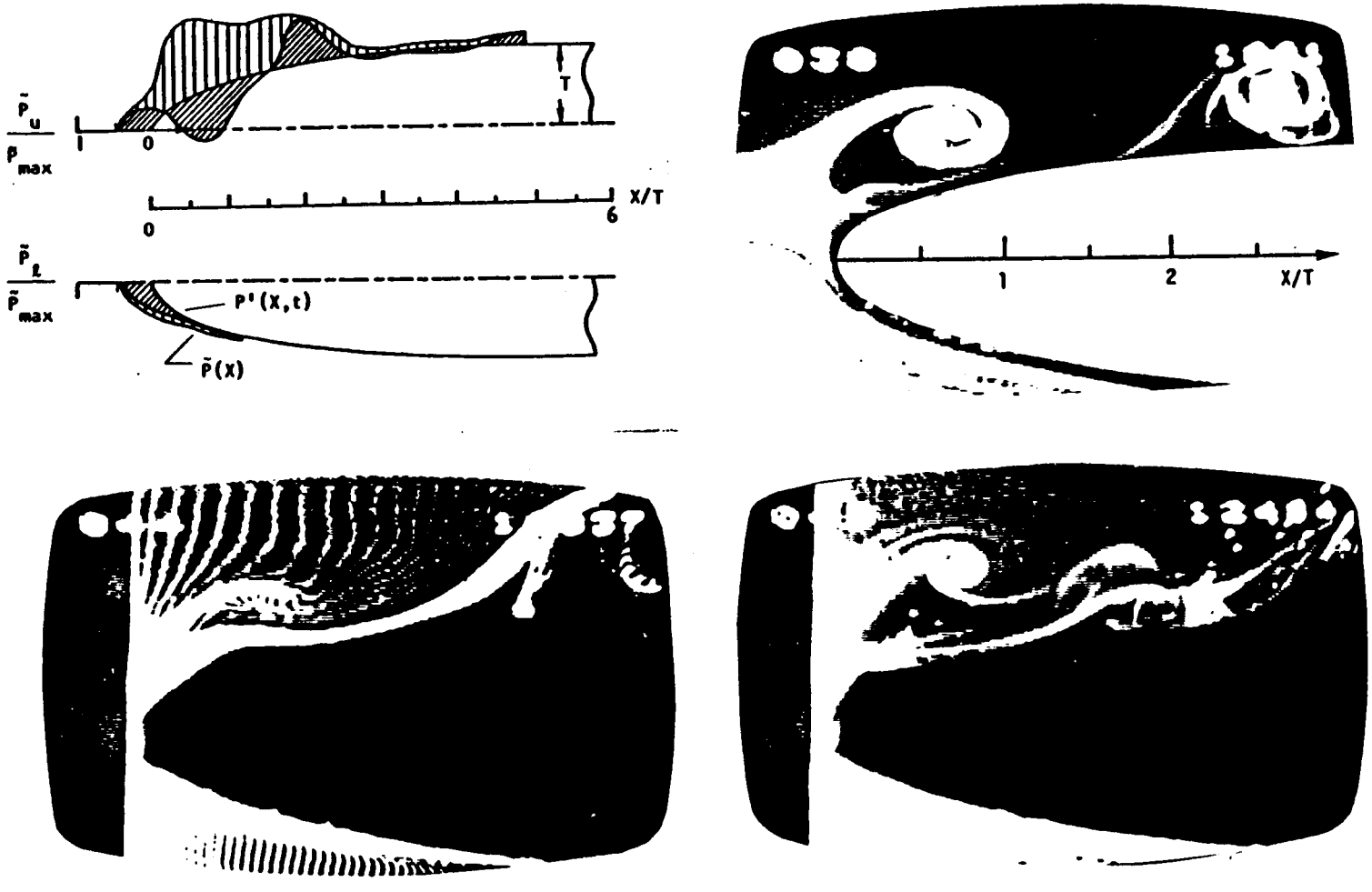

Figure 61. Instantaneous pressure fields and three different visualizations of corresponding flow field at t=3T/5 ($\xi/2T=-0.4$).

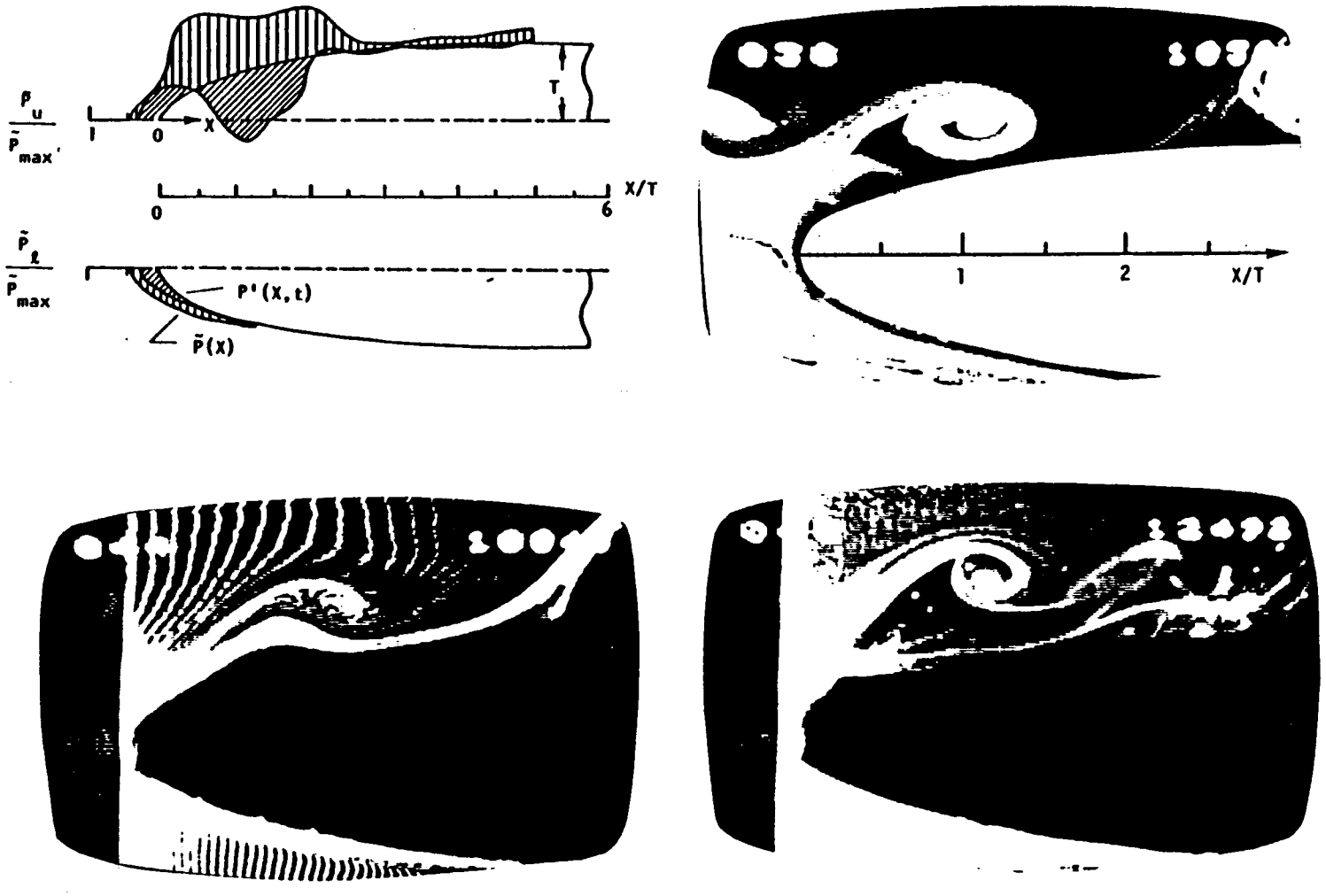

Figure 62. Instantaneous pressure fields and three different visualizations of corresponding flow field at t=4T/5 ($\xi/2T=-0.4$).

References

Booth Jr., E. R. and Yu, J. C. 1984 "Two Dimensional Blade-Vortex Interaction Flow Visualization Investigation", AIAA Paper No. 84-2307, presented at the 9th Aeroacoustics Conference, October 15-17, Williamsburg, Virginia.

Bushnell, D. M. 1984 "Body-Turbulence Interaction", AIAA Paper No. 84-1527, presented at 17th AIAA Fluid-Dynamics, Plasma Dynamics, and Laser Conference, June 25-27, Snowmass, Colorado.

Erwin, J. R. 1964 "Experimental Techniques", Section D of Aerodynamics of Turbines and Compressors, Princeton University Press.

Freymuth, P. 1966 "On Transition in a Separated Laminar Boundary Layer", Journal of Fluid Mechanics, Vol. 25, Part 4, pp. 683-704.

Ham, N. D. 1974 "Some Preliminary Results from an Investigation of Blade-Vortex Interaction", Journal of the American Helicopter Society, Vol. 19, April, pp. 45-48.

Homa, J. 1984 "Interactions of an Impulsively-Generated Two-Dimensional Vortex Pair with Flat Plates and Cylinders", M. S. Thesis, Department of Mechanical Engineering and Mechanics, Lehigh University, Bethlehem, Pennsylvania.

Kaykayoglu, R. and Rockwell, D. 1985 "Vortices Incident Upon a Leading-Edge: Instantaneous Pressure Fields", Journal of Fluid Mechanics, Vol. 156, pp. 439-461.

Kaykayoglu, R. and Rockwell, D. 1986a "Unstable jet-edge interaction. Part I: Instantaneous pressure fields at a single frequency", Journal of Fluid Mechanics, Vol. 169, pp. 125-149.

Kaykayoglu, R. and Rockwell, D. 1986b "Unstable Jet-Edge Interaction. Part II: Multiple frequency pressure fields", Journal of Fluid Mechanics, Vol. 169, pp. 151-172.

Kaykayoglu, R. 1984 "Interaction of Unstable Shear Layers with Leading-Edges and Associated Pressure Fields", Ph.D. Thesis, Department of Mechanical Engineering and Mechanics, Lehigh University, Bethlehem, Pennsylvania.

Kramer, L. and Rockwell, D. 1984 "Evolution of Tip Vortices and Their Interaction with Thin Plates", in preparation for publication.

McAlister and Tung, C. 1984 "Airfoil Interaction with an Impinging Vortex", NASA Technical paper 2273 and Aliscom Technical Report 83-A-17, February.

Michalke, A. 1965 "On Spatially Growing Disturbances in an Inviscid Shear Layer", Journal of Fluid Mechanics, Vol. 23, Part 3, pp. 521-544.

Miksad, R. W. 1972 "Experiments on the Nonlinear Stages of Free Shear Layer Transition", Journal of Fluid Mechanics, Vol. 50, Part 4, pp. 695-719.

Naudascher, E. and Rockwell, D. 1980 "Practical Experiences with Flow-Induced Vibrations", Proceedings of the 1979 IAHR/IUTAM Symposium, Springer-Verlag, Berlin.

Patel, M. H. and Kancock, G. T. 1974 "Some Experimental Results of the Effect of a Streamwise Vortex on a Two-Dimensional Wake", The Aeronautical Journal, April, pp. 151-155.

Rockwell, D. 1983 "Invited Lecture: Oscillations of Impinging Shear Layers", AIAA Journal, Vol. 21, No. 5, May, pp. 645-664.

Rockwell, D. 1984 "Unsteady Loading of Leading-Edges in Unstable Flows: An Overview", AIAA Paper No. 84-2306, presented at the AIAA/NASA 9th Aeroacoustics Conference, October 15-17, Williamsburg, Virginia

Rockwell, D. and Knisely, C. 1979 "The Organized Nature of Flow Impingement Upon a Corner", Journal of Fluid Mechanics, Vol. 93, Part 3, pp. 321-352.

Schraub, F. A., Kline, S. T., Henry, S., Runstadler Jr., P. W., Littell, A. 1965 "Use of Hydrogen Bubbles for Quantitative Determination of Time-Dependent Velocity Fields in Low-Speed Water Flows", Journal of Basic Engineering, pp. 429-444.

Stuart, J. R. 1967 "On Finite Amplitude Oscillations in Laminar Mixing Layers", Journal of Fluid Mechanics, Vol. 29, pp. 417-428.

Volluz, R. T. 1961 "Handbook of Supersonic Aerodynamics", Section 20, Vol. 6 "Wind Tunnel Instrumentation and Operation", U. S. Bream of Naval Weapons, NAVORD Rep. 1488.

Ziada, S. 1983 "Self-Sustained Oscillation of a Mixing Layer-Wedge System", Ph.D. Thesis, Department of Mechanical Engineering and Mechanics, Lehigh University, Bethlehem, Pennsylvania.

Ziada, S. and Rockwell, D. 1982 "Vortex-Leading Edge Interaction", Journal of Fluid Mechanics, Vol. 118, May, pp. 79-107.

Ziada, S. and Rockwell, D. 1983 "Subharmonic Oscillations of a Mixing Layer-Wedge System Associated with Free Surface Effects", Journal of Sound and Vibrations, Vol. 87, pp. 483-491.

LIST OF FIGURES

List of Figures - cont.

List of Figures - cont.

List of Figures - cont.

List of Figures - cont.

List of Figures - cont.

APPENDIX: PRELIMINARY INVESTIGATION OF VORTEX STREET - ELLIPTICAL EDGE INTERACTION

Recent experiments have been carried out to investigate the mechanisms of vortex street-elliptical edge interaction (Gursul 1988)*. Figures A-1 through A-7 shown in the following describe the details of this class of interactions. Detailed measurements of the surface pressure, as well as of the velocity and vorticity fields, are forthcoming and will be reported by Gursul (1988).

---

* Gursul, I. 1988 Ph.D. Dissertation, Department of Mechanical Engineering and Mechanics, Lehigh University, Bethlehem, Pennsylvania, 18015

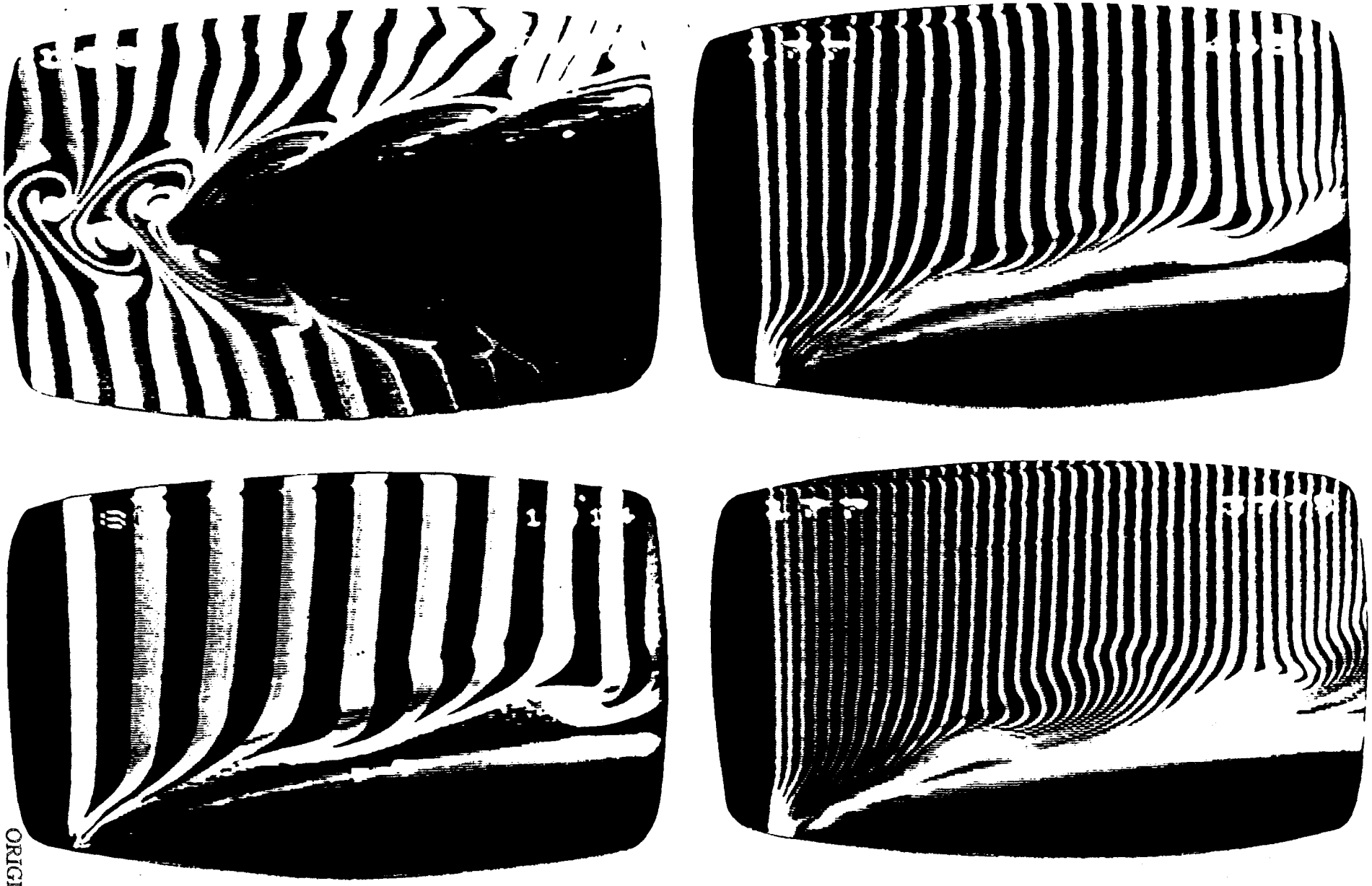

Figure A-1:
Interaction of a moderate-scale vortex street with elliptical leading-edge produces severe distortion of the incident vortices, shown in the upper left photo. However, there persists a well-defined instability along the surface, evident in the remaining photos, where the bubble wire is located at the tip, rather than well upstream of it.

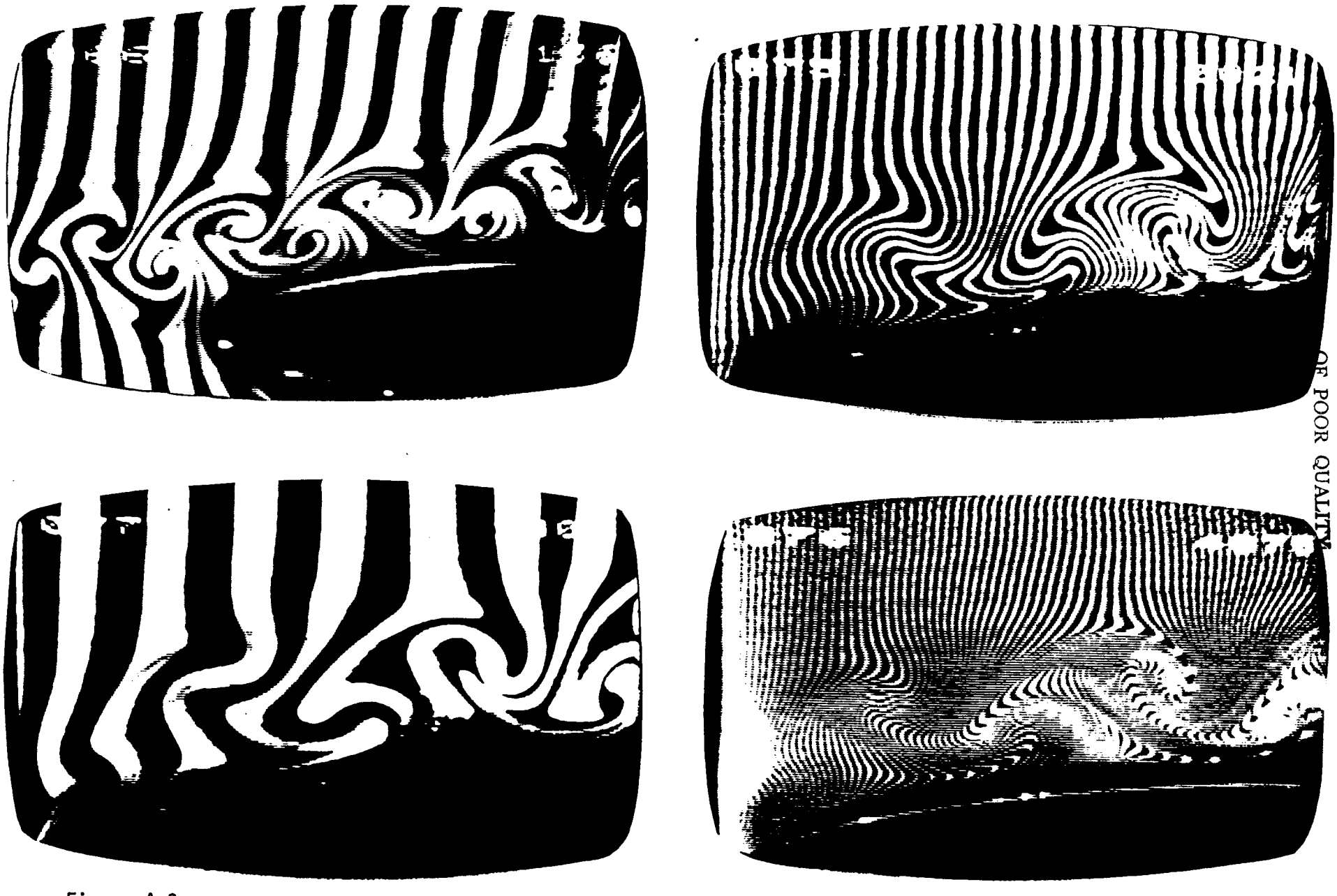

Figure A-2:
If the leading-edge is offset from the incident vortex array, it preserves its general character, with rearrangement towards a single vortex row, well downstream of the tip of the edge; these features are indicated by bubble wire locations well upstream of (upper left photo) and at (remaining photos) the tip of the edge. There is no classical secondary vortex formation due to close spacing of alternating vortices and mutual induction effects.

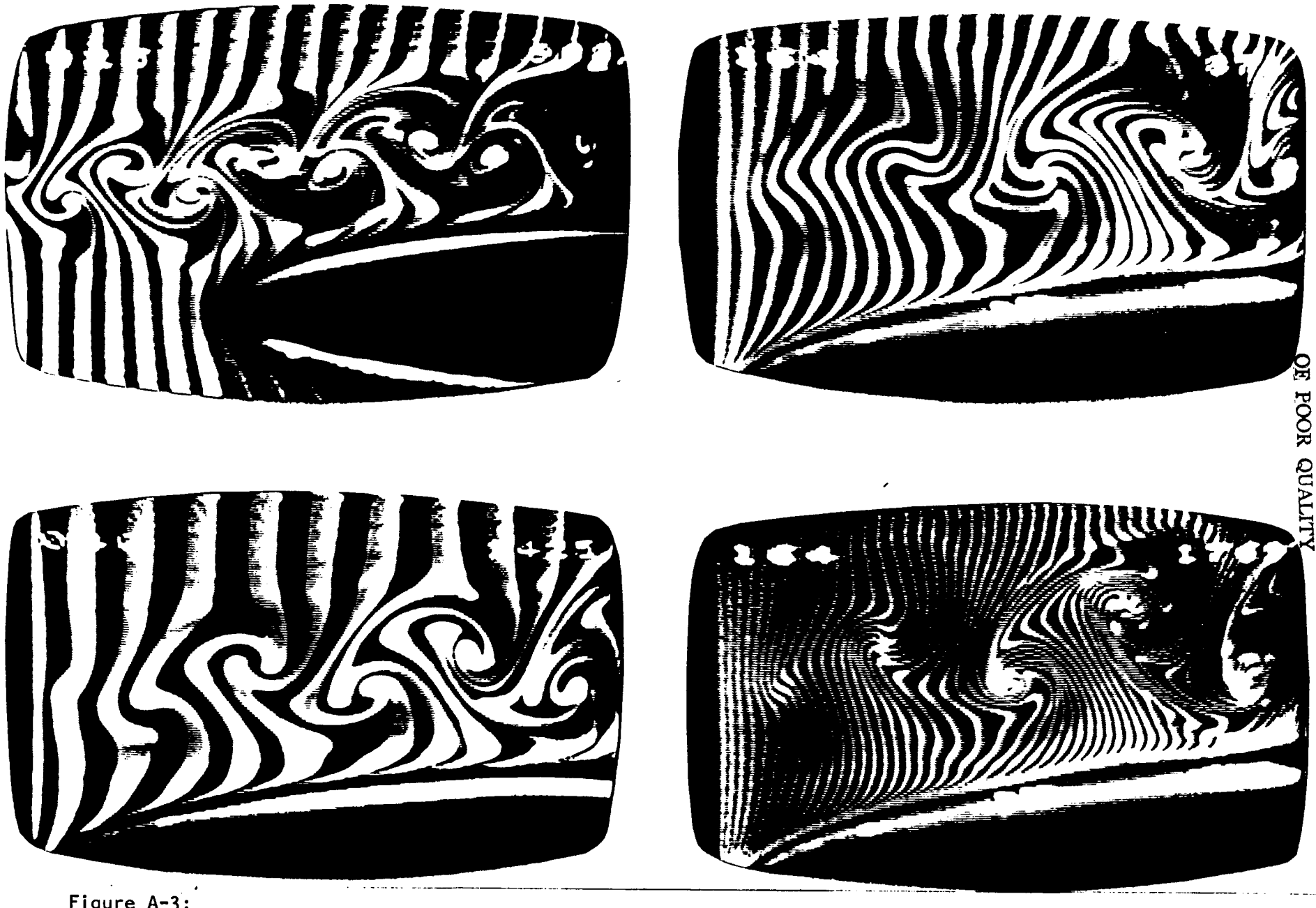

Figure A-3:
If the leading-edge is offset further from the incident vortex array, it preserves its general character well downstream of the tip of the edge; these features are indicated by bubble wire locations well upstream of (upper left photo) and at (remaining photos) the tip of the edge. There is still no classical secondary vortex formation due to close spacing of alternating vortices and mutual induction effects.

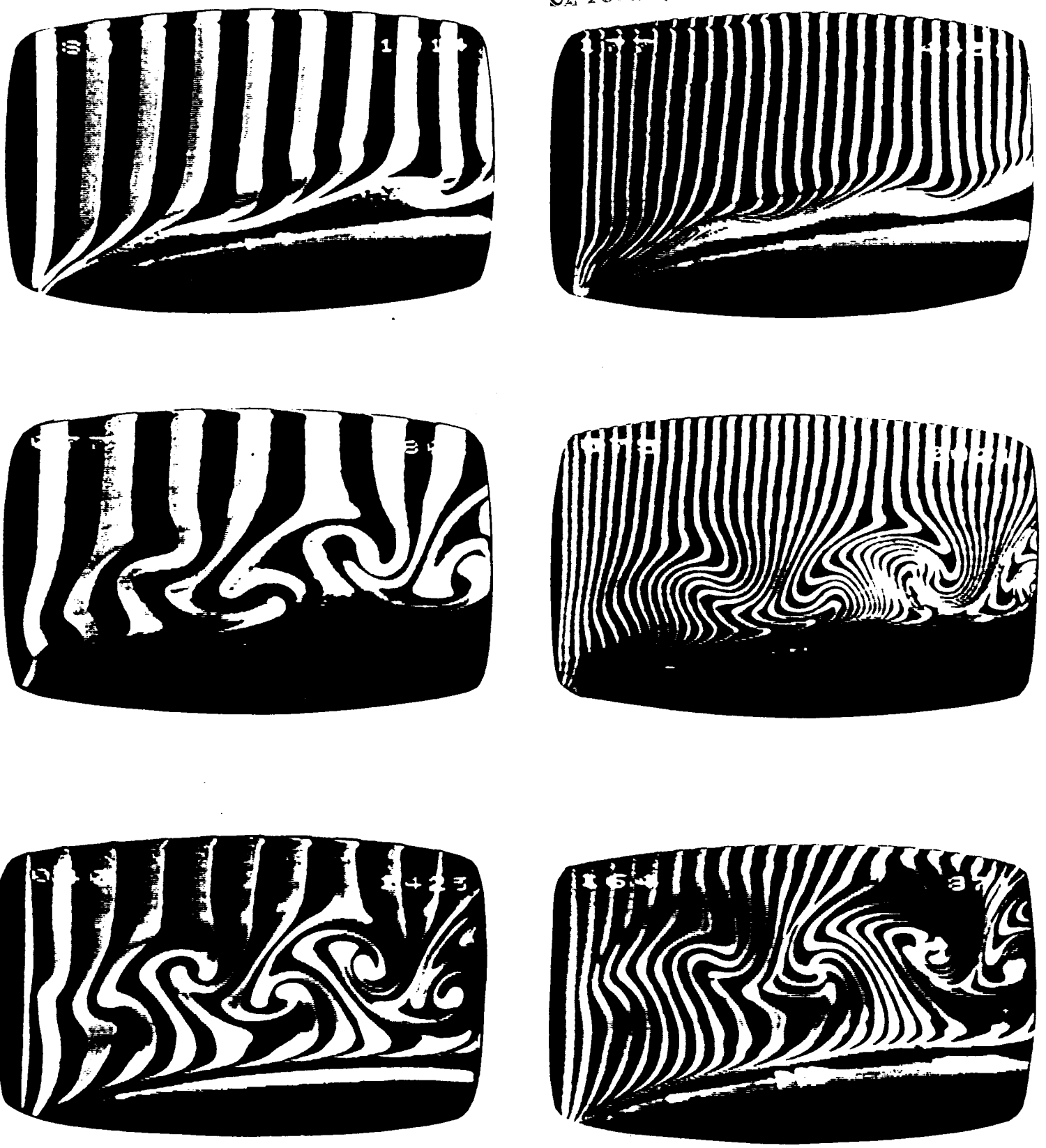

Figure A-4:
Direct comparison of effect of offset on vortex street distortion.

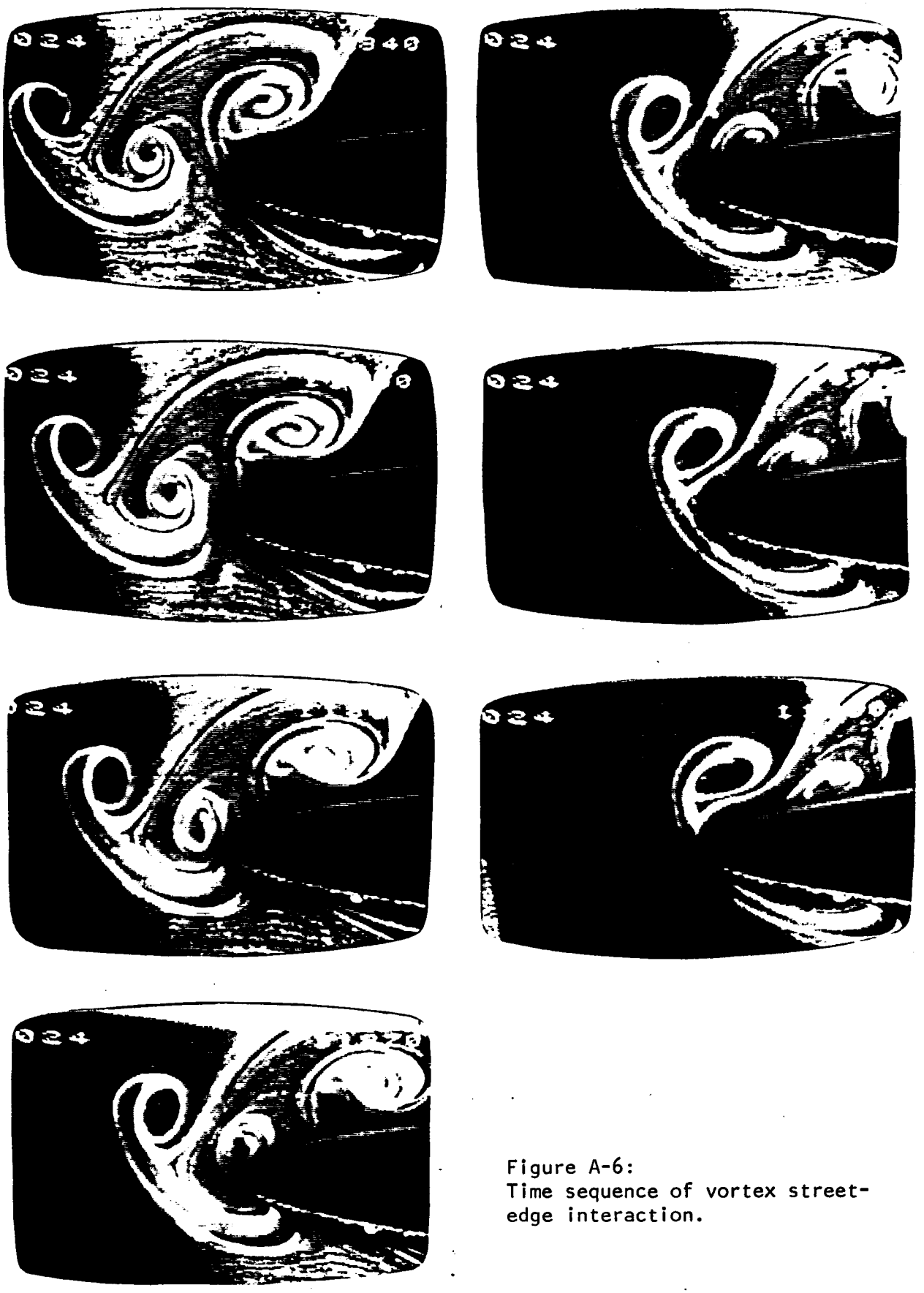

Figure A-6:
Time sequence of vortex street-edge interaction.

Figure A-7:
Time sequence of vortex street-edge interaction.